Antenna Sector-Time Division Multiple Access System for Indoor Wireless Communications

by

Aleandro Soares Macedo

A thesis submitted in conformity with the requirements
for the Degree of Doctor of Philosophy,
Graduate Department of Electrical and Computer Engineering
University of Toronto

National Library of Canada
Acquisitions and Bibliographic Services
395 Wellington Street
Ottawa ON K1A 0N4
Canada

Bibliothèque nationale du Canada
Acquisitions et services bibliographiques
395, rue Wellington
Ottawa ON K1A 0N4
Canada

Your file Votre référence

Our file Notre référence

0-612-35234-X

Canada

Antenna Sector-Time Division Multiple Access System for Indoor Wireless Communications

Aleandro Soares Macedo

Degree of Doctor of Philosophy

Department of Electrical and Computer Engineering

University of Toronto

1998

Abstract

This thesis proposes a new *multiple access* system for *indoor wireless communications* based on *sectored antennas.* Unlike previous sectored antenna indoor systems, this system incorporates the capability of reusing spectrum in different antenna sectors of the base station. It is shown that portable terminals located in different sectors of the indoor microcell may transmit/receive simultaneous data packets on the same frequency if their mutual interference is below a threshold level that guarantees an acceptable packet error rate. An experiment was devised to measure the mutual interference among portables located in some typical indoor environments. An algorithm is proposed for scheduling simultaneous packet transmissions, and its maximum throughput is investigated in the measured indoor locations. Experimental investigation was performed using ten sectors; a statistical model is used to investigate different sectorization levels. A new multi-carrier modulation scheme that requires less processing power is proposed, and the system throughput is investigated when operating with this new scheme and with the conventional multi-carrier scheme. The proposed system can significantly increase capacity when compared with systems that can transmit a single data packet per time slot. For example, while previous systems can transmit only one packet at a time, the proposed system can transmit on average more than four packets per time slot when operating with multi-carrier modulation and ten antenna sectors in an open indoor location. This same system configuration can transmit on average close to three packets per time slot in a closed indoor location with internal walls of concrete blocks.

Acknowledgements

I would like to thank Professor Elvino Sousa for his guidance and support. I also gratefully acknowledge the financial support of the Brazilian Council for Scientific and Technological Research (CNPq).

I would like to thank all my friends in the Communications Group for providing a rich environment. I appreciate the opportunity I had to learn about many cultures during these four years.

I would like to thank all my family members in Brazil, especially my parents. "Mesmo distantes, vocês sempre estiveram comigo por intermédio do Senhor Jesus Cristo."

Special thanks are extended to my wife for sharing this dream with me.

Contents

List of Figures

List of Tables

Chapter 1

Introduction

The use of wireless technology for indoor data communications in environments like office buildings, warehouses, factories, hospitals, convention centers, airport lounges, or apartment buildings is an attractive proposition. It would free portable terminals from cables, and therefore from being fixed to particular locations within these indoor environments. Besides creating mobility, it would also drastically reduce wiring in a new building, and would provide flexibility for reallocation of terminals in existing buildings without the burden and cost of rewiring. The challenge is to provide capacity for delivery of large volume, high-speed, multimedia information in an often overcrowded spectrum. The most promising way to improve system capacity is through the use of intelligent antenna systems. In the words of Andrew J. Viterbi [23]:

> *"The design of antenna systems, whether by sectoring, with arrays, or with distributed elements, provides perhaps the greatest opportunity for increasing capacity for any future advances in cellular and personal communication networks. Tailoring the antenna technique to the physical environment and population distribution, injecting and extracting signal power to and from where it is needed, is an important means of increasing capacity through spatial interference management."*

Sectored antennas are not only for future applications though; they have been used for some time in mobile cellular systems as a means of reducing interference and consequently of increasing system capacity. More recently, sectored antennas have also been applied to Wireless Local Area Networks (WLAN) [5] [6].

In [5] the use of directional antennas is considered to be an excellent technique for dealing with multipath propagation problems. In [6] sectored antennas are proposed in order to combat the severe co-channel interference arising from a small frequency reuse factor. Although [5] and [6] propose different rules for the use of sectored antennas, the final goal in both cases is to achieve an increase in system capacity.

In this thesis we propose a new multiple access scheme for WLAN which also relies on the use of sectored antennas in order to increase system capacity. However, the scheme proposed is different from the schemes proposed in [5] and [6]. The main distinction lies in its ability to exploit compatibilities among portable terminals. The concept of compatibility will be fully treated in Chapter 2, but for now we may say that portables are compatible if they are located in different sectors of the indoor microcell, and if their mutual interference is below a given threshold level. In this case, the base station can transmit or receive one data packet for each of a set of compatible portables during a single time slot. To do so, the base station will need to have the ability to use more than one of its antenna sectors at a time.

In the following section we present a summary of the multiple access scheme proposed in [5] for the Motorola ALTAIR™ WLAN. This was the first WLAN to employ intelligent antenna sectorization on a large scale. In Section 1.2 we present an overview of another proposed sectored antenna WLAN: the CITR system [6]. We will see that these two sectored antenna systems can employ only one of their antenna sectors at a time. Therefore they can not take advantage of the compatibilities we mentioned above. In Section 1.3 we introduce the multiple access scheme for sectored antenna systems that is investigated in this thesis, namely, Antenna Sector-Time Division Multiple Access.

™ ALTAIR is a trademark of Motorola.

1.1 The Motorola ALTAIR WLAN

ALTAIR Network Architecture and Protocols

Motorola has developed the ALTAIR Wireless Local Area Network (WLAN) which operates in the 18 GHz radio frequency, occupies a bandwidth of 10 MHz and transmits at a bit rate of 15 Mbps. The topology of this system is described in Figure 1.1.

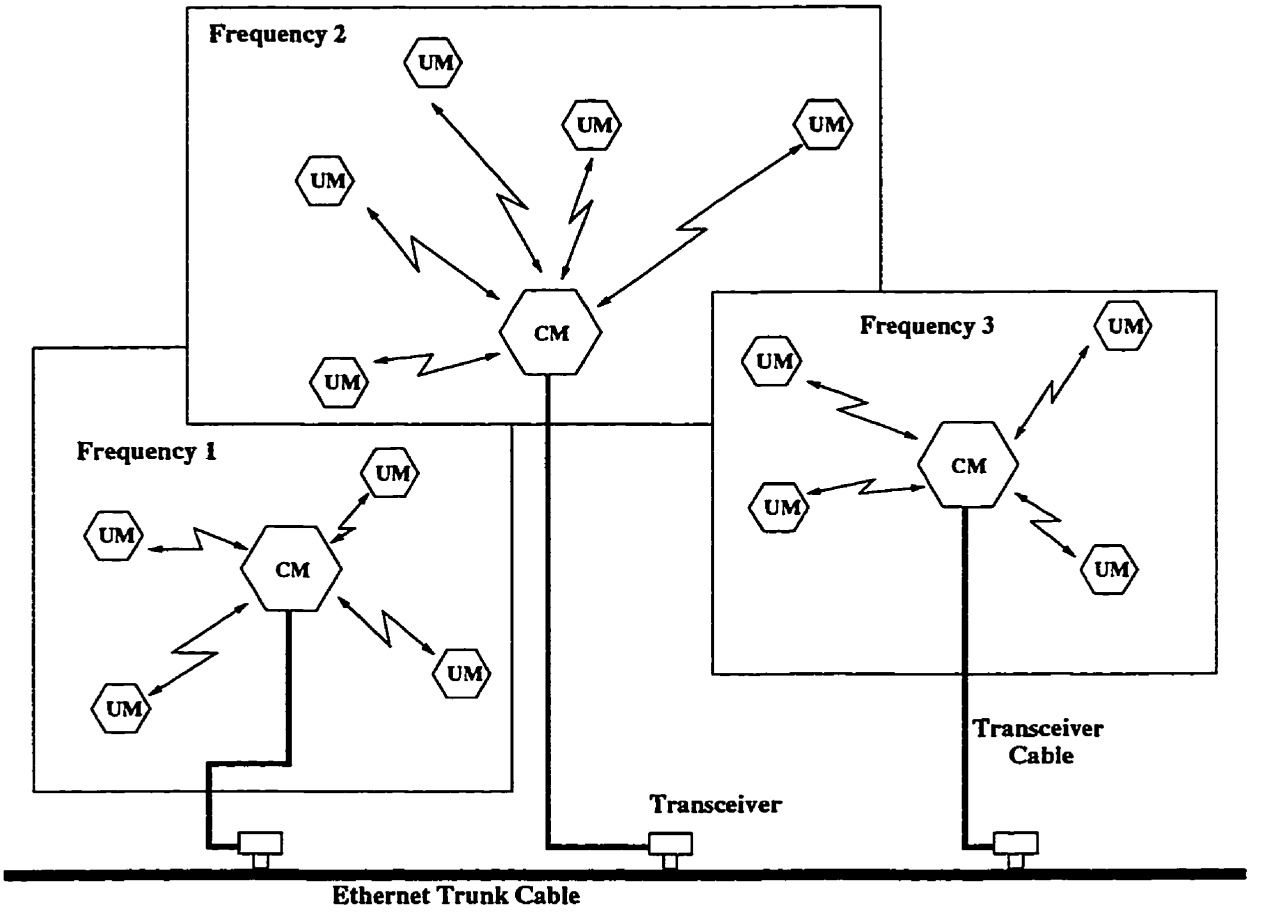

Figure 1.1: The ALTAIR Topology [5]

Two types of radio communication devices are shown in Figure 1.1: Control Modules (CMs) and User Modules (UMs). The UM works as the interface between each user's individual computer and the WLAN. The CM is the analog of a base station in cellular systems. Its main function is to relay packets from UM to UM within its coverage area,

or from UM to the wired network. The CM also performs the common functions of a base station, such as frame synchronization and coordination of packet transmissions to avoid collisions.

The CM is normally placed on the ceiling, near the center of its coverage area, which is called a microcell. Each microcell operates in a 10 MHz channel centered at a frequency close to 18 GHz. To avoid interference, neighboring microcells are not allowed to operate in the same channel. The maximum area of a microcell depends on the number and types of obstructions between radios and is typically between 450 and 5,000 m^2. The control in the microcell is centralized; UMs do not communicate directly with one another but they must communicate with a CM which acts as a relay point between UMs or between a UM and the wired backbone.

The CM and UM are similar in appearance. They are basically composed of a system of six sectored antennas controlled by a switch matrix which selects the antenna that provides the best signal for CM-UM communication. Figure 1.2 illustrates this antenna system.

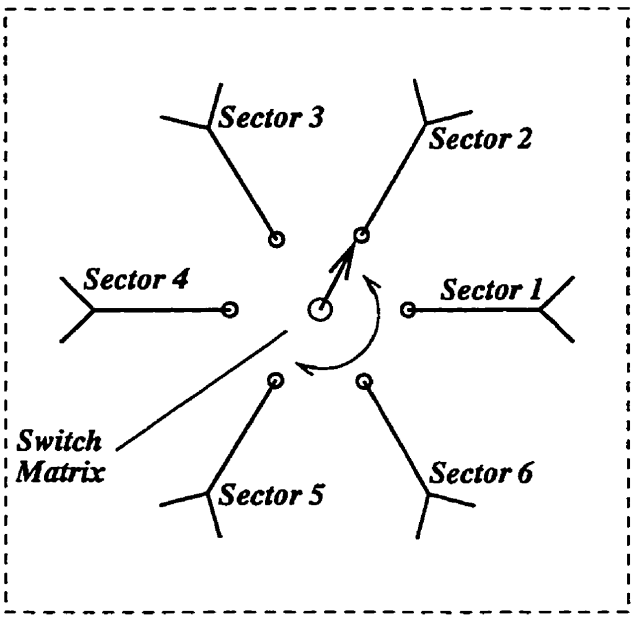

Figure 1.2: The CM/UM six-sectored antenna system. At the center, a switch matrix selects the antenna that provides the best signal

With this sectored antenna system, communication between CM and UM can occur in

one of 36 possible antenna combinations, as illustrated in Figure 1.3.

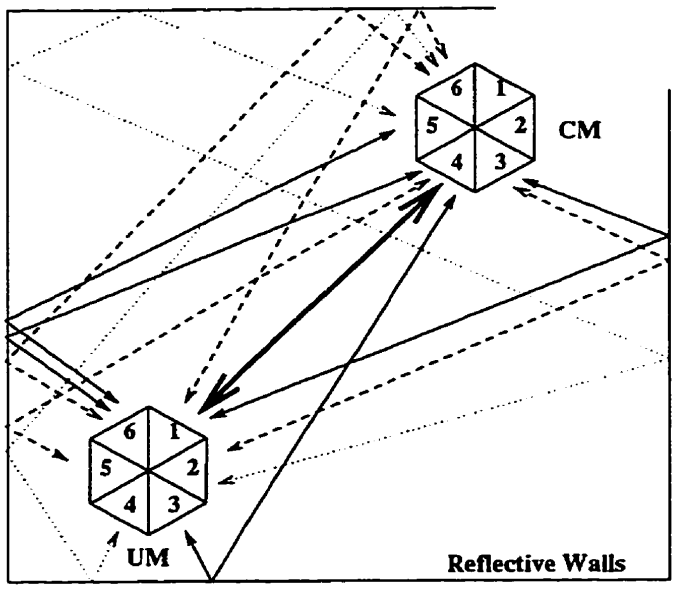

Antenna Selection Table (for illustration only)

CM \ UM	1	2	3	4	5	6
1						
2						
3	Better	Good				
4	Best		Better		Good	Better
5		Bad				Better
6	Good			Bad		Good

Bad = Below Threshold
No Value = No Signal Path

Figure 1.3: Antenna selection table showing antenna pair combinations that provide bad, good, better and best signals [5]

The multiple access scheme used in the ALTAIR WLAN is illustrated in Figure 1.4, which shows a Time Division Duplex (TDD) frame with its multiple time slots. Each time slot is capable of carrying a control or a data message. The frame repeats periodically and has a well-defined structure with areas or segments for the transmission of control information and user data from CM to UM and UM to CM. The time slots in each segment vary in size, depending on their function and the number of data packets being transported.

Frame synchronization in the microcell is defined by the CM through the transmission of

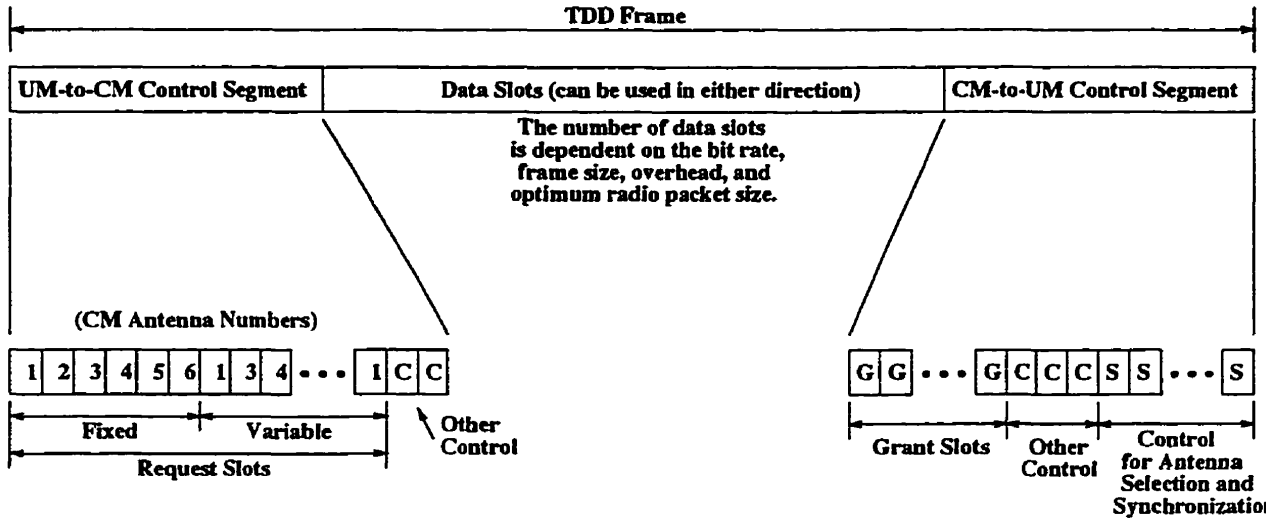

Figure 1.4: Altair TDD frame structure [5]

control packets from which the UMs obtain frame timing information. Each control packet contains a time stamp which indicates the frame number and location in the frame when the control packet was transmitted by the CM. A UM receives this time stamp and uses it to align a local clock with the CM's clock.

In order to join a microcell, a UM first listens for control packets. It periodically listens to each of its six antennas for control packets from each of the six CM antennas. The signal quality and strength are recorded for each received control packet. This information is then used to construct the antenna selection table as illustrated in Figure 1.3. The up-link path (UM-to-CM) is assumed to be the reciprocal of the down-link path since both links use the same frequency.

The values in the antenna selection table are periodically updated by averaging the signal quality and strength of the most recent sample with the corresponding value in the table. The selection table is initially built over a period of time before a UM joins a microcell in order to get an adequate sample of the radio channel characteristics. Since the channel varies with time due to changes in the environment, the best antenna pair for CM-UM communication is continually evaluated.

Once a UM has acquired TDD frame synchronization and has learned about the best

antenna pair for communication with the CM, it can attempt to join the microcell. A UM determines when to transmit a request for joining the microcell based on the CM antenna chosen from its antenna selection table and the predefined TDD frame structure which allows the UM to know in which time slot the CM will be receiving on that antenna (see Figure 1.4). These predefined time slots are *request slots* which are used by the UMs to transmit control information to the CM. A UM attempts to gain access to the microcell by transmitting a registration request in the appropriate request slot. After a validation check, the UM is notified that it has permission to request transfer of data through the system. In addition, the registration request tells the CM which antenna to use when attempting communication with this UM.

The CM and UM receive data in the form of *fragments* of Ethernet packets. Before transmission, the Ethernet packets are broken into smaller pieces, or fragments. These fragments are then transmitted during data time slots (see Figure 1.4), and after reception they are reassembled into the original Ethernet packet. Each fragment consists of a reassembly header, a piece of the Ethernet packet, and a Cyclic Redundancy Check (CRC). Figure 1.5 illustrates this fragmentation process. The reassembly header contains information pertaining to the source, destination, fragment number, number of fragments, and other control information. The fragment number and number of fragments are used to assure that all pieces have been successfully received. By means of a selective retransmission protocol whereby only missing fragments are retransmitted, the fragmentation/reassembly protocol guarantees that all fragments arrive and are reassembled in the proper order. This way, the protocol helps to overcome any potential problems due to changes in the propagation environment.

In the TDD frame, a *request/grant* protocol is used to assign time slots to UM transmissions. A UM may submit a request for time slots to the CM during an appropriate request slot. If two or more UMs make a request during the same request slot, their request will collide and will not be received by the CM. The UM will be unaware of the collision since receiving and transmitting are mutually exclusive operations. Thus, each CM antenna owns

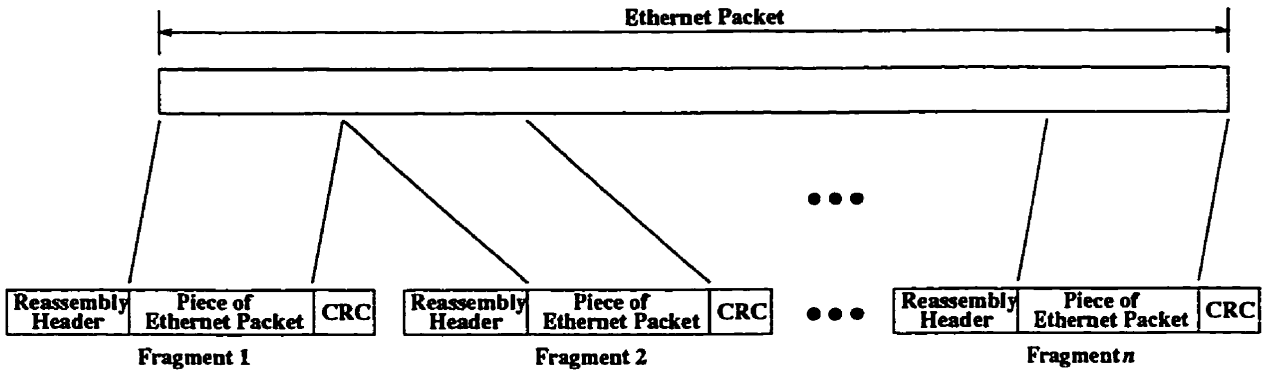

Figure 1.5: The Ethernet packet fragmentation process [5]

a set of request slots which collectively perform in a manner equivalent to a slotted Aloha system [17].

A *grant slot* is a dedicated time slot used by the CM to grant transmission time to a UM immediately prior to the frame containing the data slot(s) to be used by the UM.

The ALTAIR Modulation Scheme

The modulation scheme employed in the ALTAIR system is 4-ary Continuous-Phase Frequency-Shift Keying (CPFSK) with a symbol rate of 7.5 Msymbol/s (15 Mb/s) [8]. The transmitted signal must be limited to a strict spectral mask of 10 MHz; therefore, a non-rectangular baseband pulse shape is used. This pulse shape is realized digitally using an Application Specific Integrated Circuit (ASIC).

The ASIC symbol shaper registers are designed to store up to 16 samples to compose each symbol. These samples, each 12 bit wide, are loaded as part of the system power up sequence. Therefore, symbol shape can be changed by software.

The digital signal obtained from the ASIC symbol shaper is converted into an analogic signal and has its high-frequency components filtered out (see Figure 1.6). This signal is then used to control the Frequency Modulator which converts the baseband signal into a bandpass signal at 19 GHz. A Voltage Controlled Oscillator (VCO) is used to carry out the voltage-to-frequency conversion.

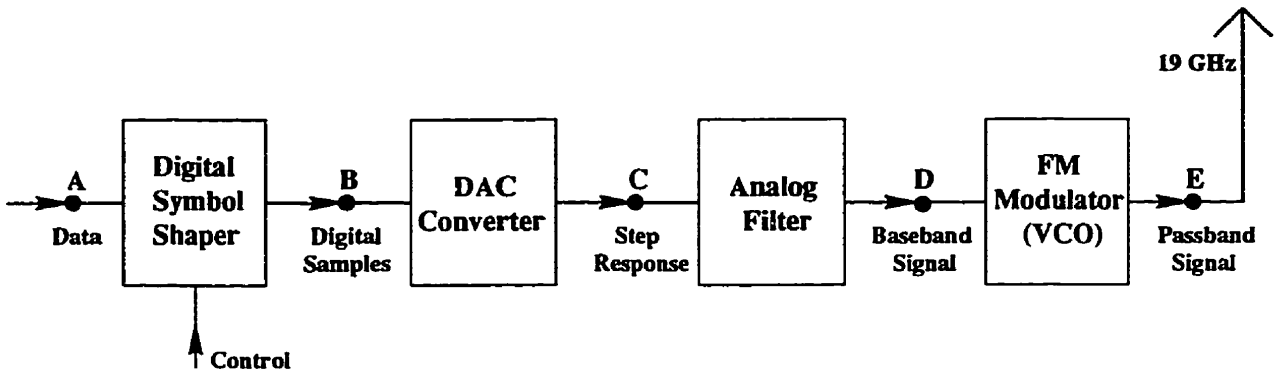

Figure 1.6: ALTAIR transmitter block diagram [8]

1.2 The CITR Broadband Indoor Wireless System

The Canadian Institute for Telecommunications Research (CITR) funded a research project aimed to develop a broadband WLAN. This section presents an overview of the proposed system.

The proposed multiple access scheme related to this project is published in [6]. It considers the use of sectored antennas in both base station and mobile terminals as done in the ALTAIR system. However, unlike the ALTAIR scheme, the CITR multiple access scheme was designed to allow high bit rate access: as high as 160 Mb/s. This system uses the Asynchronous Transfer Mode (ATM) [11] protocol, and since the rates of ATM cell generation are not necessarily commensurate, purely contention-based approaches, such as the slot-reservation scheme of the ALTAIR system, have been ruled out: the multiple access scheme proposed in this project is based on polling.

In the CITR system, up-link traffic (mobile to base) and down-link traffic (base to mobile) are carried in ATM cells which are encapsulated along with overhead information into *envelopes* for radio transmission. Like in the ALTAIR system, a TDD mode is proposed. However, unlike in the ALTAIR system, fixed length frames are used. Transmissions of envelopes in the microcell are arranged by the microcell's base station into these fixed duration frames. Each frame may carry both up-link and down-link envelopes. The overall frame structure is shown in Figure 1.7.

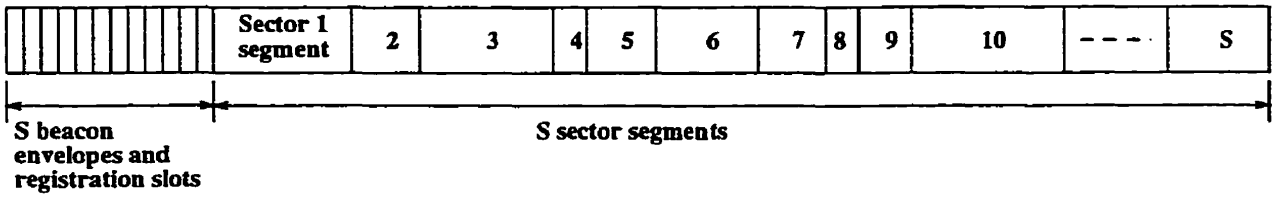

Figure 1.7: The CITR microcellular frame format [6]

The first portion of every frame is reserved for *beacon envelopes* and *registration slots* from the base station antenna sectors. At the beginning of every frame, the base station transmits, using a fixed power level, one beacon envelope on each of its S antenna sectors. Registered portables and portables that are seeking to register listen, on all of their own antenna sectors, to these beacon envelopes to determine and compare the relative power level received from each base station antenna sector. They can then determine the best base antenna-portable antenna combination to communicate with the base station.

A number of *registration slots* follow each beacon envelope. These are up-link time slots that can be used by portables seeking registration to transmit request envelopes in a slotted ALOHA protocol.

The remainder of the frame is partitioned into *sector segments*, one for each base station antenna sector. During each sector segment, the base transmits and receives only on that antenna sector. Although the sum of sector segment durations is fixed, the duration of each sector segment is different in general, and may vary from frame to frame in response to traffic demands. Figure 1.8 shows the structure of a sector segment. If the base has any envelopes destined for all portables in the sector, it starts with a control envelope indicating the number of such broadcast envelopes, followed by the envelopes themselves.

Following the broadcast envelopes, the base station polls the first portable in the sector by transmitting a polling envelope which contains a synchronization word, the identity of the portable being polled, the maximum number of up-link envelopes the base station will accept, and the number of down-link envelopes to be sent by the base to the portable. Also included is a positive or negative acknowledgement of the envelope from the terminal transmitted in the previous frame.

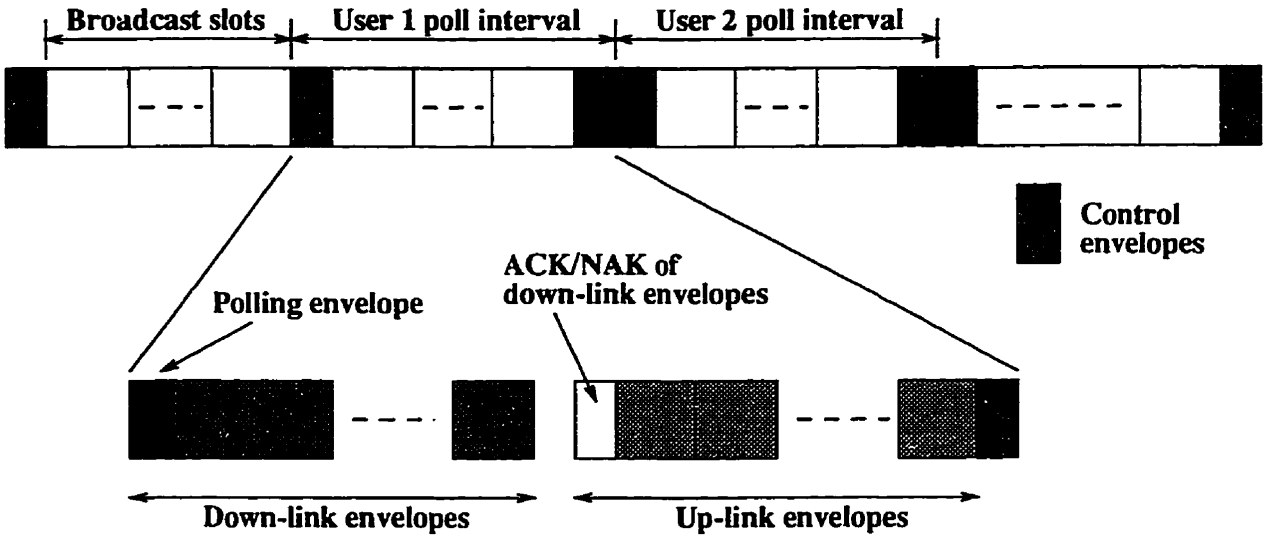

Figure 1.8: Sector segment structure [6]

After the poll, the base transmits the specified number of down-link envelopes. The portable then responds with a control envelope, and, if it has something to send, a sequence of up-link traffic envelopes up to the maximum allowed. Included as overhead information within the control envelope will be acknowledgement or a retransmission request of the down-link envelopes. There may also be requests for a higher or lower polling rate, for an increase or a decrease of transmitter power, or for switching to a different base antenna sector. Polling continues in this way for each portable.

The CITR Project Modulation Scheme

Due to the high bit rates, an anti-multipath modulation scheme was proposed for this project [28]. This modulation scheme operates with a set of N (usually a small number, such as five) orthogonal words. The transmitter encodes (spreads) each information bit with one of these words. The orthogonal words are used cyclicly, so two bits that are encoded by the same word are separated in time by $(N-1)T$, where $1/T$ is the bit rate. Therefore, since consecutive words are orthogonal, a previous word carried by a delayed path can not interferer with the current word, which makes this scheme very resistant to inter symbol interference which is caused by multipath propagation. However, this scheme

is not bandwidth efficient since it requires expanding the bandwidth by a factor of five or more. In Chapter 5 we investigate the use of multi-carrier modulation, a scheme that is both resistant to inter symbol interference and bandwidth efficient.

1.3 Antenna Sector-Time Division Multiple Access

Let us start explaining the concept of Antenna Sector-Time Division Multiple Access by redrawing Figure 1.4, which shows the TDD frame of the Motorola Altair WLAN, as Figure 1.9, where time is shown on the horizontal axis, while the vertical direction shows which of the antenna sectors is being employed during a given time slot. In this system, only the time dimension is used to achieve multiple access so that only one antenna sector is employed during any time slot.

In this thesis we propose and investigate a new multiple access scheme called Antenna Sector-Time Division Multiple Access. As its name implies, this scheme provides multiple access in the time dimension, and also in the antenna sector dimension where more than one antenna may be employed during a given time slot. Figure 1.10 illustrates how the Motorola Altair system could have its capacity increased by allowing transmission/reception in more than one antenna sector during a given data time slot to/from different UMs. However, for this scheme to be valid, the CM would need a means of knowing which UMs can share a time slot without causing unacceptable mutual interference, i.e, which UMs are compatible. With such knowledge, the CM will allow only compatible UMs to transmit/receive during the same time slot.

This new multiple access scheme, which is described in more detail in Chapter 3, has three fundamental differences from the schemes in [5] and [6]. First, we propose that it should operate in the 5 GHz range, based on the FCC (USA-Federal Communications Commission) proposal that a total spectrum of 300 MHz be allocated for unlicensed NII devices in the short-to-medium communications range [9]. The 5 GHz frequency band is considered the appropriate spectrum for broadband WLAN. The spectrum below this range

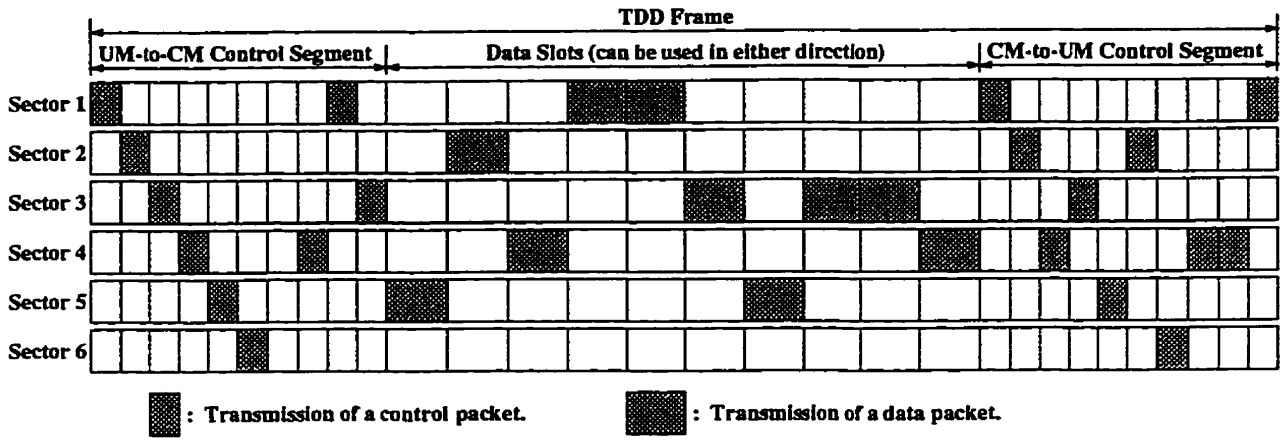

Figure 1.9: The Motorola Altair TDD frame redrawn to show antenna sectors being used

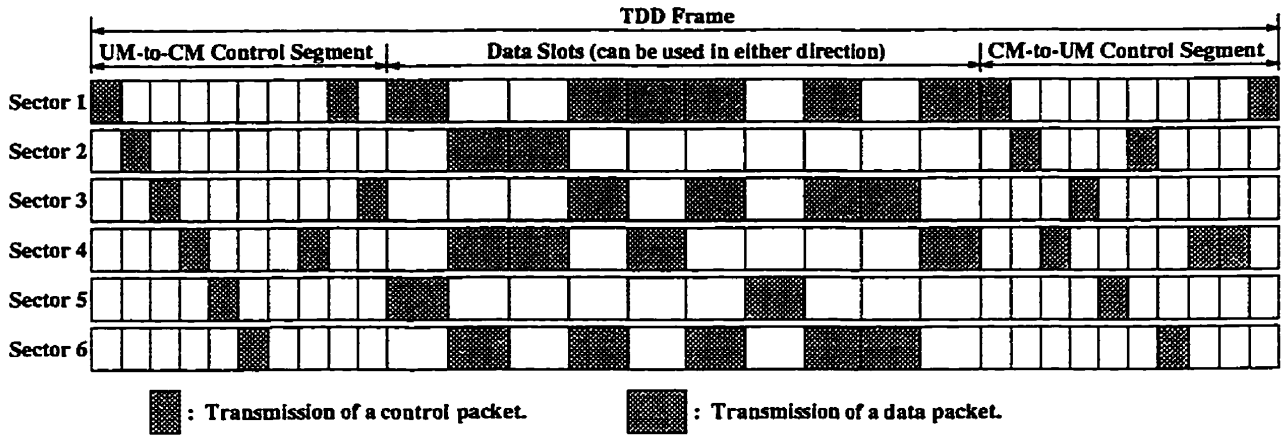

Figure 1.10: Antenna Sector-Time Division Multiple Access Frame

is too congested, and the spectrum at higher frequencies, such as millimeter waves, would increase the cost of equipment and exhibit severe propagation characteristics. Moreover, we assume that the use of sectored antennas in both the base station and portable modules causes the system to become excessively complex, and, due to the size of the sectored antenna system, not suitable for a portable terminal. Therefore the conservative approach of concentrating the complexity of the system in the base station is adopted in order to be able to use simpler antennas in the portables: we propose using sectored antennas only in the base station and simple omni-directional antennas in the portables. Finally, as already mentioned, multiple access makes use of compatibility relations among portables

in an indoor microcell in order to increase capacity. The concept of compatibility is fully explained in the next chapter.

In order to validate the multiple access proposal, we performed channel measurements in three different indoor locations. A sectorization level of 10 (10 sectors) was assumed in the measurements. The use of different sectorization levels is investigated in Chapter 4 through statistical modeling of indoor multipath propagation.

The effect of using omni-directional antennas in the portables is larger delay spread profiles in the channels. As a result, the system requires a modulation scheme that is capable of overcoming channel dispersion. At the same time, this scheme has to be bandwidth efficient, and it has to avoid the high-power consumption signal processors needed for equalization. An alternative multi-carrier modulation that fits these requirements is proposed by Macedo and Sousa [1]. In Chapter 5 we investigate the performance of the proposed multiple access technique when operating with this alternative multi-carrier scheme, and compare the performance results with the results obtained when the system operates with the conventional multi-carrier modulation.

Chapter 2

The Concept of Compatibility

2.1 Introduction

The multiple access schemes described in [5] and [6] allow transmission/reception in only one of the antenna sectors at a time, usually in the one that provides the best communication channel between the base station and a given portable. Figure 2.1-a shows sectored antennas similar to those in [5] and [6]. The RF switch matrix used to select the desired antenna from the set can be fabricated compactly and inexpensively using either a Gallium Arsenide Monolithic Microwave Integrated Circuit (GaAs MMIC) or microwave diode switching elements [7].

The multiple access scheme proposed in this thesis achieves in-cell frequency reuse by allowing simultaneous transmissions over different antenna sectors in order to take advantage of existing compatibilities among portables in an indoor microcell. Figure 2.1-b represents the same set of antennas as in Figure 2.1-a but with a switch matrix capable of simultaneously selecting two antennas and connecting each to a desired port that can be connected to a transmitter or to a receiver. The sectored antenna system of Figure 2.1-b has the potential to double the capacity of the system by allowing simultaneous transmissions/receptions to occur in two antenna sectors sharing the same frequency spectrum. However, as we start explaining now, this kind of spectrum sharing requires compatible portables.

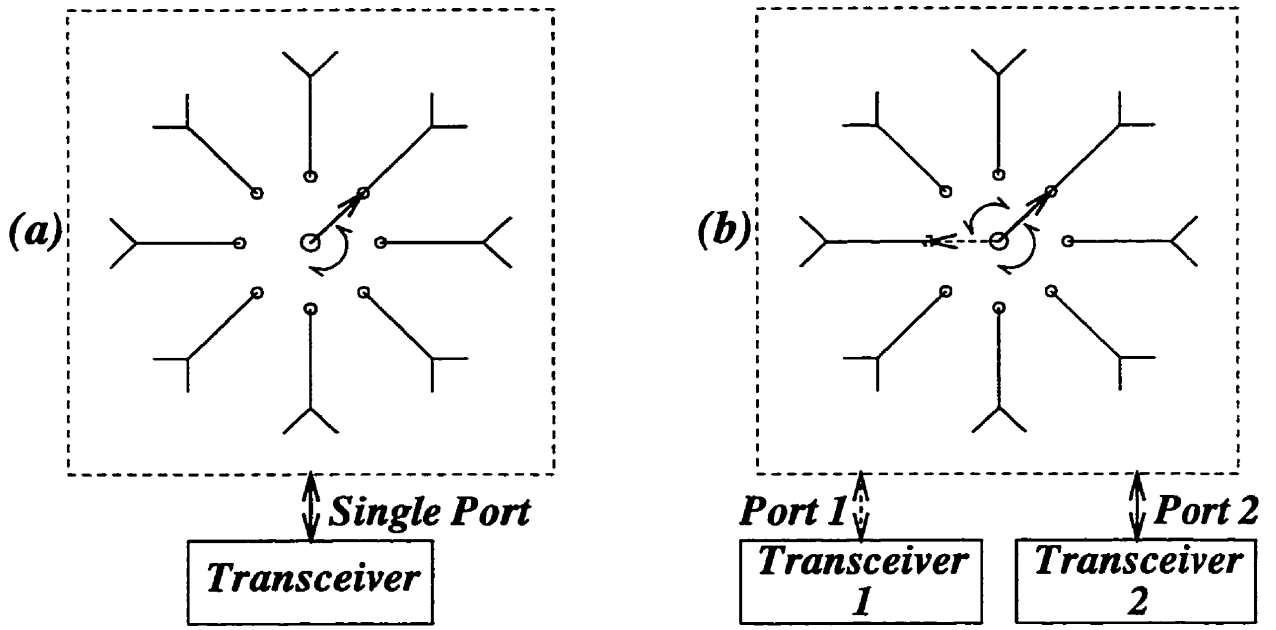

Figure 2.1: (a) Sectored antenna system similar to those in [5] and [6]; (b) The 2-port sectored antenna system

2.2 Compatibility Condition

The concept of compatibility is explained with the help of Figure 2.2, which shows a base station using a 2-port sectored antenna system to communicate simultaneously with two portables, $\mathbf{P}_1$ and $\mathbf{P}_2$. The signal strength values quoted in this figure were chosen for illustrative purposes. The reflectors represent reflecting structures, for example, walls or metallic doors. In order to verify the compatibility between portables $\mathbf{P}_1$ and $\mathbf{P}_2$, the minimum Signal-to-Interference Ratio (SIR) acceptable for communication between the base station and a portable has to be specified. This parameter is the capture threshold, which we name Π. Its value is dependent on the coding and on the modulation scheme employed. For example, spread spectrum modulation schemes can operate with a level of interference above the level of the signal, which results in a negative value of Π (in decibel). However our multiple access scheme is intended to operate with narrow band (non spread spectrum) modulation schemes which can achieve high spectrum efficiency, around 1 bps/Hz, as required in the FCC proposal for U-NII wireless networks [9]. Therefore we

will be considering values of Π in the range of 5 to 20 dB.

It is assumed that an up-link transmission and a down-link transmission can not occur simultaneously: either both transmissions are in the up-link direction (from portable to base station) or both are in the down-link direction (from base station to portable). This assumption is made because the level of interference that a down-link transmission would cause in an up-link reception would be unacceptable: in the base station, the power level of a transmitted signal is much higher than the power level of a received signal.

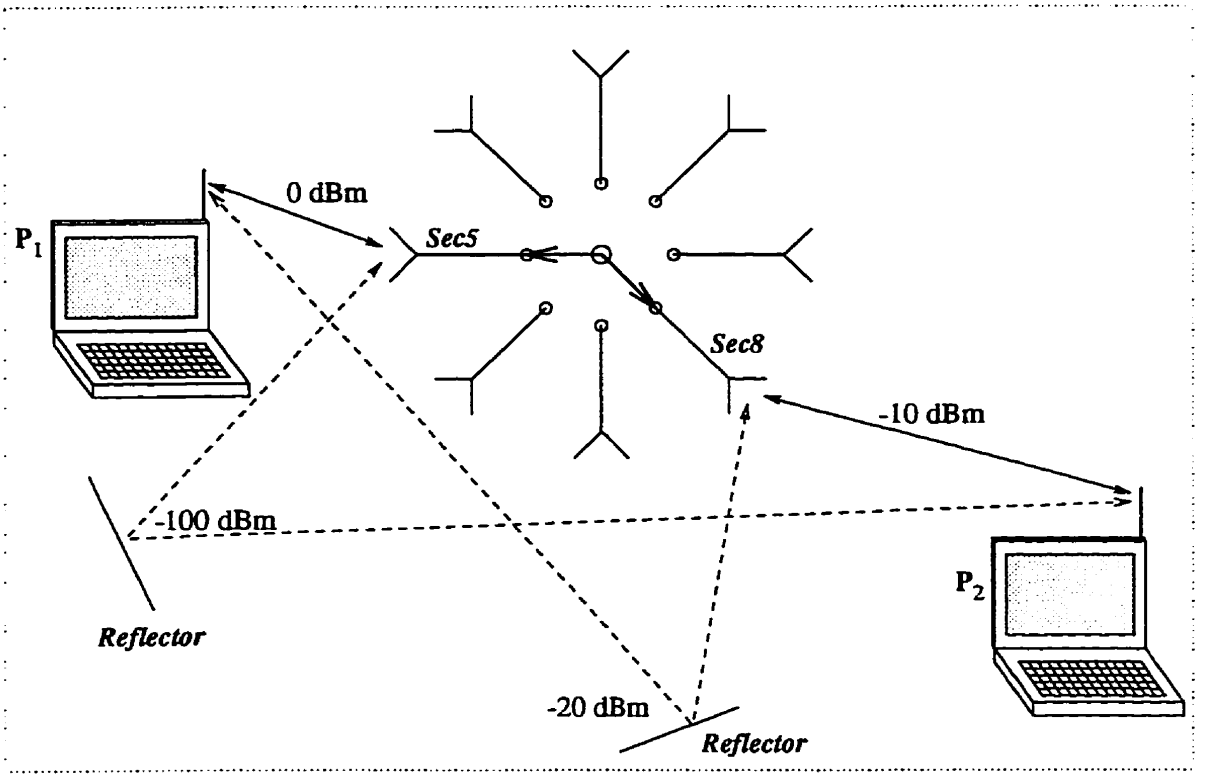

(a)

	Sec5	*Sec8*
P_1	0	-20
P_2	-100	-10

(b)

	Sec5	*Sec8*
P_1	0	-20
P_2	-100 +10 = -90	-10 + 10 = 0

(c)

Figure 2.2: (a) A base station communicating simultaneously with two portables; (b) Table of average power levels (dBm) received without power control; (c) Table of average power levels (dBm) received with power control

In the down-link case, the base station uses antenna sector 5 to transmit to portable P_1,

and antenna sector 8 to transmit to portable $\mathbf{P_2}$. Portable $\mathbf{P_1}$ receives a signal from antenna sector 5 at an average power level of 0 dBm and interference from antenna sector 8 through a reflected path at an average power level of -20 dBm. Simultaneously portable $\mathbf{P_2}$ receives a signal from antenna sector 8 at an average power level of -10 dBm and interference from antenna sector 5 through a reflected path at an average power level of -100 dBm. Therefore, the SIR for the signal received by portable $\mathbf{P_1}$ is 20 dB, and the SIR for the signal received by portable $\mathbf{P_2}$ is 90 dB. Then we say that portables $\mathbf{P_1}$ and $\mathbf{P_2}$ are compatible in the down-link case if $\Pi \leq 20$ dB.

In the up-link case, the base station receives, through antenna sector 5, the signal transmitted by $\mathbf{P_1}$ at an average power level of 0 dBm and interference of -100 dBm from the reflected signal transmitted by $\mathbf{P_2}$, yielding an SIR of 100 dB for the $\mathbf{P_1}$ transmitted signal. Simultaneously, the base station receives, through antenna sector 8, the signal transmitted by $\mathbf{P_2}$ at an average power level of -10 dBm and interference of -20 dBm from the reflected signal transmitted by $\mathbf{P_1}$, yielding an SIR of 10 dB for the $\mathbf{P_2}$ transmitted signal. Therefore we say that portables $\mathbf{P_1}$ and $\mathbf{P_2}$ are compatible in the up-link case if $\Pi \leq 10$ dB.

In this example, which does not consider power control, compatibility in the down-link case does not necessarily correspond to compatibility in the up-link case. In fact, we observed through measurement results that the average number of compatibilities among portables in an indoor microcell is, in general, larger for the down-link case than for the up-link case. This down-link/up-link average compatibility asymmetry arises because, in the up-link case, portables located closer to the base station cause stronger interference with the signals of portables located on the periphery of the indoor microcell. In a sense this problem is similar to the near-far effect that decreases the up-link capacity of CDMA systems. Therefore it is expected that power control can be used to improve the average number of compatibilities in the up-link case. This is shown to be true later in this chapter by analyzing measurement results.

Consider now the use of power control in Figure 2.2. In this case, portable $\mathbf{P_2}$ increases

its transmitted power so that the base station can receive its signal with the same power level of the signal received from portable $\mathbf{P}_1$. Then $\mathbf{P}_2$ has to add 10 dB to its transmitted signal power. By doing so, it also adds 10 dB to the interference caused in the $\mathbf{P}_1$ signal. This is shown in Figure 2.2-c. If the up-link SIR values are recalculated with the power control values of Figure 2.2-c, the SIR values obtained are 90 dB for the $\mathbf{P}_1$ signal and 20 dB for the $\mathbf{P}_2$ signal. Therefore, the minimum of the two SIR values, 20 dB, is 10 dB better than the minimum SIR value obtained without power control.

In order to express the compatibility conditions mathematically we define the following parameters:

- $G_{p,s}$ (Portable-Sector Power Gain): represents the average power received through the channel between portable $\mathbf{P}_p$ and antenna sector s. It has the same value for both up-link and down-link channels (provided that the same power level is transmitted in both cases). This is true because we assume that up-link and down-link transmissions occur in the same frequency band (but not at the same time); therefore up-link and down-link channels are reciprocal.

- $B(i)$: represents the best antenna sector for communicating with $\mathbf{P}_i$.

These parameters are illustrated in Figure 2.3 and in Figure 2.4 for portables $\mathbf{P}_1$ and $\mathbf{P}_2$, where $B(1) = 5$ and $B(2) = 8$.

Using these definitions, we can express the conditions for the existence of compatibility in the down-link case between two portables $\mathbf{P}_i$ and $\mathbf{P}_j$ as:

$$\left\{ \begin{array}{l} 10\log\left[\frac{G_{i,B(i)}}{G_{i,B(j)}}\right] \geq \Pi \\ \\ 10\log\left[\frac{G_{j,B(j)}}{G_{j,B(i)}}\right] \geq \Pi \end{array} \right\} . \tag{2.1}$$

In the up-link case the conditions for the existence of compatibility between two portables $\mathbf{P}_i$ and $\mathbf{P}_j$ are:

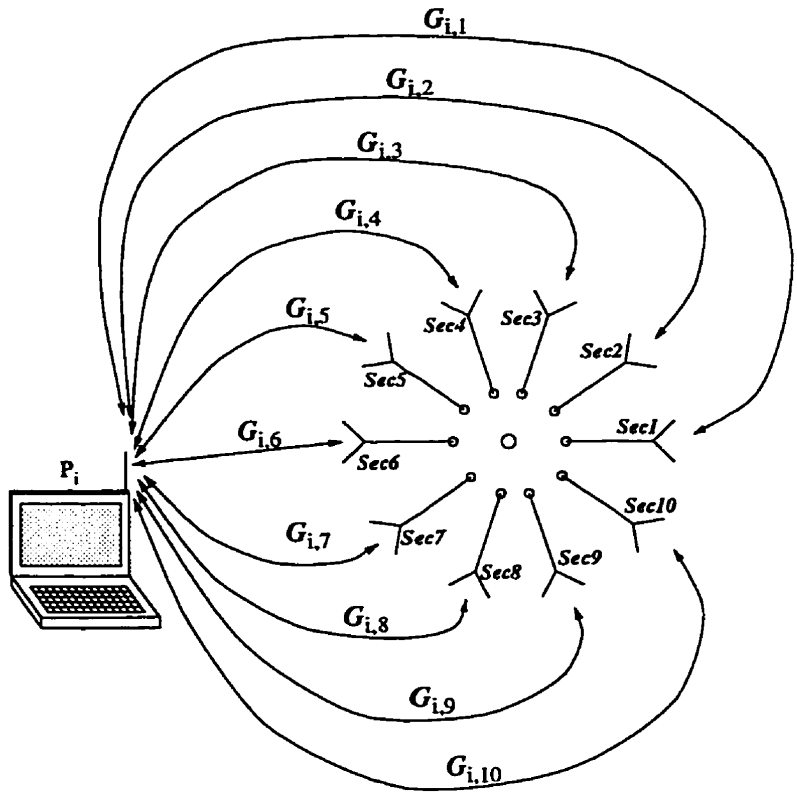

Figure 2.3: Illustration of the $G_{p,s}$ parameter

$$\left\{ \begin{array}{l} 10\log\left[\frac{G_{i,B(i)}}{G_{j,B(i)}}\right] \geq \Pi \\ \\ 10\log\left[\frac{G_{j,B(j)}}{G_{i,B(j)}}\right] \geq \Pi \end{array} \right\} . \tag{2.2}$$

2.3 Compatibility Condition for the N-Port Case

In the previous section, we considered compatibility for the 2-port case, which implies using a system of sectored antennas with two ports as shown in Figure 2.1-b. Now we consider a system of sectored antennas with N ports as shown in Figure 2.5.

An N-port antenna system would allow a maximum of N simultaneous transmissions in N different antenna sectors. As such it would have a switching matrix capable of selecting N of the antenna sectors and connecting each of them to one of N ports (each port is

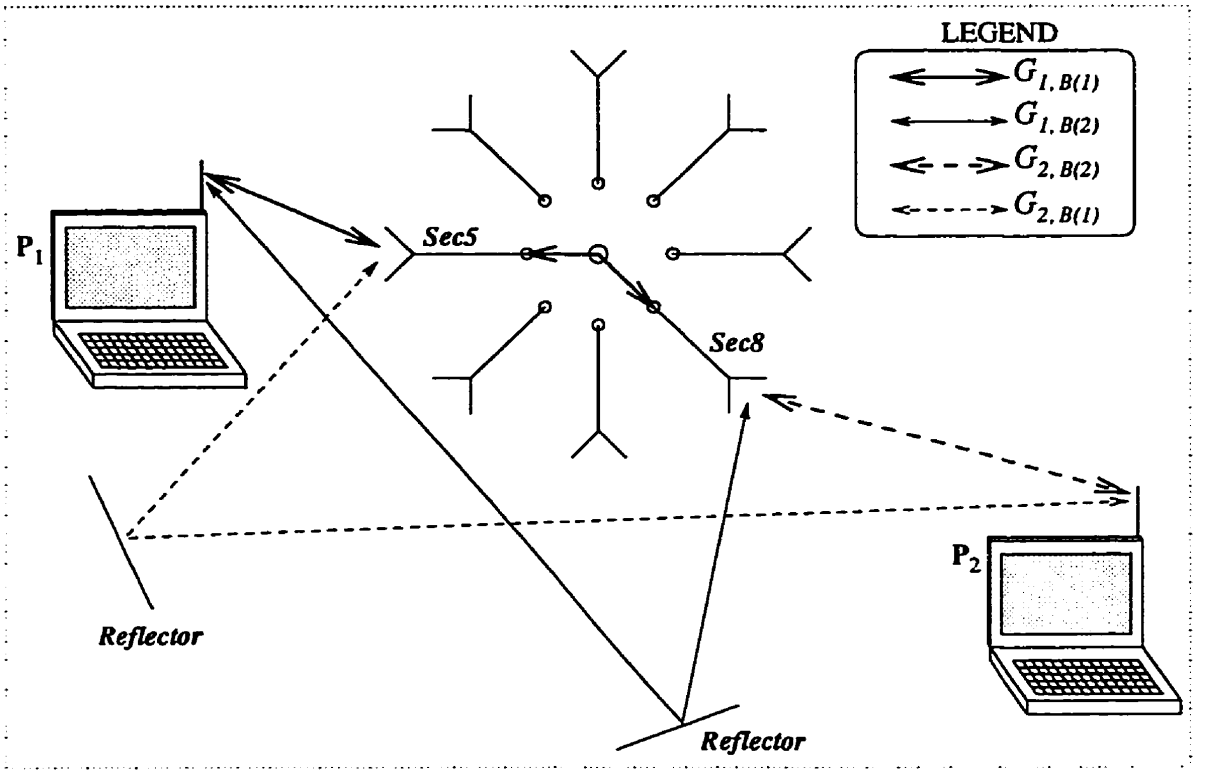

Figure 2.4: Illustration of parameters $G_{p,s}$ and $B(i)$ for portables $\mathbf{P}_1$ and $\mathbf{P}_2$

connected to a transmitter/receiver). In this case the conditions for compatibility among N portables $\mathbf{P}_1$, $\mathbf{P}_2$, ... , $\mathbf{P}_N$ in the down-link case are given in (2.3).

$$\left\{ \begin{array}{l} 10\log\left[\frac{G_{1,B(1)}}{G_{1,B(2)}+G_{1,B(3)}+,\ldots,+G_{1,B(N)}}\right] \geq \Pi \\ \\ 10\log\left[\frac{G_{2,B(2)}}{G_{2,B(1)}+G_{2,B(3)}+,\ldots,+G_{2,B(N)}}\right] \geq \Pi \\ \\ \cdot \\ \cdot \\ \cdot \\ 10\log\left[\frac{G_{N,B(N)}}{G_{N,B(1)}+G_{N,B(2)}+,\ldots,+G_{N,B(N-1)}}\right] \geq \Pi \end{array} \right\}, \tag{2.3}$$

and, in the up-link case, the compatibility conditions are given in (2.4). Note that these N portables represent a subset of all the portables in the microcell.

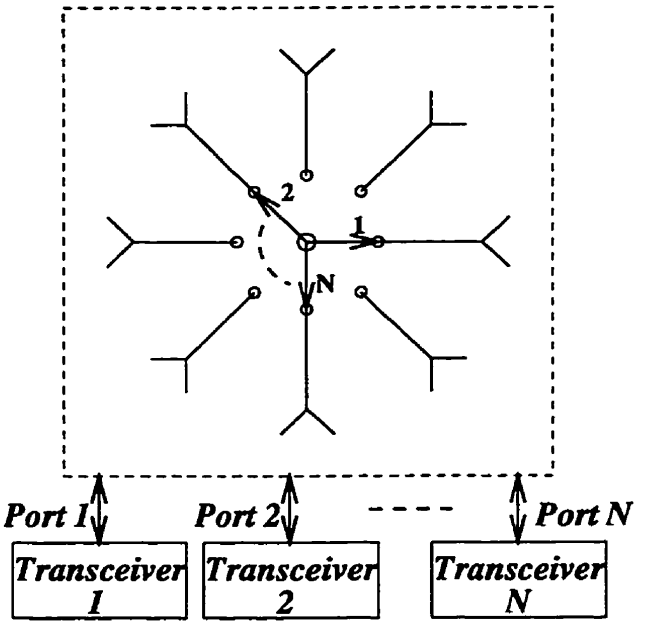

Figure 2.5: The N-port sectored antenna system

$$\left\{ \begin{array}{l} 10\log\left[\frac{G_{1,B(1)}}{G_{2,B(1)}+G_{3,B(1)}+,\ldots,+G_{N,B(1)}}\right] \geq \Pi \\ \\ 10\log\left[\frac{G_{2,B(2)}}{G_{1,B(2)}+G_{3,B(2)}+,\ldots,+G_{N,B(2)}}\right] \geq \Pi \\ \\ \quad . \\ \quad . \\ \quad . \\ 10\log\left[\frac{G_{N,B(N)}}{G_{1,B(N)}+G_{2,B(N)}+,\ldots,+G_{N-1,B(N)}}\right] \geq \Pi \end{array} \right\} \quad (2.4)$$

If the N conditions of (2.3) are satisfied, then there may be N simultaneous packet transmissions during a time slot to these N portables (down-link case). This means that, during this time slot, the down-link system capacity is multiplied by N, i.e., N packets are transmitted through N sectors instead of the single packet that could be transmitted in this time slot if a single port sectored antenna system were used in the base station. Similarly, if the N conditions of (2.4) are satisfied, then there may be N simultaneous packet

transmissions during a time slot from these N portables (up-link case), which corresponds to the up-link system capacity being multiplied by N. In general, however, an increase in the number of ports does not correspond to a proportional increase in system capacity, as can be observed from measurement and simulation results presented later in this thesis. The reason is that the number of subsets of N portables that correspond to compatible portables decrease as N increases. For example, the probability of two portables being compatible is larger than the probability of three portables being compatible. Therefore, as the number of ports N increase, it is more likely that some of them will not be used during a given time slot due to a lack of compatible portables. The capacity gain eventually saturates at a given number of ports.

2.4 Channel Measurements

We devised an experiment which allowed us to measure the portable-sector power gain ($G_{p,s}$) values for a base station and portables located in some typical indoor environments. With these values, we were able to verify the compatibility among portables using the conditions established in (2.3) or (2.4). The experimental setup is depicted in Figure 2.6. The output of the frequency sweeper was amplified to a maximum of 25 dBm and radiated with a $\lambda/4$ mono-pole antenna which provided an omni-directional radiation pattern. The frequency sweeper, the power amplifier and the transmitting antenna were mounted on a cart, allowing the transmitter to be moved to any position within the indoor location for the purpose of simulating portables.

In order to simulate the base station, a horn antenna was mounted on a tripod and placed at the center of the indoor location. This horn antenna, with approximately 36° of 3 dB beam-width in its H-plane, could be rotated around its vertical axis, which allowed the simulation of 10 sectors by pointing it in 10 different directions. The horn antenna radiation pattern is shown in Figure 2.7, and the superimposed field strength patterns of the 10 sectors are shown in Figure 2.8. The signal received by the horn antenna was then

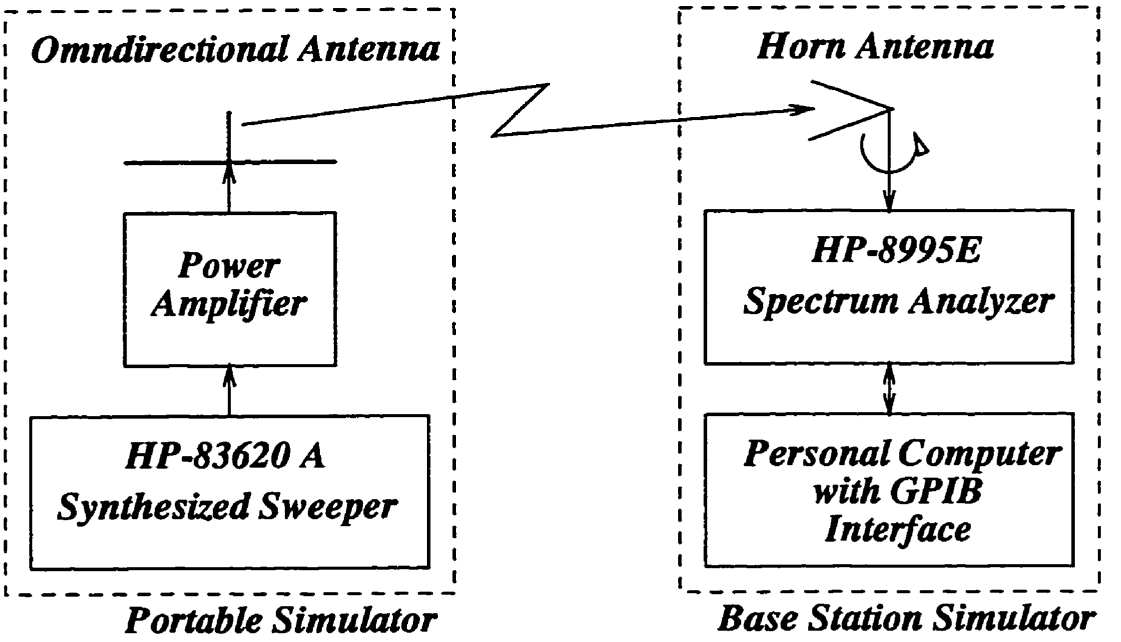

Figure 2.6: Channel measurement setup

measured by a spectrum analyzer connected to a personal computer through a General Purpose Instrumentation Bus (GPIB) interface.

The purposes and limitations of this experiment should be made clear. The aim was not to study the angle of arrival spread as in [14], nor was it to study channel characterization at the level studied in [16], where a coherent wideband measurement system is used to measure power delay profile, path loss, coherence bandwidth and delay spread of indoor channels. The single channel parameter this experiment sought to obtain is the portable-sector power gain ($G_{p,s}$) that was defined in the previous section. If this parameter is measured for many positions in the indoor location, it can be used to verify compatibility relations among these positions, i.e., among the portables that are supposed to occupy these positions. Since we measured with a horn antenna with approximately 36° of 3 dB beam-width, we could investigate experimentally only for a sectorization level of 10 (10 sectors). In Chapter 4 we study different sectorization levels using a statistical multipath propagation model that considers ray angle of arrival.

The synthesized sweeper was programmed to slowly sweep a continuous wave signal

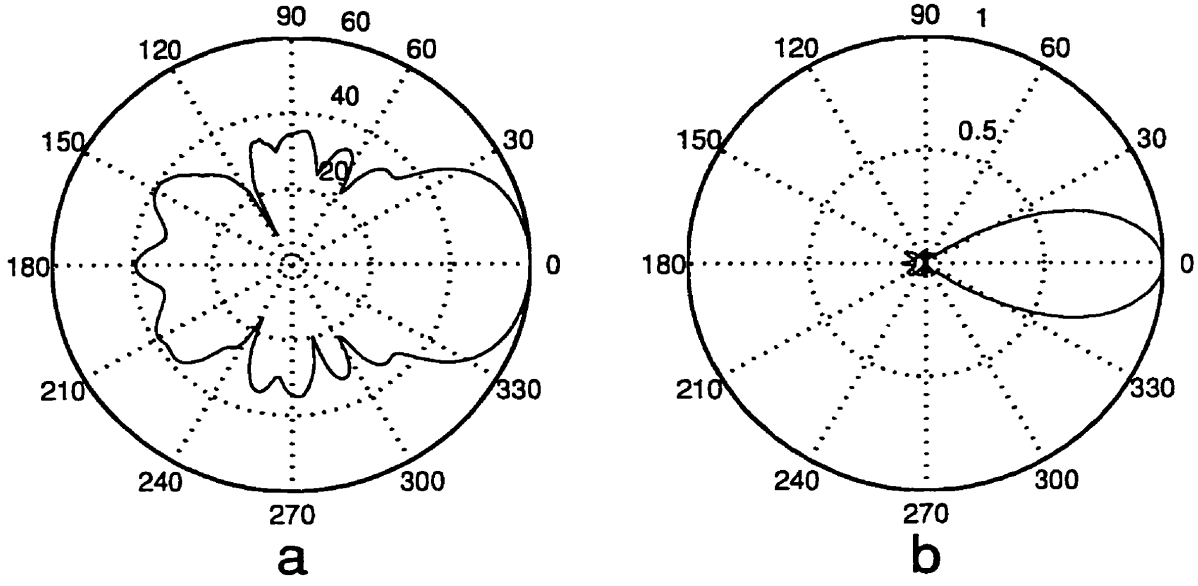

Figure 2.7: (a) Polar coordinate plots of power radiation pattern on logarithmic scale; and (b) normalized field strength pattern on linear scale of the horn antenna used in the experiment. Note: the plotted values were normalized by making the maximum value equal to 60 dB in the logarithmic plot, and by making the maximum value equal to 1.0 in the linear plot.

within a bandwidth of 20 MHz, which is the expected bandwidth for U-NII channels [9], centered at 5.8 GHz. A computer program was developed to control the spectrum analyzer which received instructions to measure, for each transmitter position and for each sector, the signal strength of approximately 40 frequency samples within the 20 MHz band. The synthesized sweeper and the spectrum analyzer were not synchronized. Therefore there was no need to lay down a cable between the sweeper and the spectrum analyzer. Since the two instruments were not synchronized, in order to be able to track the swept signal which was set to sweep the 20 MHz in 20 seconds, the spectrum analyzer used an internal function that allowed it to find the strongest signal peak within the 20 MHz band. This function could be performed approximately 40 times every 20 seconds. The instantaneous frequency of the continuous wave signal being slowly swept by the synthesized sweeper was acquired by the spectrum analyser every time this function was performed, and its strength was

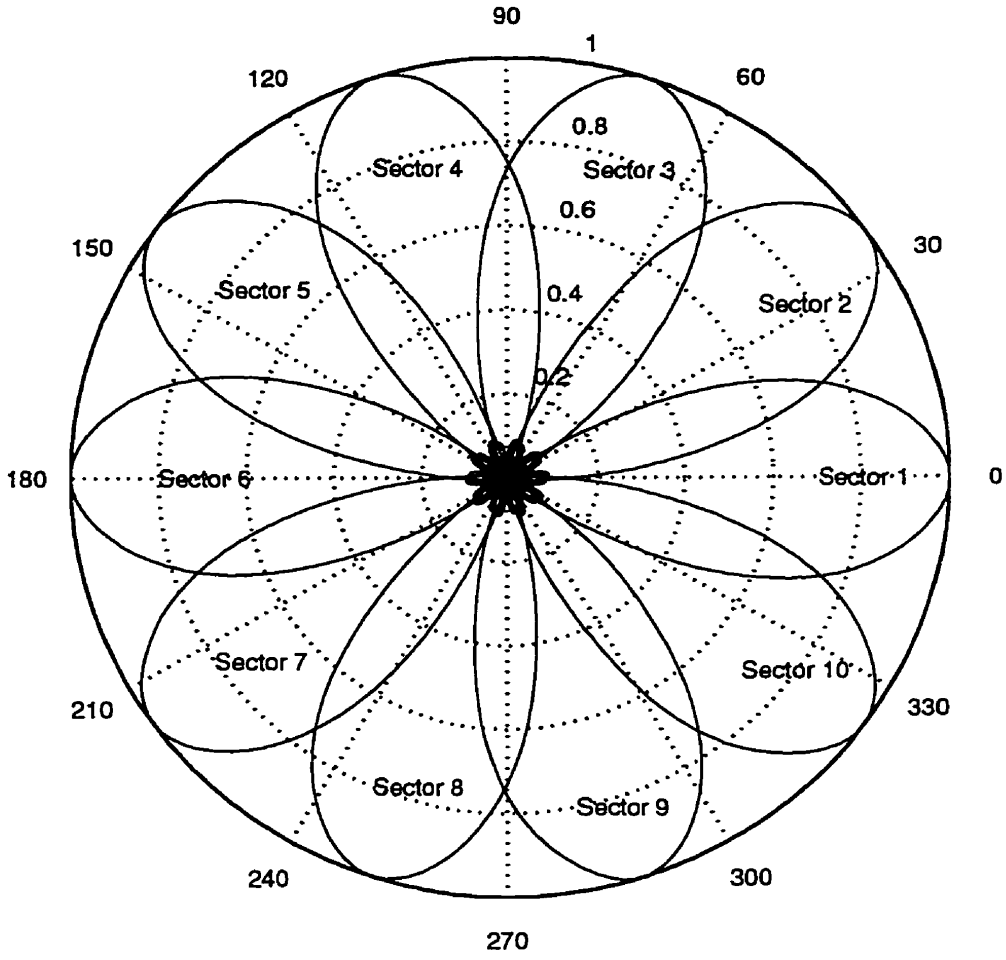

Figure 2.8: Superimposed polar coordinate plots of the ten field strength patterns. Note: the plotted values were normalized by making the maximum value equal to 1.0.

measured. Therefore approximately 40 frequency samples were measured per channel. The results were then stored in computer files for subsequent analysis. For example, Figure 2.9 shows the plot of the data stored in file P8S4, obtained when the transmitter was located in position 8 (P8) of one of the indoor locations and the horn antenna was pointed towards sector 4 (S4). It also shows the plot of the data stored in file P8S7, which was obtained in the same indoor location and with the transmitter in the same position, but with the horn antenna pointed towards sector 7 (S7).

The data in each file were then used to obtain the $G_{p,s}$ value by averaging over the 40

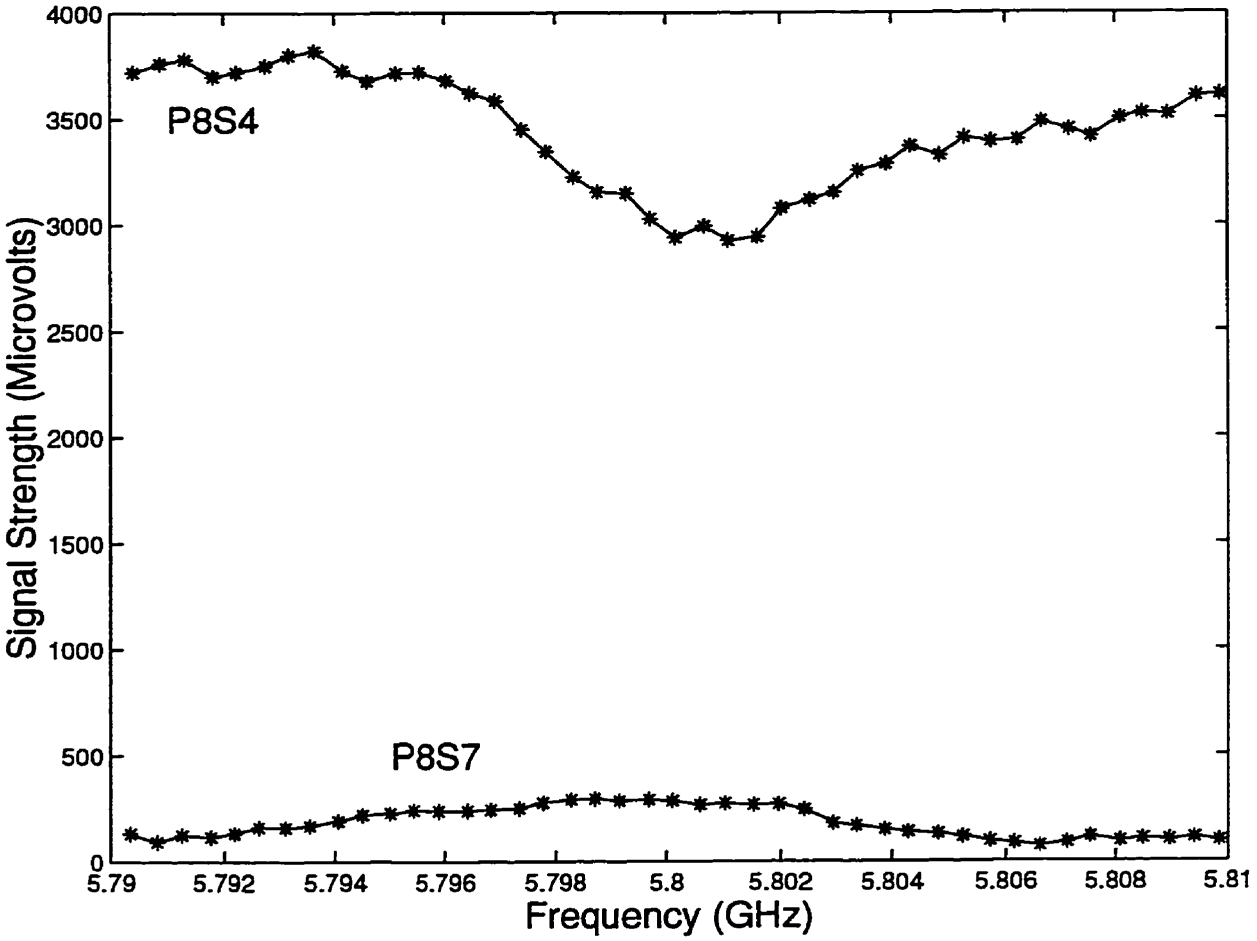

Figure 2.9: The plots of the data in files P8S4 and P8S7

frequency samples:

$$G_{p,s} = \frac{1}{40} \sum_{n=1}^{40} H_n^2, \tag{2.5}$$

where H_n represents the signal strength of the n-th frequency sample. For example, with the data plotted in Figure 2.9 we can compute the values of $G_{8,4}$ and $G_{8,7}$. Table 2.1 shows the $G_{p,s}$ values for some of the positions (portables) in one of the measured indoor locations.

Portable	Antenna Sector Number									
(Position)	1	2	3	4	5	6	7	8	9	10
1	-64.0	-54.9	-68.8	-52.1	-38.3	-53.5	-63.1	-55.3	-59.7	-65.1
7	-63.5	-39.9	-50.3	-51.3	-61.2	-61.2	-61.8	-63.7	-54.4	-63.0
10	-42.3	-43.0	-59.0	-63.1	-56.1	-57.9	-58.0	-58.8	-58.3	-54.8
15	-48.6	-62.7	-46.2	-50.3	-60.3	-59.5	-56.9	-54.6	-44.3	-51.0

Table 2.1: $G_{p,s}$ values (in dBm) obtained for some of the positions measured in indoor location 2

2.5 Measured Indoor Locations

Measurements were taken at three different indoor locations. The first location was the southwest section of the fourth floor of the Galbraith Building located in the University of Toronto Campus. This location is depicted in Figure 2.10. It represents a closed indoor environment where the walls are made of a hard material, in this case concrete blocks.

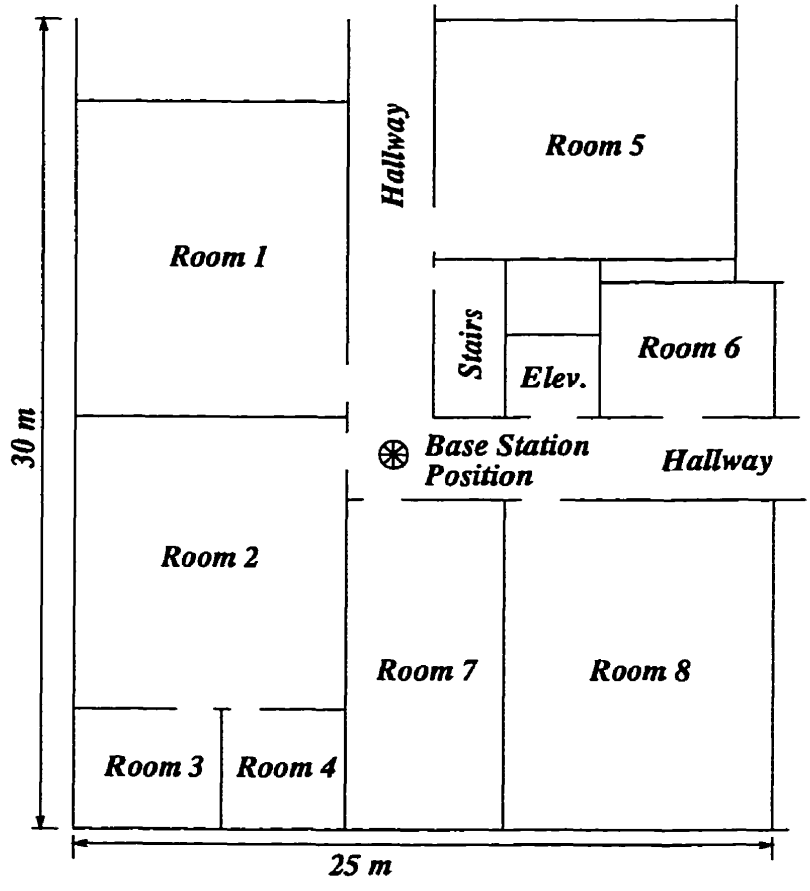

Figure 2.10: Indoor Location 1

For this location, 50 uniformly distributed positions were measured. The following table shows the number of positions measured within each room.

Room	1	2	3	4	5	6	7	8
Number of measured positions	10	8	1	1	9	4	5	12

The second location was an 10×11 m^2 room (room GB402 in Galbraith Building) divided into cubicle offices with soft material partitions. This room was chosen to represent a semi-open indoor environment. For this location, 20 positions were measured, each corresponding to the interior of one cubicle office.

The third location was a 10×11 m^2 classroom (room GB404 in Galbraith Building) furnished mainly with desks and chairs. This room was chosen to represent an open indoor environment. For this location, 36 uniformly distributed positions were measured.

We took the precaution of performing the measurements during the night, which ensured static channels. This was a requirement since the measuring experiment could not account for channel dynamics. Therefore, it is important to state that the results reported in this thesis assume that the indoor channels are static. We expect, however, that the proposed technique would work well with quasi static indoor networks, where changes in the portable-sector power gain parameters ($G_{p,s}$) can be satisfactorily tracked by the base station.

For all locations, the horn antenna (base station simulator) height was 2.2 m and the omni-directional antenna (portable simulator) height was 1.1 m. The spectrum analyser was set to operate with a resolution bandwidth of 3 kHz, ensuring that only negligible noise was added to the received signal.

2.6 Measurement Results

In this section we present the measurement results in terms of average compatibilities which we define as follows.

The average compatibility between two portables is given by

$$AC2 = \frac{1}{\binom{N_p}{2}} \sum_{i=1}^{N_p} \sum_{j=i+1}^{N_p} I(i,j), \tag{2.6}$$

where N_p is the number of portables registered with the base station, and $I(i,j)$ is defined

for portable i and j as

$$I(i,j) = \begin{cases} 1, & \text{if portables } i \text{ and } j \text{ satisfy compatibility condition.} \\ 0, & \text{otherwise.} \end{cases} \tag{2.7}$$

Here, $AC2$ represents the fraction of all two portable combinations that correspond to compatible pairs. Therefore it represents the probability of two randomly picked portables being compatible.

The average compatibility among three portables is given by

$$AC3 = \frac{1}{\binom{N_p}{3}} \sum_{i=1}^{N_p} \sum_{j=i+1}^{N_p} \sum_{k=j+1}^{N_p} I(i,j,k), \tag{2.8}$$

where $I(i,j,k)$ is defined for portable i, j and k as

$$I(i,j,k) = \begin{cases} 1, & \text{if portables } i,\ j \text{ and } k \text{ satisfy compatibility condition.} \\ 0, & \text{otherwise.} \end{cases} \tag{2.9}$$

Here, $AC3$ represents the fraction of all three portable combinations that correspond to compatible triples. Therefore it represents the probability of three randomly picked portables being compatible.

Similarly, ACn represents the fraction of all n portable combinations that correspond to compatible subsets of n portables.

Figures 2.11, 2.12 and 2.13 show the results obtained in the up-link case for locations 1, 2 and 3, respectively. The average compatibilities $AC2$, $AC3$ and $AC4$ are plotted as functions of the capture threshold. The solid curves are the results obtained when the transmitting power of each portable is adjusted so that the base station receives the same average power from each portable through its best sector. As explained in a previous section, the use of power control can eliminate stronger interference with peripheral portables caused by signals from portables close to the base station. Therefore, as expected, we obtained higher average compatibilities with the use of power control.

Figures 2.14, 2.15 and 2.16 show the average compatibilities obtained in the down-link case for locations 1, 2 and 3, respectively. In the down-link case, assuming that the same

power level is transmitted to all the portables, we obtained average compatibilities close to those obtained in the up-link case with power control.

In order to understand the meaning of these measurement results, let us assume a multiple access scheme in which a base station operating with a sectored antenna system like that shown in Figure 2.5 allocates packets in time slots in order to transmit them to portables in the microcell. Let us also assume that there is no compatibility verification in this process, i.e, packets are picked randomly. Therefore, when two or more packets are transmitted in the same time slot, they may be received with errors if the receiving portables are not compatible, and in this case we say that a collision occurs. The probability that a time slot is collision-free depends on the number of packets transmitted in this time slot. This probability is the average compatibility among the portables. Consider for example a capture threshold of 10 dB in Figure 2.14. In this case the probability of a collision-free time slot is approximately 0.4 if two packets are transmitted together, and approximately 0.04 if three portables are transmitted together. We may conclude that such a multiple access scheme would provide poor throughput due to the small likelihood of collision-free transmissions. In the next chapter we propose a multiple access scheme that verifies compatibility among the portables in order to avoid simultaneously transmitting packets that can jam each other. We will see that such a scheme can significantly improve the throughput compared with the one-port case described in [5] and [6].

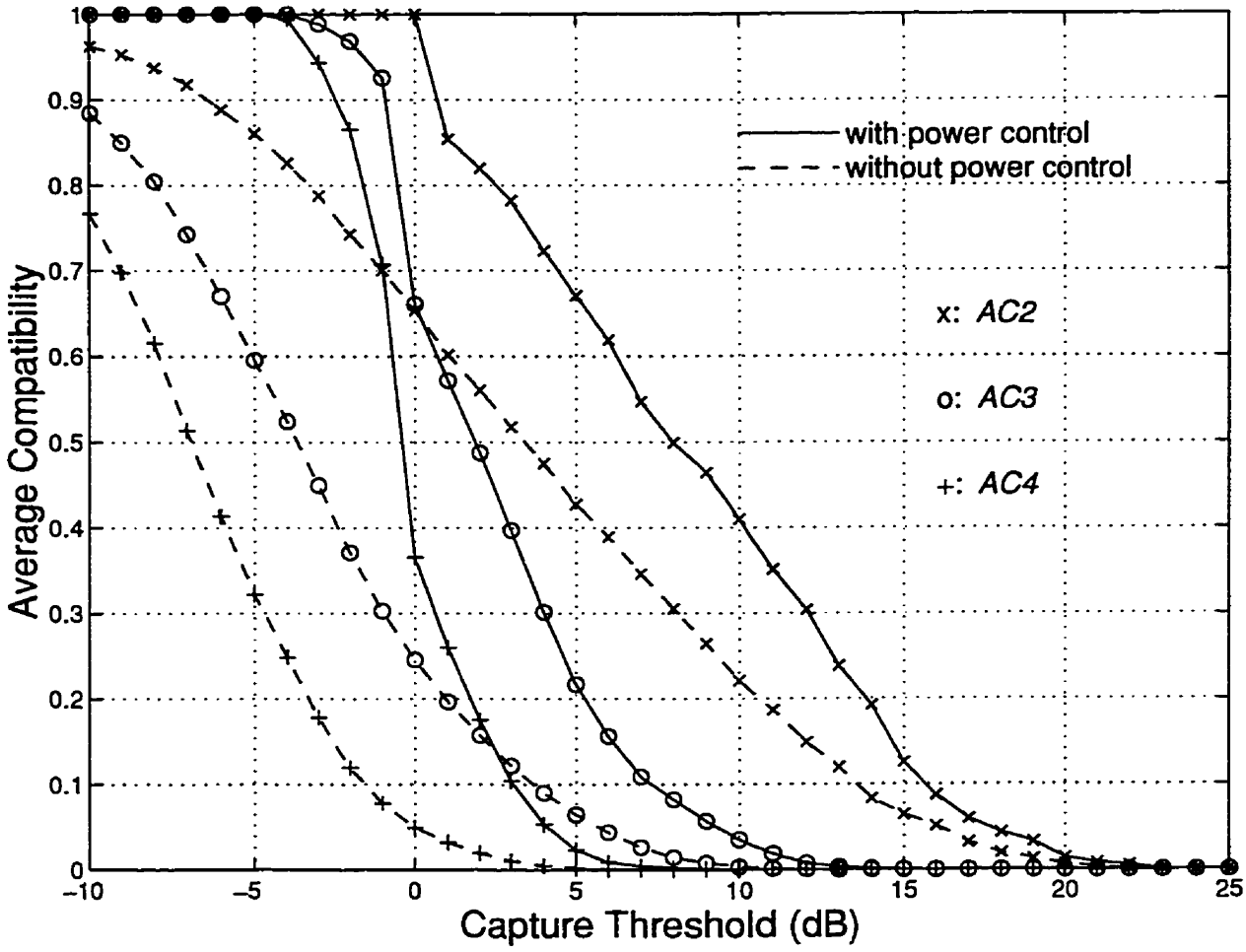

Figure 2.11: Up-link average compatibilities in location 1

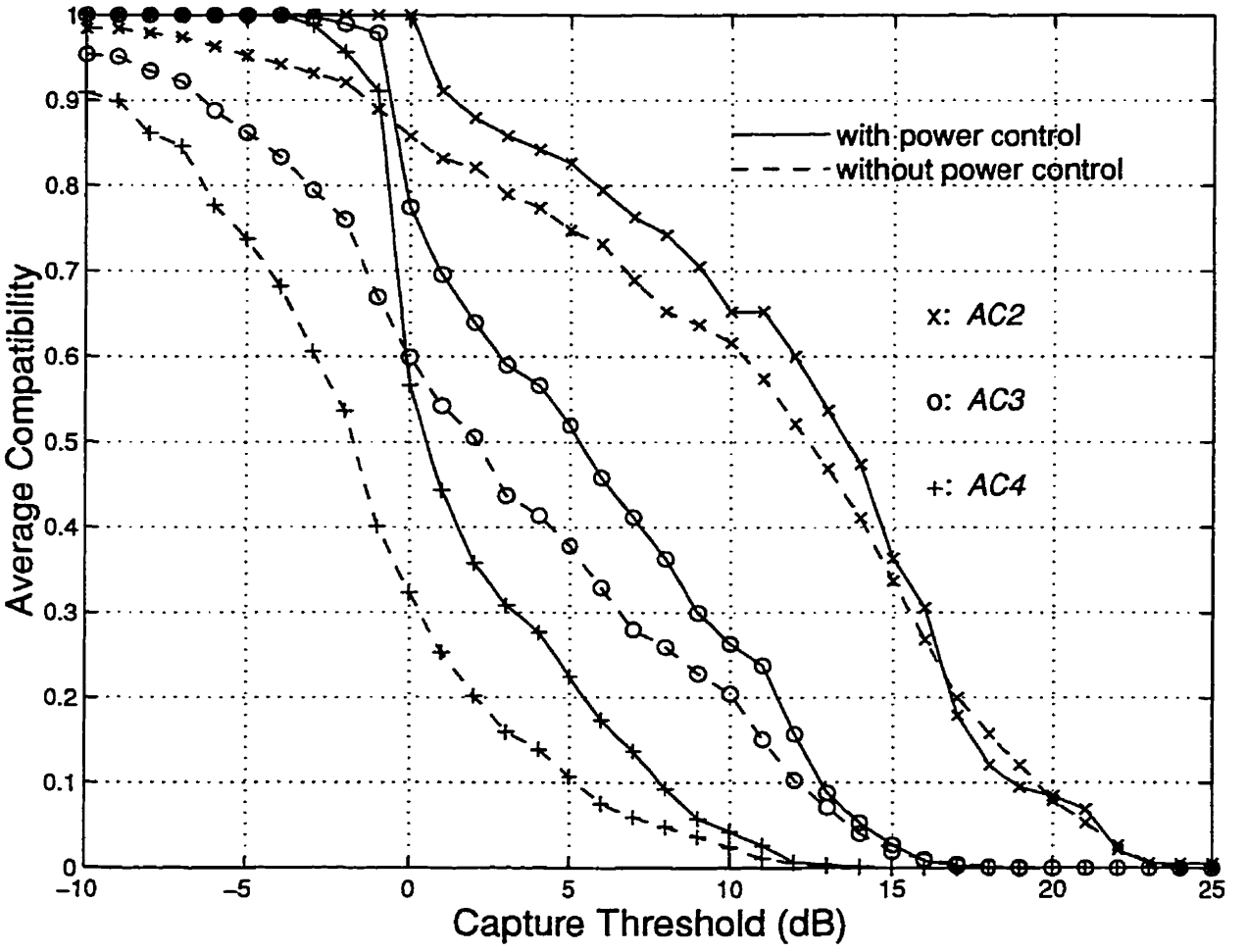

Figure 2.12: Up-link average compatibilities in location 2

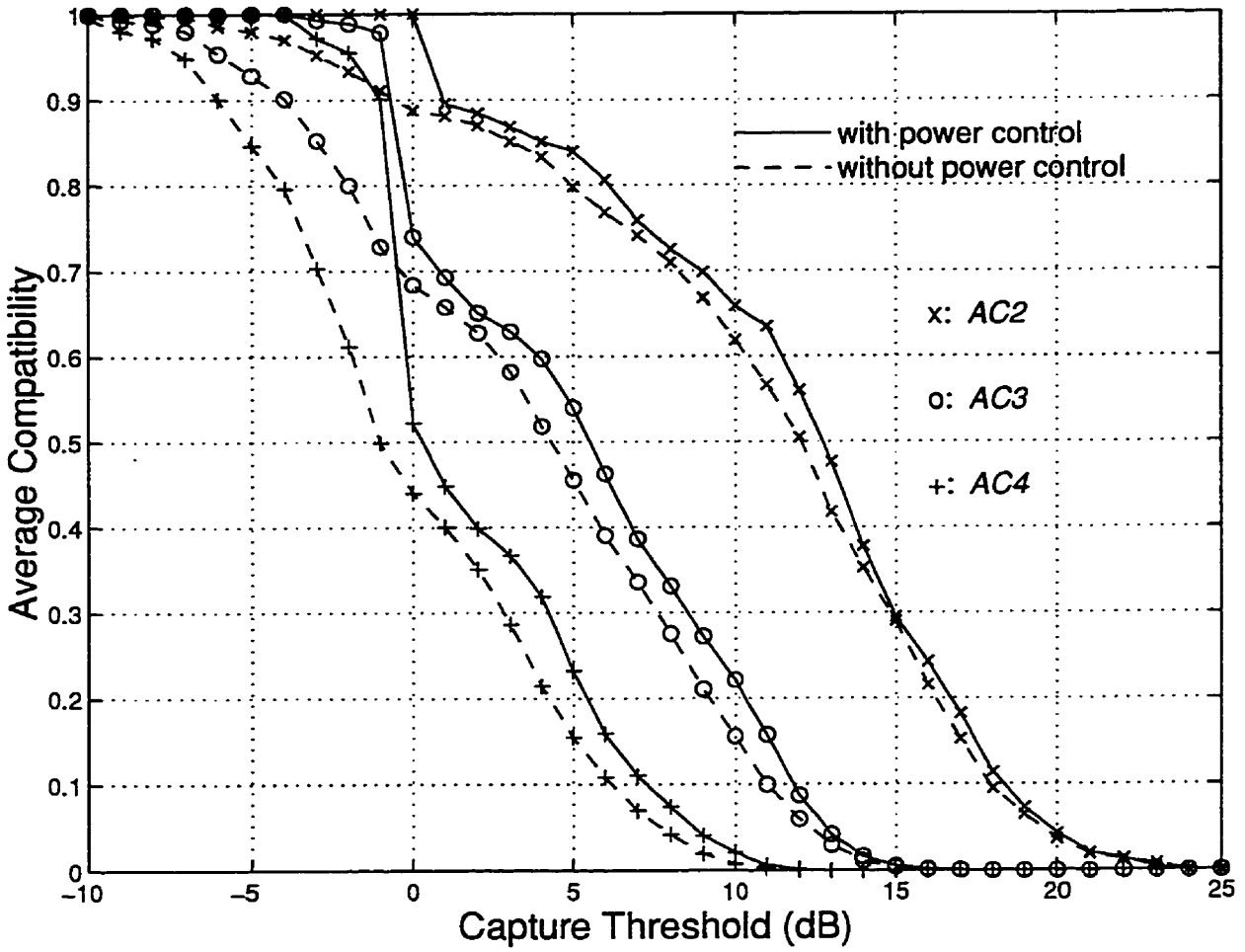

Figure 2.13: Up-link average compatibilities in location 3

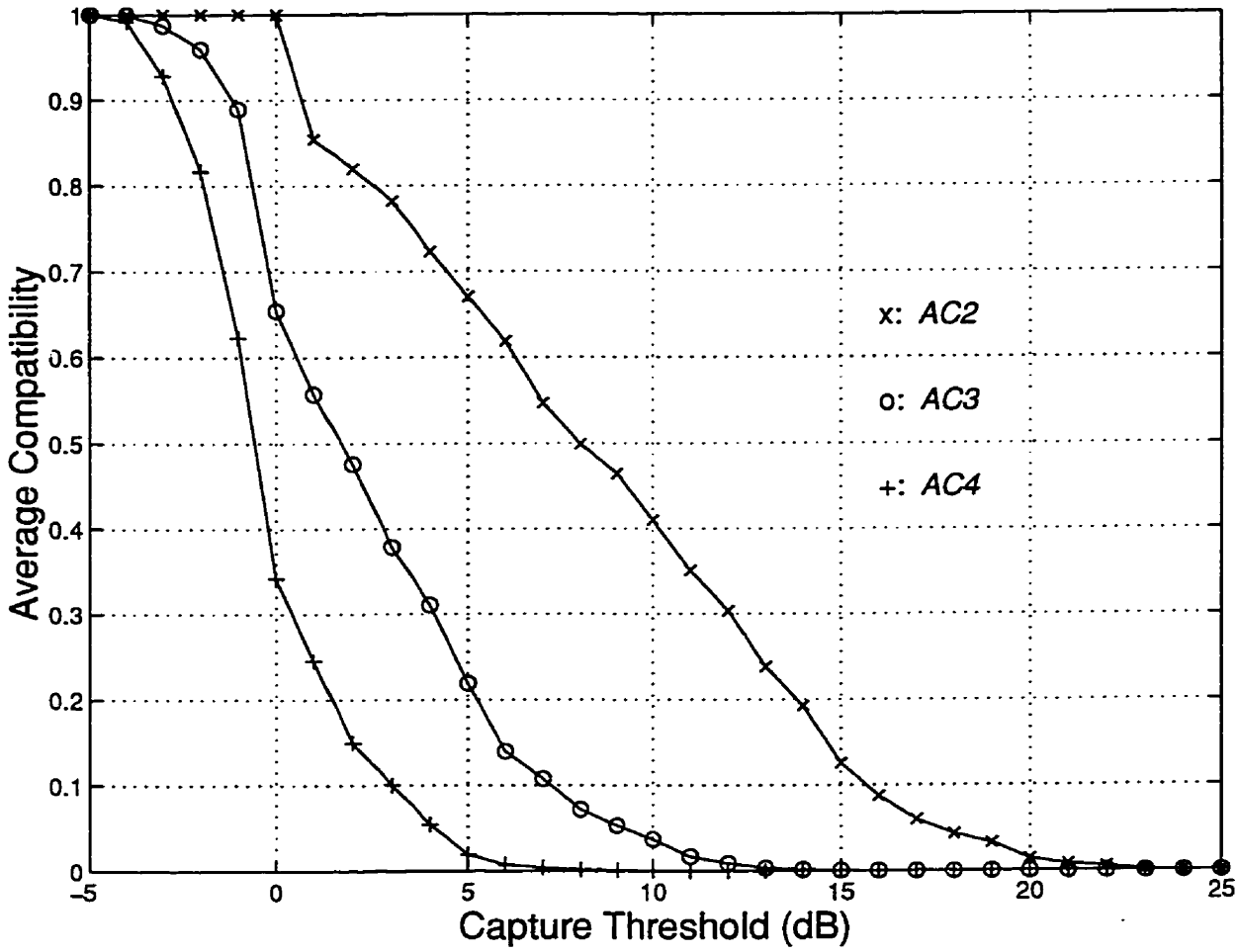

Figure 2.14: Down-link average compatibilities in location 1

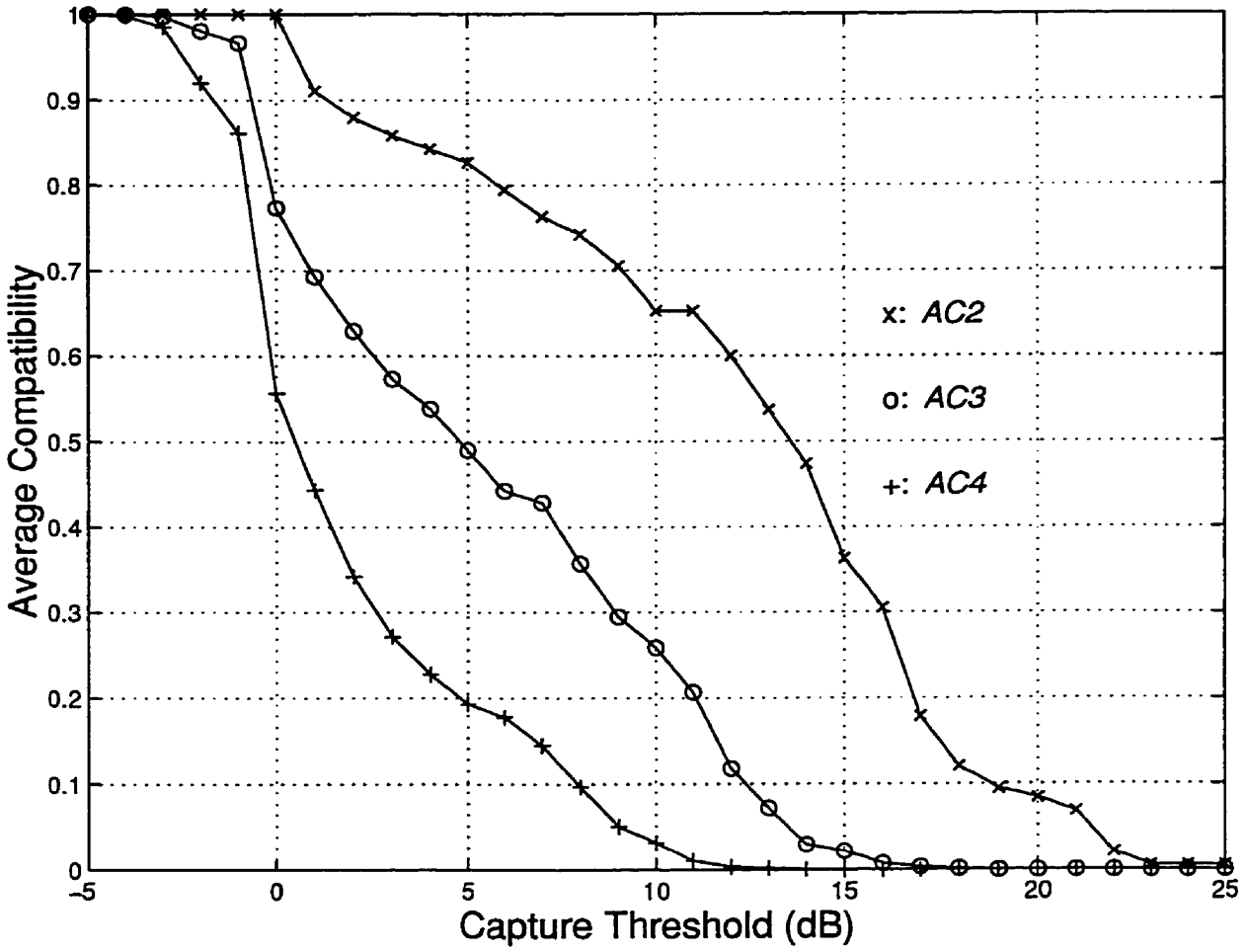

Figure 2.15: Down-link average compatibilities in location 2

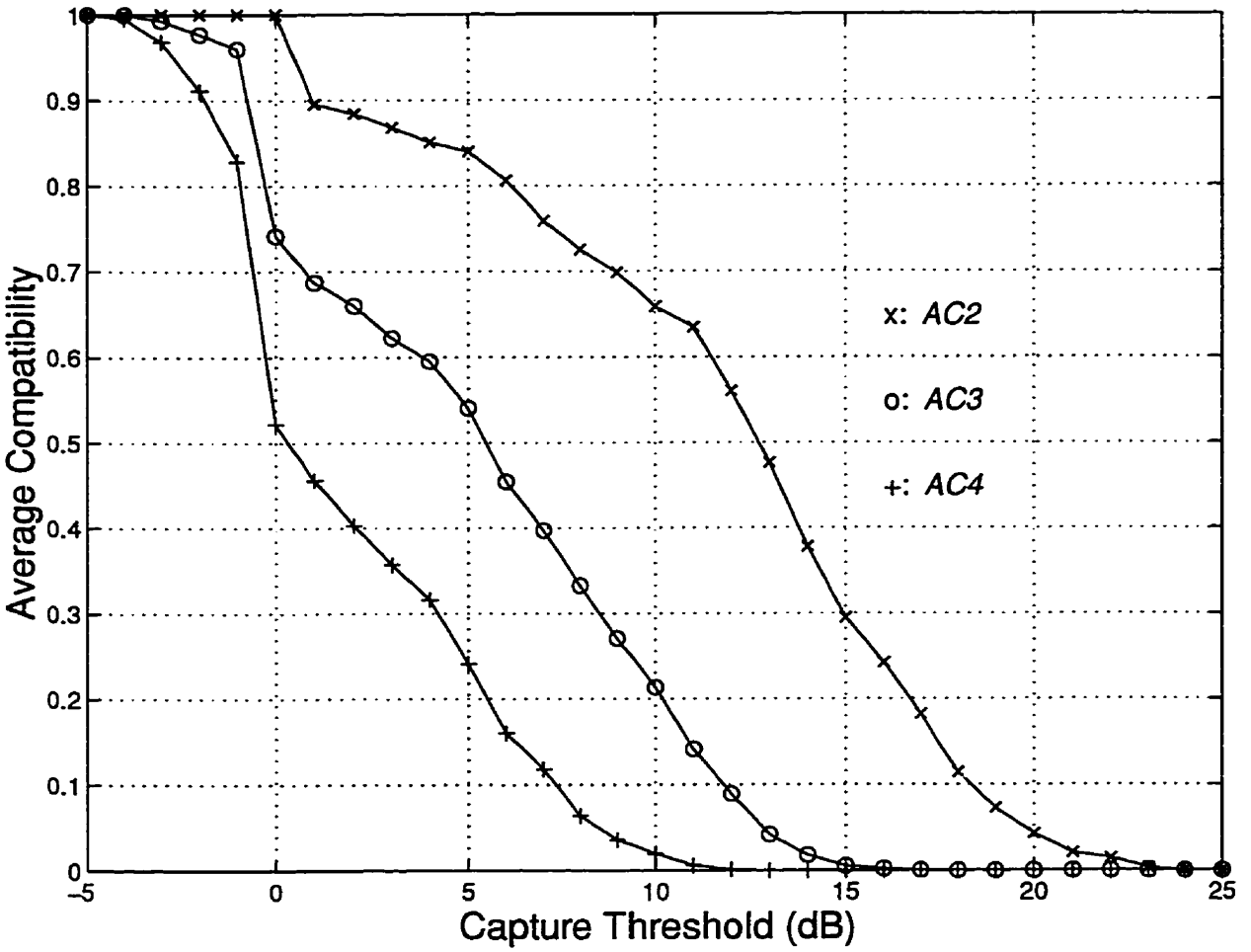

Figure 2.16: Down-link average compatibilities in location 3

Chapter 3

Antenna Sector-Time Division Multiple Access

3.1 Introduction

In this chapter we propose a new multiple access scheme that is able to take advantage of the compatibilities among portables in an indoor microcell, defined in the previous chapter, in order to increase system capacity. This can be done by properly scheduling simultaneous transmissions of packets that belong to compatible portables. Figure 3.1 depicts the scenario where scheduling is performed. It shows that the base station has a buffer where packets collected from a high speed wireline backbone network are temporarily stored while waiting to be transmitted to their destination portables during down-link time slots. It also shows that each portable has a buffer that temporarily stores packets generated in the end-user terminal equipment and are waiting to be transmitted to the base station during granted up-link time slots. The scheduling problem consists in finding among the awaiting packets those that can share a time slot in the next frame, namely, those that belong to compatible portables.

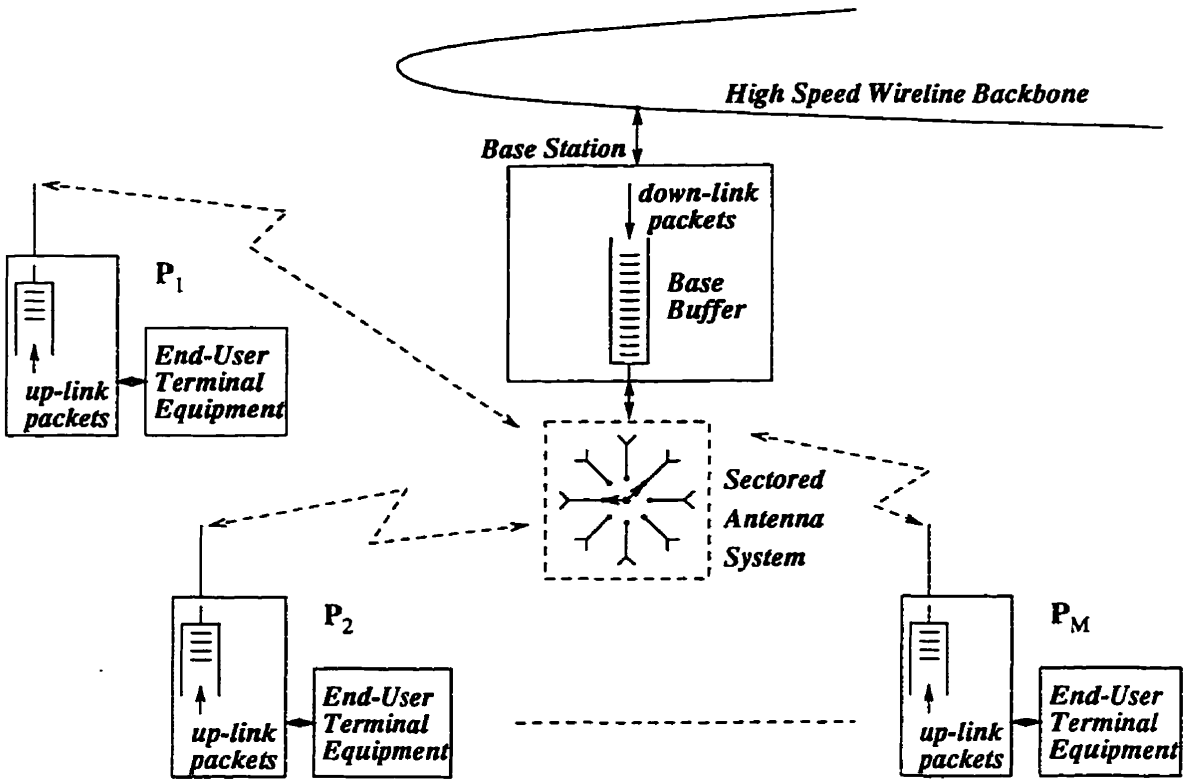

Figure 3.1: A microcell with its base station and portables

3.2 Frame Scheduling

In this section we make use of an example of a two-port frame schedule in order to explain the frame scheduling problem. Let us suppose that Figure 3.2-a represents the values of the $G_{p,s}$ parameters, as defined in Chapter 2, related to the portables and the base station of Figure 3.1. The values quoted in this figure were chosen for illustrative purposes. With these values, the two by two compatibility relations among the portables can be obtained, as shown in Figure 3.2-a for a capture threshold of 10 dB, where "1" means compatibility and "0" means incompatibility. Let us also suppose that a 2-port frame has been scheduled using these compatibility relations. Figure 3.3 represents this frame with its down-link and up-link portions. Here, the word "port" is used to denote a port in the sectored antenna system which can be switched to any one of the antenna sectors. Therefore, in this figure, the base station operates with a two-port sectored antenna system as shown

in Figure 2.1-b. The frame is composed of a number of equal time slots, each capable of carrying one packet per port. Thus, with the two-port antenna system, a maximum of two packets can be transmitted per time slot. For example, each packet could transport one ATM (Asynchronous Transfer Mode) cell [11] plus some wireless overhead. The packet owners and the sectors being used for the transmission of each packet are also shown in this Figure 3.3. The first time slot of the down-link sub-frame carries two packets, one for $\mathbf{P}_1$ and the other for $\mathbf{P}_3$. For each packet, the base station uses the antenna sectors that provide the best signal level, namely, sectors 2 and 6. The time slot and frequency spectrum sharing between a $\mathbf{P}_1$ packet and a $\mathbf{P}_3$ packet is possible because of the compatibility between their owners.

Portables	Base Station: Sec1	Sec2	Sec3	Sec4	Sec5	Sec6	Sec7	Sec8
P_1	-50	-5	-32	-100	-10	-20	-50	-40
P_2	-40	-10	-20	-4	-60	-56	-15	-41
P_3	-23	-50	-10	-20	-6	-4	-20	-38

P_M	-3	-23	-42	-12	-34	-21	-15	-100

(a) $G_{i,S}$ (dBm) Table

Portables \ Portables: 1	2	3	-----	M
1	0	0	1	-----	1
2	0	0	1	-----	0
3	1	1	0	-----	1
⋮	⋮	⋮	⋮	⋮	⋮
M	1	0	1	-----	0

(b) Compatibility Matrix

Figure 3.2: (a) $G_{p,s}$ parameters; and (b) Matrix of compatibility of pairs of portables in the microcell in Figure 3.1

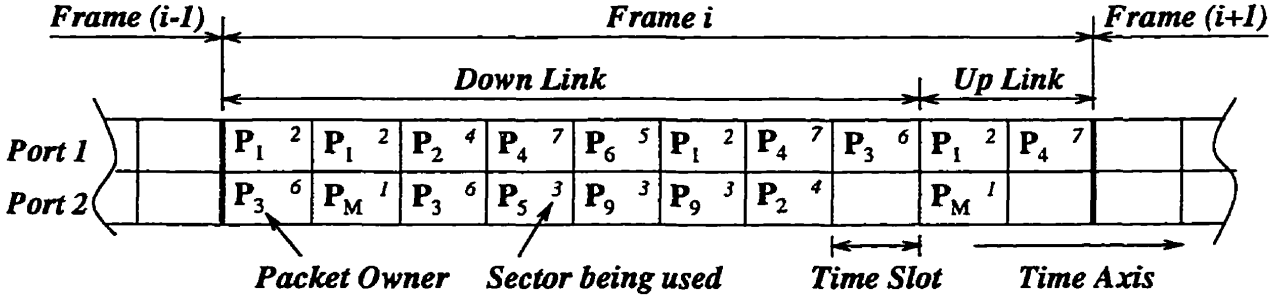

Figure 3.3: A frame schedule for two ports

We propose that up-link and down-link modes use the same frequency spectrum (Time Division Duplex). This guarantees reciprocity between up-link and down-link channels, allowing the $G_{p,s}$ parameters to be used for both down-link and up-link compatibility verification with the conditions defined in (2.1) and (2.2), respectively. Up-link/down-link traffic does not need to be symmetrical. In fact it is expected that the up-link traffic will be a small fraction of the down-link traffic. This is the case, for example, for the current traffic in the Internet where the down-loading of files generates highly asymmetrical traffic. Accordingly, the down-link subframe in Figure 3.3 was made intentionally larger than the up-link subframe for illustrative purposes.

It is assumed that scheduling is performed in the base station (central control architecture). For this purpose the base receives updated information about the compatibility relations among the portables and about the number of packets waiting transmission in each buffer. For Variable Bit Rate (VBR) services, the number of packets that arrive in the portables' buffers and in the base station's buffer during one frame duration varies from frame to frame. This means that each new frame requires its own scheduling. Therefore the time available for scheduling each frame is one frame duration: during the transmission of the i-th frame, the base station is working out the scheduling of the $(i+1)$-th frame, which has to be ready for transmission before the end of the i-th frame transmission.

Now a simple example is used to demonstrate that frame scheduling may be optimized in order to allocate a maximum number of packets. Figure 3.4-a describes the compatibility relations of 4 portables. Figure 3.4-b shows a non-optimum frame scheduling. It can be seen that portables 1 and 2 can share the first time slot because they are compatible. However, portables 3 and 4 are not compatible, so a portable 4 packet could not be allocated together with the portable 3 packet in the second time slot. Figure 3.4-c shows a better way to perform scheduling. By allowing portable 1 to share the first time slot with portable 3, an opportunity was created for portable 2 to share the second time slot with portable 4, resulting in more efficient scheduling.

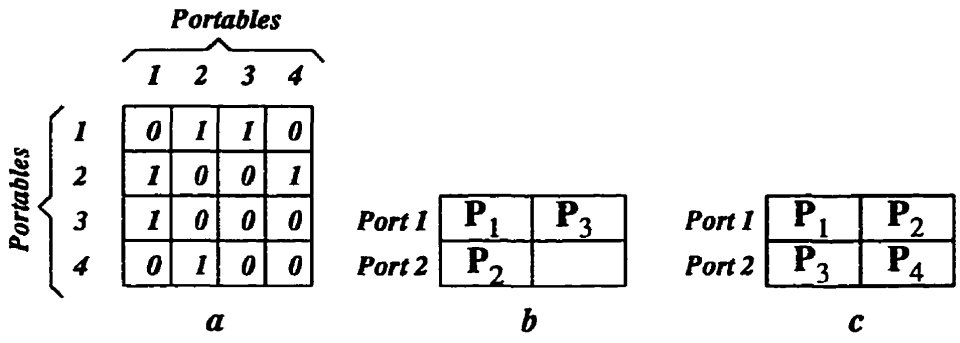

Figure 3.4: (a) Compatibility relations among 4 portables; (b) A non-optimum frame schedule; (c) Optimum frame schedule

3.3 First Fit Algorithm

The necessity of solving the scheduling problem in less than one frame duration was stated in the previous section. However, it turns out that for the N-port case ($N \geq 3$), the optimum scheduling problem is in the **NP**-Complete class of problems (problems that can not be solved in polynomial time, or **N**on **P**olynomial problems). The practical result is that, for a large number of packets, solving it in real time becomes impractical.

The NP-Completeness of this problem is proved for the case of $N \geq 3$ in the appendix. The 2-port optimum frame scheduling problem is a special case that requires further investigation to determine if it belongs to the **NP**-complete class or if it belongs to the **P** class (problems that can be solved in polynomial time [10]). However we prefer to concentrate on finding a sub-optimum frame scheduling solution that fits the generic N-port case, and that can be solved in real time. This sub-optimum solution is the First Fit Algorithm (FFA) that we describe below.

The FFA can be better explained with the help of Figure 3.5. This algorithm places the packets into the time slots one at a time in the order that they arrive in the buffer. It does so according to the following simple rules:

1. First the algorithm fills the time slots of the first port. If after performing this step there are still packets left in the buffer, then it goes to the following steps.

2. For allocating packets in ports 2 and up, the algorithm always places the next packet of the buffer into the lowest-indexed time slot containing only packets that are compatible with the packet being allocated. The conditions of compatibility are given by (2.3) for the down-link case and by (2.4) for the up-link case, where N is such that $N-1$ is the number of packets already allocated in the time slot. When searching for the lowest-indexed time slot, the port index has priority over the time slot index. Therefore the algorithm looks first for a time slot in port 2, and if it can not find a valid time slot, then it looks for one in port 3, and so on. This helps to distribute packet transmissions evenly across time.

3. If a packet does not fit in any of the time slots of this frame, then the algorithm leaves it to be transported in the next frame and tries to allocate the next packet of the buffer by going back to step 2.

4. The algorithm repeats steps 2 and 3 until all the packets of the buffer are considered or until the frame is full.

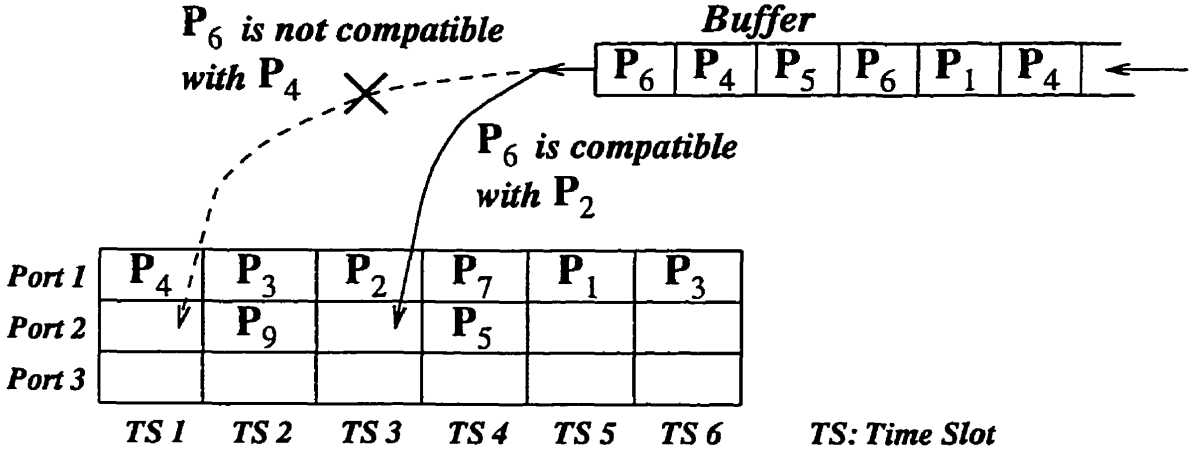

Figure 3.5: The First Fit Algorithm

In the scheduling of down-link packets, the packets are stored in the base station's buffer while awaiting transmission, so the FFA operates in a local buffer. However, in the scheduling of up-link packets, the buffer is distributed in the sense that it is composed of

all the portables' buffers. In this case the base station has to receive updated information about the number of packets awaiting transmission in each portable buffer, so that the distributed buffers can be operated in conjunction as if they were a single buffer.

The FFA serves the packets according to their order of arrival in the buffer. However, this algorithm could be modified in order to serve packets according to some policy that privileges real time services. See [12] for example.

3.4 Frame Structure

It has been assumed that the base station keeps updated information about the compatibility conditions among the portables and about the number of packets awaiting transmission in each buffer. In this section we propose a frame structure with overheads that allow the base station to acquire and update this information. Figure 3.6 shows this frame structure.

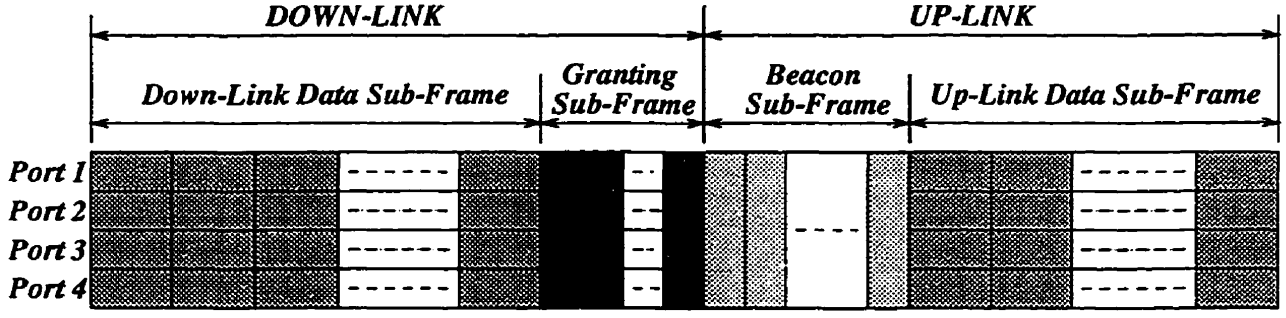

Figure 3.6: A proposed frame structure

In this frame structure, the time slots of the *Up-Link Data* and *Down-Link Data* sub-frames are used to transport data packets (for example, ATM cell + wireless overhead $\simeq$ 500 bits) in the down-link and up-link directions, respectively.

The *Granting Sub-Frame* is used to transport control packets from the base station to the portables. Its function is to transport information that lets portables know when they are allowed to transmit in the Up-Link Data Sub-Frame, i.e, this sub-frame is used to inform the portables of the result of the current up-link frame schedule.

Every portable which is registered with the base station has a reserved time slot every N_F frames in the *Beacon Sub-Frame*. Therefore the number of time slots in this sub-frame are

$$N_{ts} = \frac{M_{max} + 1}{N_F} \tag{3.1}$$

where N_{ts} is the number of time slot in this sub-frame, and M_{max} is the maximum number of portables allowed to register with the base station. For example, if $M_{max} + 1 = 100$ (one of these time slots is reserved for registering new users, as explained below), and if $N_F = 20$ then this sub-frame is composed of five time slots, so each portable can transmit during one of them every 20 frames. The Beacon Sub-Frame has three functions as follows:

- It allows the base station to acquire the portable-sector power gain ($G_{p,s}$) values, which describe the average power received by each of its antenna sectors during the portable transmission. Note that a single portable transmits during one of these time slots. This information is used to generate a table of average received power per antenna sector, per portable as in Table 2.1. Then from this table the base station obtains the compatibility relation among the portables.

- During these time slots, the portables inform the base station about the number of packets waiting in their buffers.

- Once every N_F frames, one of these time slots is used in a slotted ALOHA protocol in order to admit (register) new portables to the microcell.

The value of N_F is a trade-off depending on bandwidth efficiency, *reaction time*, and *adaptability rate*. Reaction time is the delay before a portable informs the base station that a new packet has arrived in its buffer. The adaptability rate is related to how fast the base station can react to changes in the indoor location (changes in the compatibility relations among the portables). For example, let us suppose that the frame duration is 1 ms and that $N_F = 100$ and $M_{max} + 1 = 100$. In this case the Beacon Sub-Frame is composed of a single time slot ($N_{ts} = 1$) which gives each portable the opportunity to inform the base

station about its buffer state once every 100 frames, or every 100 ms, yielding a reaction time of 100 ms. This means the base station can adapt to changes in the compatibility relation among the portables once every 100 ms. In order to improve the reaction time and the adaptability rate, the value N_F has to be decreased. For example, making $N_F = 10$ would demand more bandwidth (10 time slots per frame) but would improve reaction time to 10 ms and adaptability rate to 1/(10 ms).

3.5 First Fit Algorithm Simulations

Simulations were run in order to evaluate the FFA performance in the three measured locations. Only up-link traffic was simulated, and performance was evaluated with and without power control. The power control mechanism consisted in adjusting the measured power levels in order to equalize, for all portables, the power level received through the best antenna sector to communicate with a given portable. This is illustrated in Figure 2.2-c.

The traffic model used in these simulations was a well behaved VBR service in which a new packet for portable i ($i = 1, 2, \ldots M$) arrives in its buffer during a time slot according to the Bernoulli process. It was assumed that the base station had immediate knowledge of a packet arrival.

The simulation results can be seen in Figures 3.7, 3.8 and 3.9, which correspond to locations 1, 2 and 3, respectively. These results were obtained assuming a capture threshold of 10 dB and a frame size of 20 time slots. However it will be shown that the maximum throughput is not dependent on the size of the frame. The frame size affects the latency of the packets though, but this thesis does not investigate packet latency. The objective here is to investigate the FFA maximum throughput when packet delay is not a concern. The curves are for mean buffer occupancy and throughput as functions of the system load, which is the traffic generated by all the M portables where each portable contributes $\frac{1}{M}$ of the total load. Throughput is defined as the average number of packets transported per time slot. From the graphs we can observe that the throughput is equal to the load up to

a point where it saturates. At this point the system reaches its *maximum throughput*, and thus the mean buffer occupancy rises rapidly.

In location 1, the maximum throughput with three ports was around 2.1 without power control and around 2.5 with power control. The results obtained with four ports (not plotted) were not significantly better than those obtained with three ports. The reason can be seen in Figure 2.11, where the value of four by four average compatibility ($AC4$) is practically zero at a capture threshold of 10 dB. However, we should note that the 3-port case with power control was able to provide a maximum throughput of 2.5, even though the three by three average compatibility ($AC3$) was only 0.04 at a capture threshold of 10 dB (see Fig. 2.11).

In locations 2 and 3, the maximum throughput achieved with four ports using power control was around 3.6. The results obtained with five ports (not plotted) were not significantly better.

The use of power control was more effective in location 1 than in locations 2 and 3. This is because, in location 1, there were walls separating portables from the base station. In some cases there were two walls separating them, and in other cases only a door separated them. This worsened the near/far problem in the sense that a portable located on the periphery seemed to be farther, from the signal power level point of view, than was suggested by its physical location.

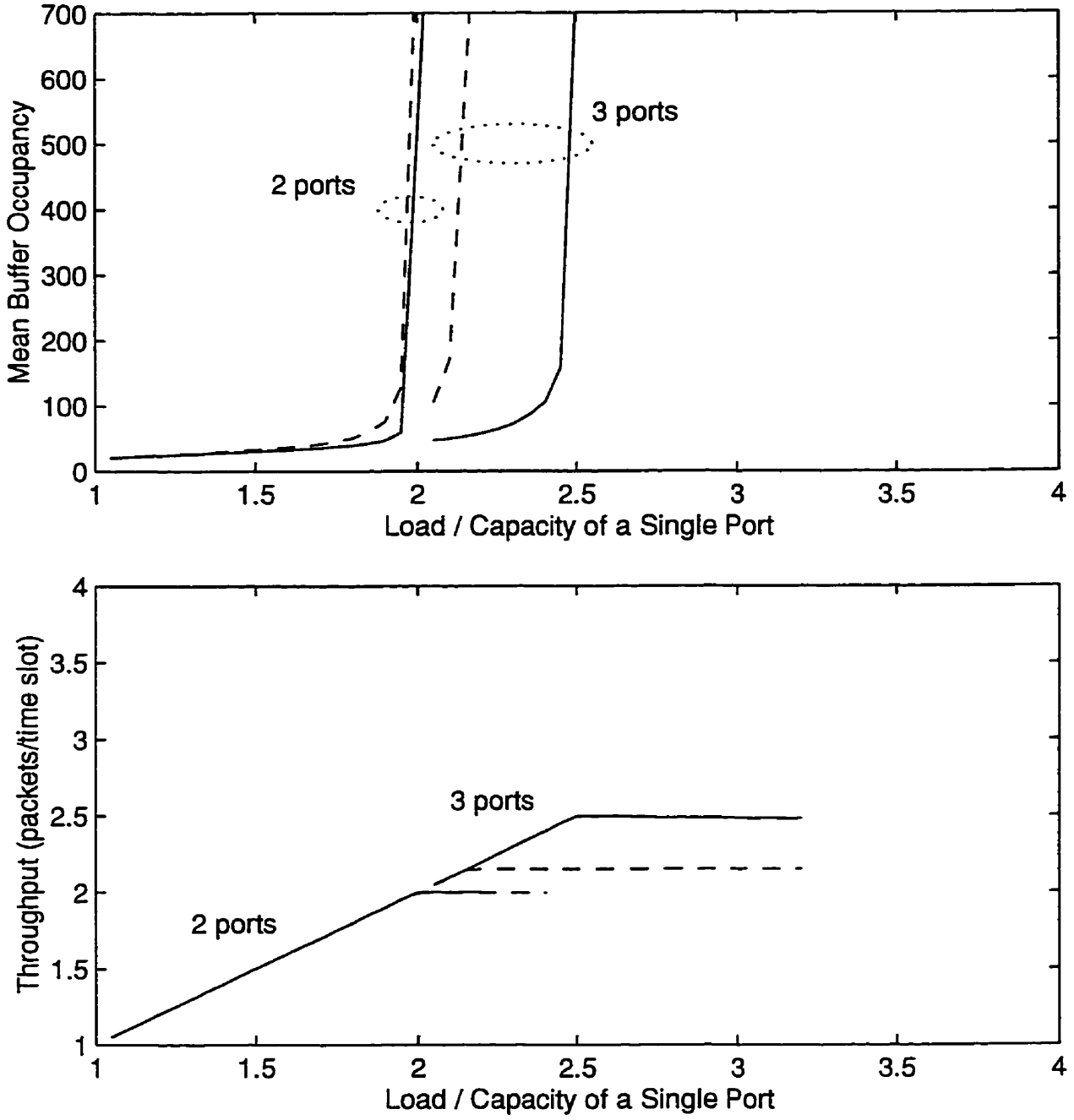

Figure 3.7: FFA performance for up-link traffic in location 1 with power control (solid lines) and without power control (dashed lines)

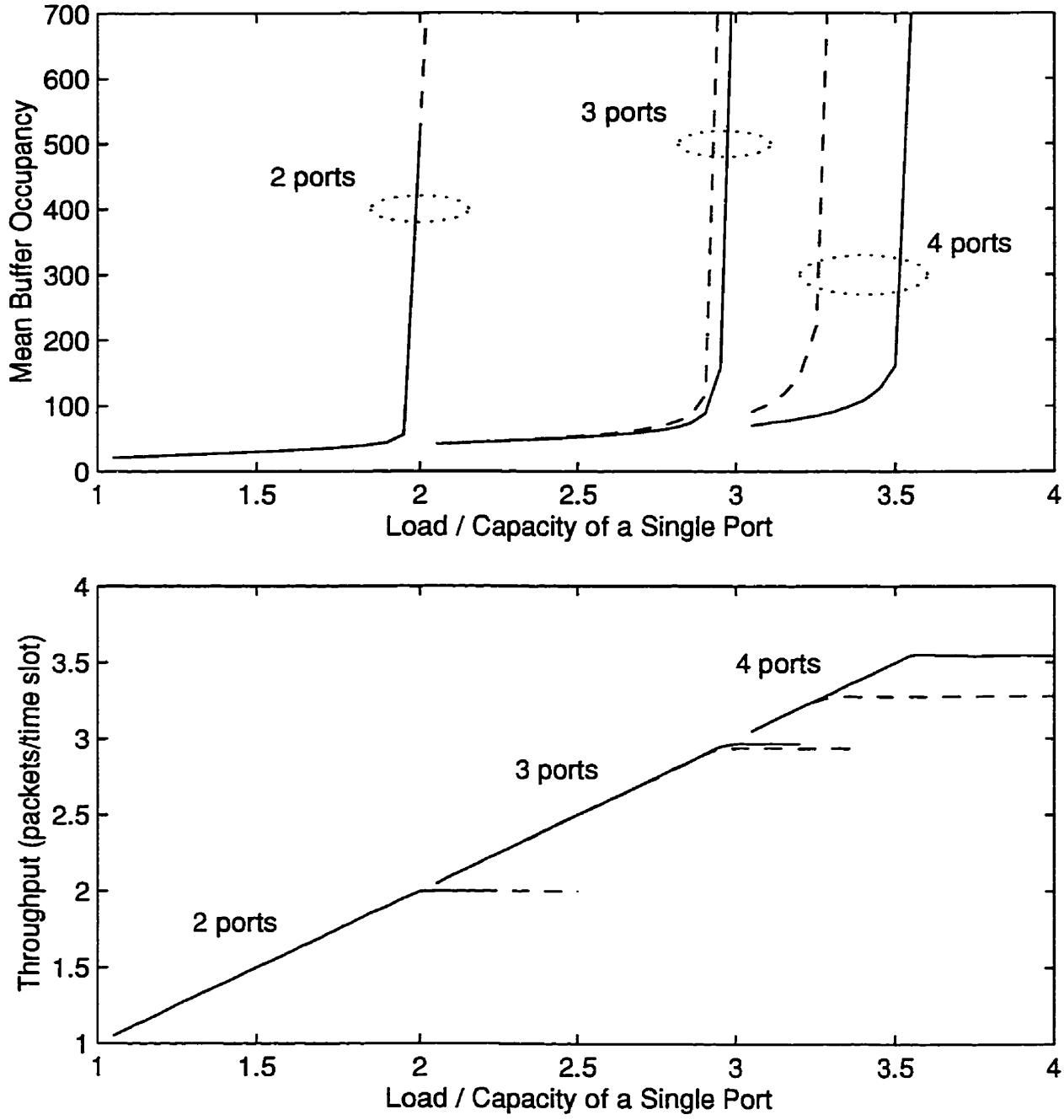

Figure 3.8: FFA performance for up-link traffic in location 2 with power control (solid lines) and without power control (dashed lines)

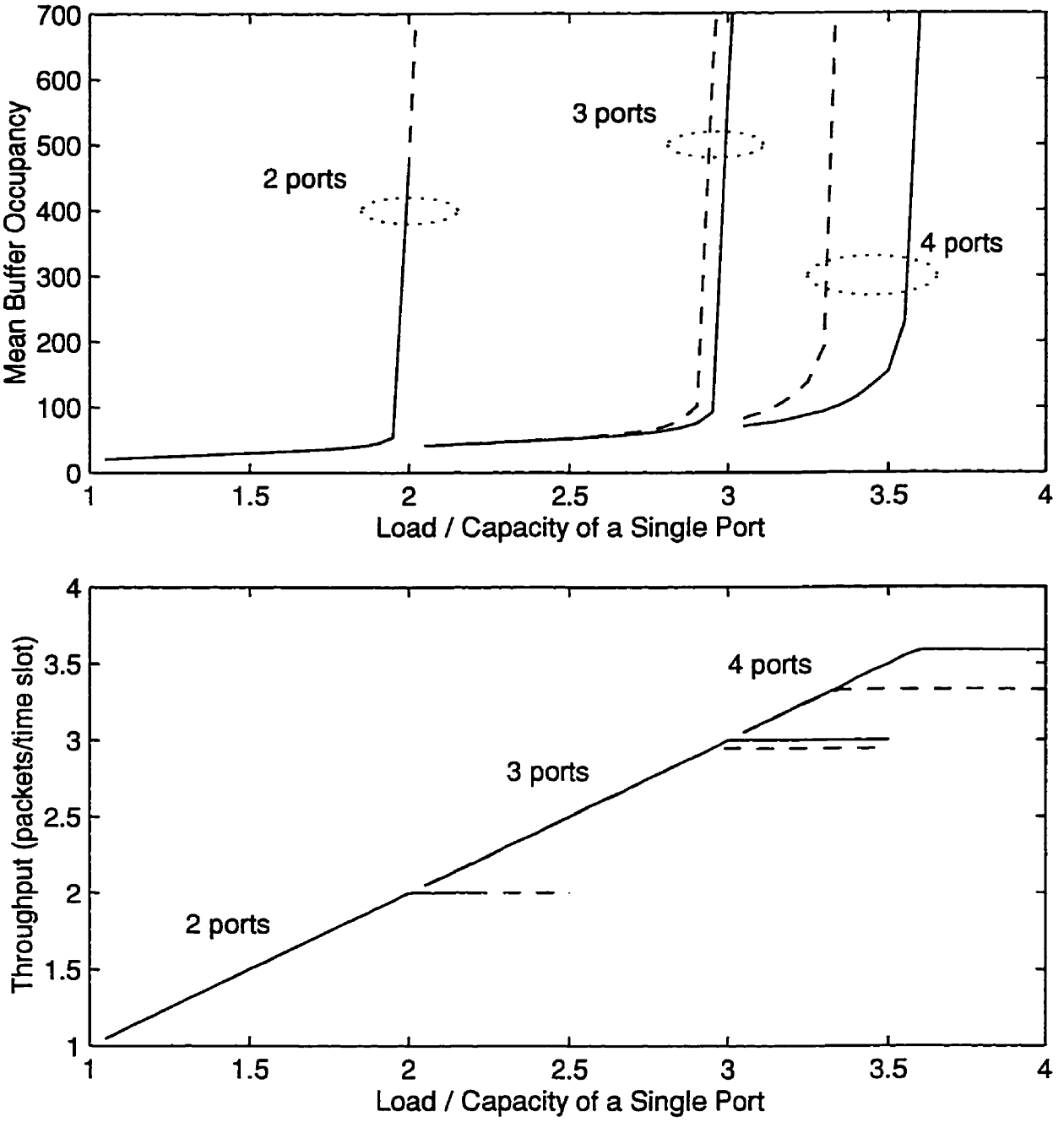

Figure 3.9: FFA performance for up-link traffic in location 3 with power control (solid lines) and without power control (dashed lines)

3.6 FFA Maximum Throughput

The simulation results shown in the previous section assumed well distributed traffic in the microcell where all portables make equal contributions to the total traffic. However it is easy to see that if the traffic is not well distributed in the microcell, then the maximum throughput will decrease. For example, in an extreme case where most of the traffic is generated in a single sector, then the multiple access scheme will not perform much better than the single port scheme of the Motorola ALTAIR system. In this situation, a single port will be used most of the time to transmit or receive packets from portables in this sector, which are not compatible since they are communicating with the same antenna sector. Based on this observation, we define FFA Maximum Throughput in the following way:

FFA Maximum throughput of a microcell is defined as the maximum average number of packets that the FFA can allocate per time slot when the portables of the microcell are uniformly distributed across the sectors, and all make an equal contribution to the total traffic, i.e, the average packet rate of each portable is the same.

This definition assumes that maximum throughput is independent of the type of traffic in the microcell. In fact, any type of traffic will reach the same maximum throughput provided that the buffer is large enough to accommodate a burst of packets, and, of course, provided that these packets can tolerate the resulting queueing delay.

The simulation results shown in the previous section were able to provide the maximum throughput for the three locations assuming a specific capture threshold value of 10 dB. It would be interesting to plot the maximum throughput as a function of the capture threshold. However, running simulations for many values of the capture threshold is time-consuming. Therefore, in order to make the FFA run faster, we simulated the FFA with a frame composed of a single time slot. This provided correct results since the maximum throughput is independent of the frame size, as we now prove:

Theorem: The maximum average number of packets that the FFA can allocate per time slot is independent of the frame size.

Proof: We base this proof on the fact that the FFA, when allocating a packet in a given time slot, verifies its compatibility with the packets already allocated in this time slot, but not with the packets allocated in the other time slots of the frame. Therefore, the maximum number of packets that can be allocated in a given time slot of the frame is not dependent on the maximum number of packets that can be allocated in the other time slots of the frame. It depends only on the order of arrival of the packets, which is random for all the time slots. Therefore maximum throughput can not be dependent on the frame size (although the latency of the packets does depend on the frame size). ■

Recall that the simulation results presented in the previous section were obtained with a traffic model in which a new packet for portable i ($i = 1, 2, ... M$) arrives in its buffer during a time slot according to the Bernoulli process. We used the same traffic model to obtain the FFA maximum throughput since, with this well behaved type of traffic, we can keep the buffer size reasonably small in order to speed up the computations. We observed that using this type of traffic, the FFA could be obtained using a buffer size not larger than four times the number of portables in the microcell: larger throughputs could not be obtained with a buffer size larger than this.

To force the FFA to achieve its maximum throughput we used a load larger than or equal to the maximum throughput. For example, in order to obtain the maximum throughput when three ports are used in the base station, we used a load of 3 packets per time slot (on average 3 packets per time slot were generated by the Bernoulli process). In this simulation, packets that arrived when the buffer was full were dropped. The maximum throughput was then obtained by averaging over 10^4 time slots, which provided an adequate confidence interval.

Figures 3.10, 3.11 and 3.12 show the FFA maximum throughput up-link results for locations 1, 2 and 3, respectively. The results are plotted as functions of the capture threshold. The solid curves represent the results obtained with power control, and the dotted curves represent the results obtained without power control. Power control provided a greater improvement in the FFA maximum throughput in location 1 than in location 2 or

3. This was expected because location 1, with its concrete block walls, worsens the near/far problem, as discussed in the previous section.

It should be noted that, for certain capture threshold values in Figures 3.11 and 3.12, the maximum throughput is better without power control than with power control. This situation seems counter-intuitive, but in fact it may occur. Let us consider the example of two portables $\mathbf{P}_1$ and $\mathbf{P}_2$ with the following values of portable-sector power gain: $G_{1,B(1)} = -15$ dBm; $G_{1,B(2)} = -30$ dBm; $G_{2,B(2)} = -20$ dBm; and $G_{2,B(1)} = -25$ dBm. Substituting these values into condition (2.2) we obtain:

$$\left\{ \begin{array}{l} G_{1,B(1)} - G_{2,B(1)} = 10 \text{ dB} \\ G_{2,B(2)} - G_{1,B(2)} = 10 \text{ dB} \end{array} \right\} . \tag{3.2}$$

Therefore, these portables are compatible in the up-link case if the capture threshold is 10 dB. Let us now assume that power control is used to equalize the received signals represented by parameters $G_{i,B(i)}$ to -10 dBm. In this case, the new portable-sector power gain values are: $G_{1,B(1)} = -15 + 5 = -10$ dBm; $G_{1,B(2)} = -30 + 5 = -25$ dBm; $G_{2,B(2)} = -20 + 10 = -10$ dBm; and $G_{2,B(1)} = -25 + 10 = -15$ dBm. Substituting these new values into condition (2.2) we obtain:

$$\left\{ \begin{array}{l} G_{1,B(1)} - G_{2,B(1)} = 5 \text{ dB} \\ G_{2,B(2)} - G_{1,B(2)} = 15 \text{ dB} \end{array} \right\} . \tag{3.3}$$

Therefore, with the use of power control, these portables become incompatible in the up-link case for the capture threshold of 10 dB. We conclude that compatibilities may be destroyed by the power control mechanism, and this explains why, for some capture threshold values in Figures 3.11 and 3.12, the maximum throughput is better without power control than with power control.

Figures 3.13, 3.14 and 3.15 show the down-link FFA maximum throughput results for locations 1, 2 and 3, respectively. These results were obtained under the assumption that the base station transmits the same power level to all the portables. Note that they are close matches to the curves obtained in the up-link using power control. This makes sense

because, with power control in the up-link case, the base station receives the same signal level from all the portables. In the down-link case, this corresponds to the base station transmitting the same power level to all the portables. Here again there is a similarity with CDMA systems in that the near/far problem affects only the up-link case.

The point in the graphs where two curves merge can be interpreted as the limiting capture threshold value, above which the larger number of ports of the upper curve is unnecessary since it does not provide any extra capacity gain. For example, it can be observed in Figure 3.10 that the solid curves for four ports and three ports merge at a capture threshold of 7 dB, meaning that the four-port case does not provide any extra capacity gain on top of the gain provided by the three-port case with a capture threshold above 7 dB.

Locations 2 and 3 yielded similar results, leading us to the conclusion that reflections and the shadowing caused by soft material partitions, like those in location 2, do not significantly affect FFA performance. With its hard material partitions, location 1 exhibited the worst FFA performance.

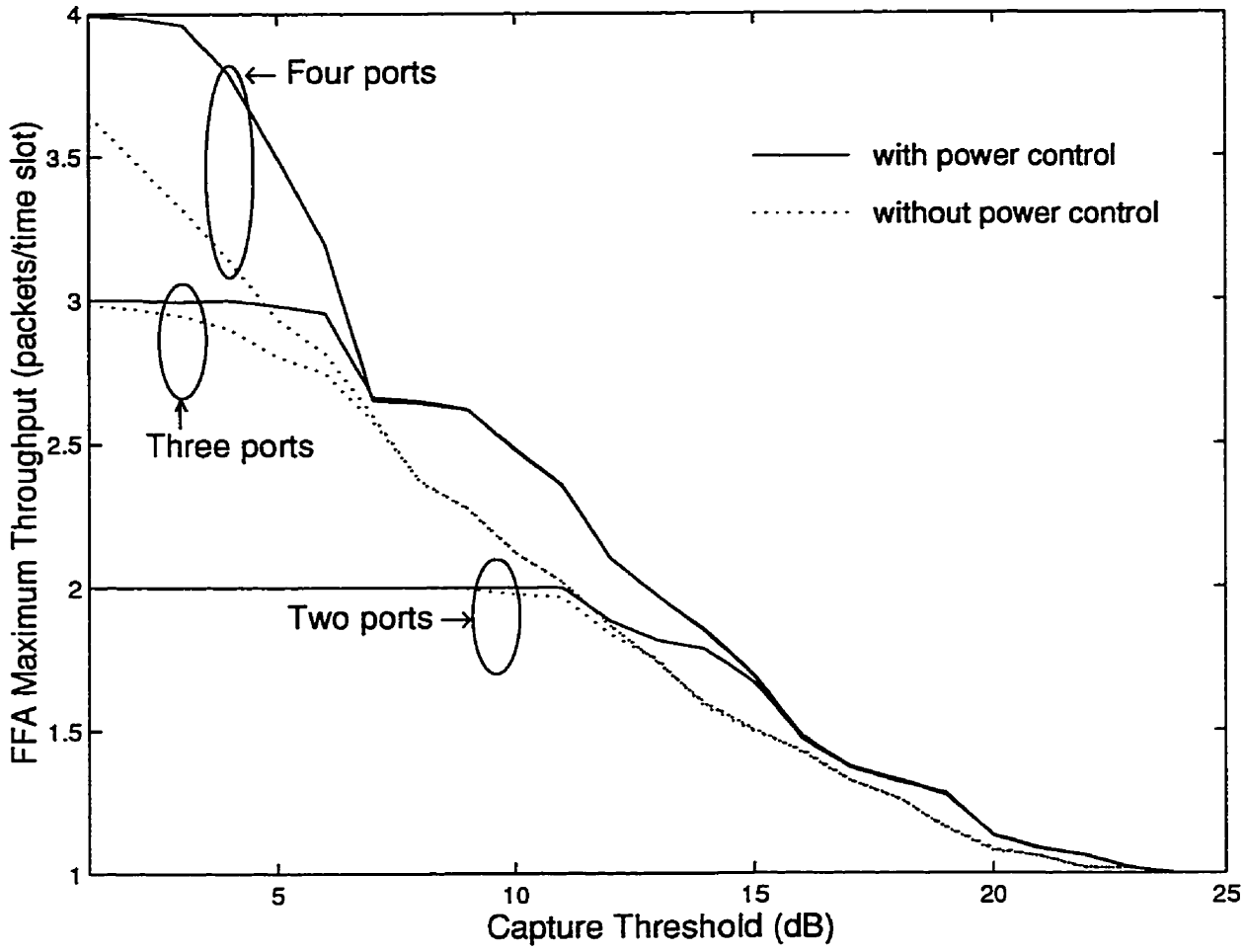

Figure 3.10: FFA up-link maximum throughput in location 1

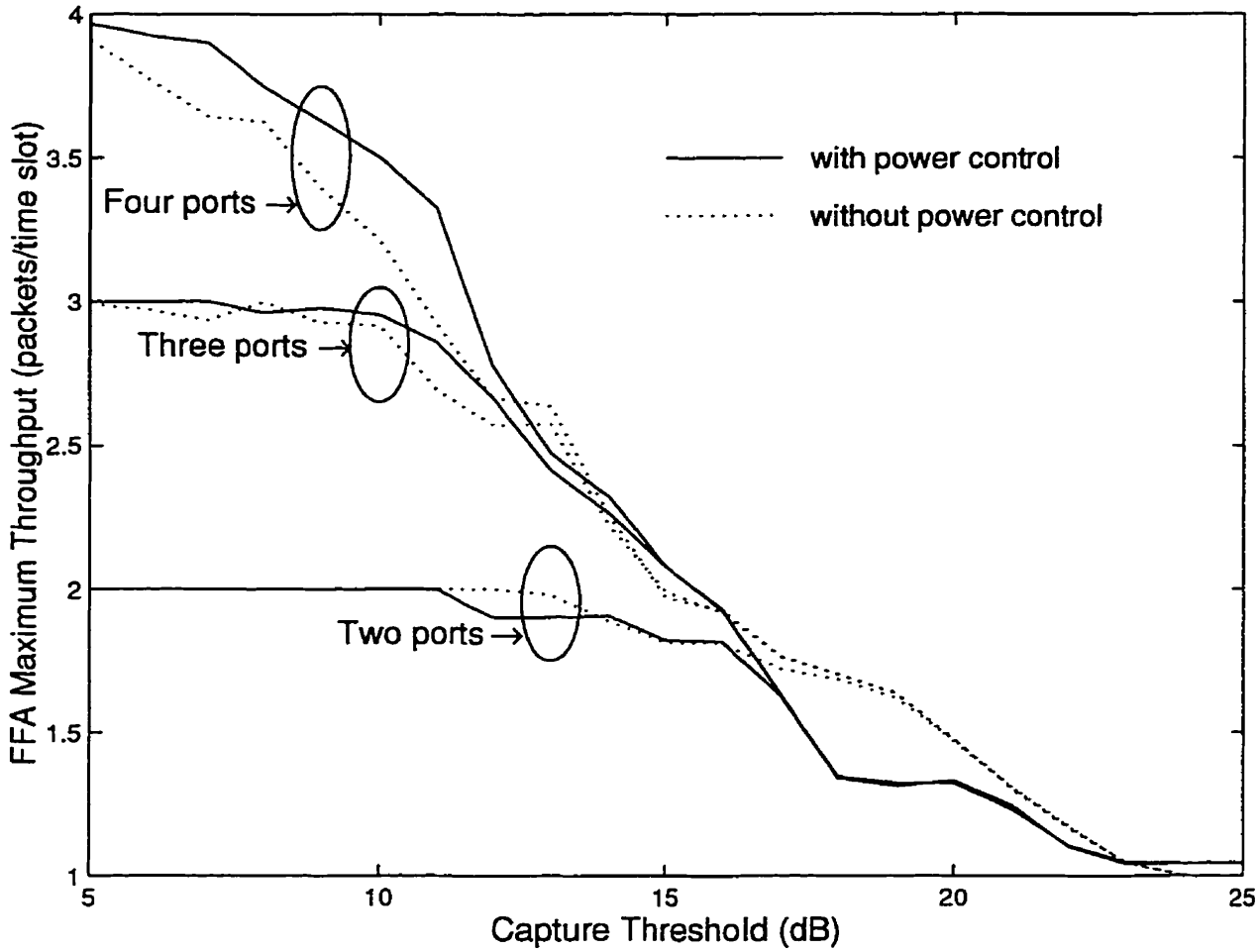

Figure 3.11: FFA up-link maximum throughput in location 2

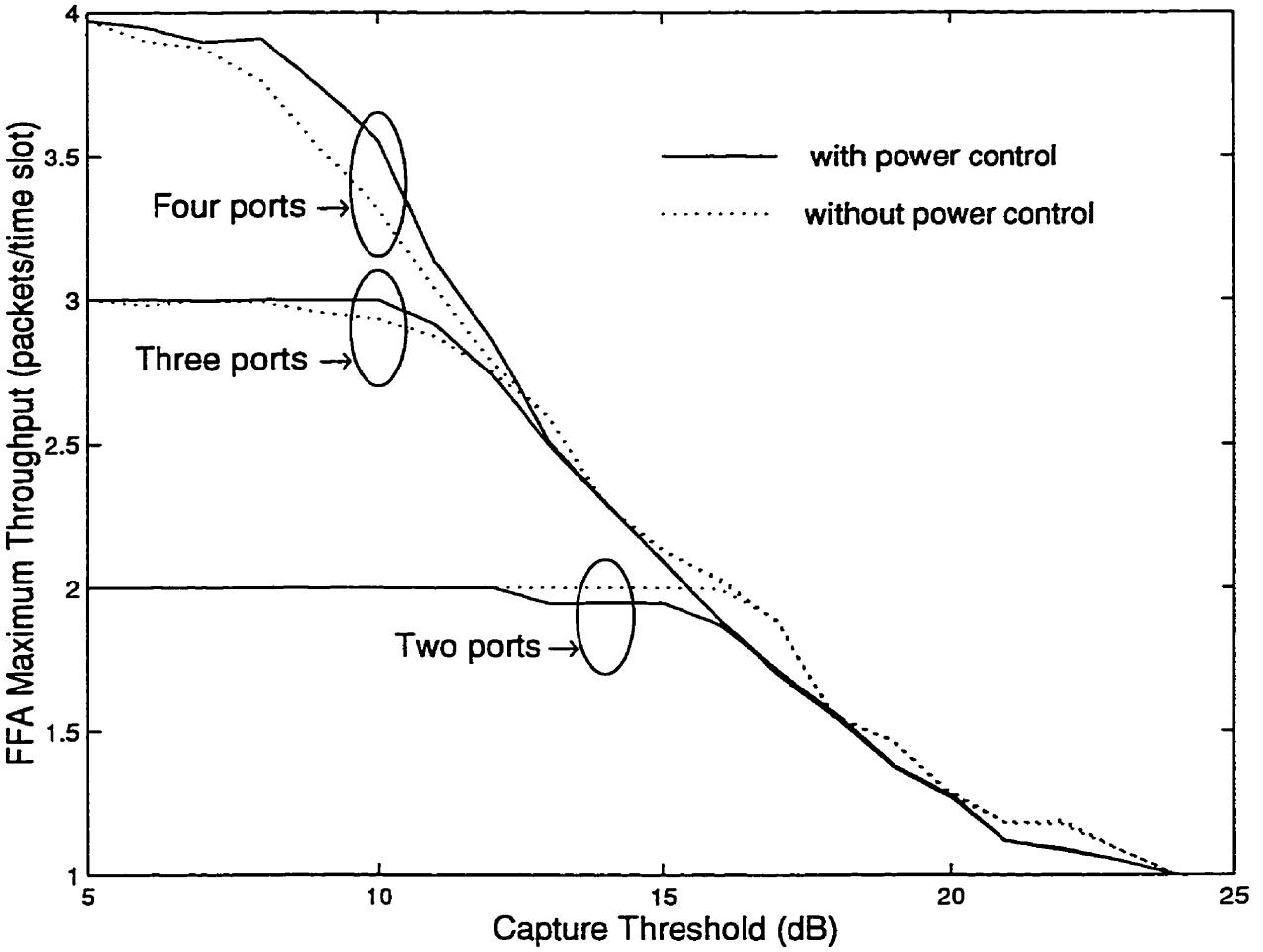

Figure 3.12: FFA up-link maximum throughput in location 3

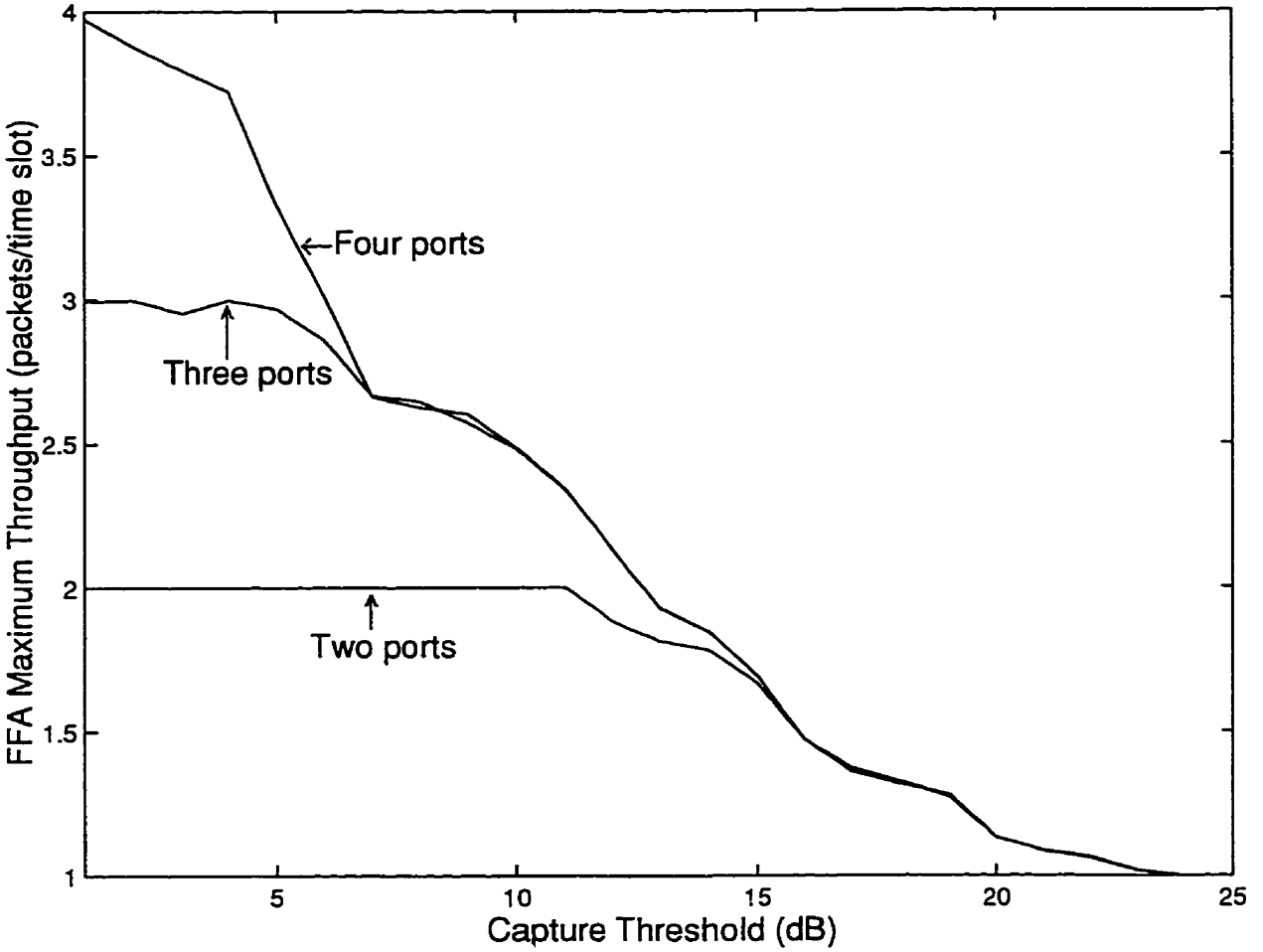

Figure 3.13: FFA down-link maximum throughput in location 1

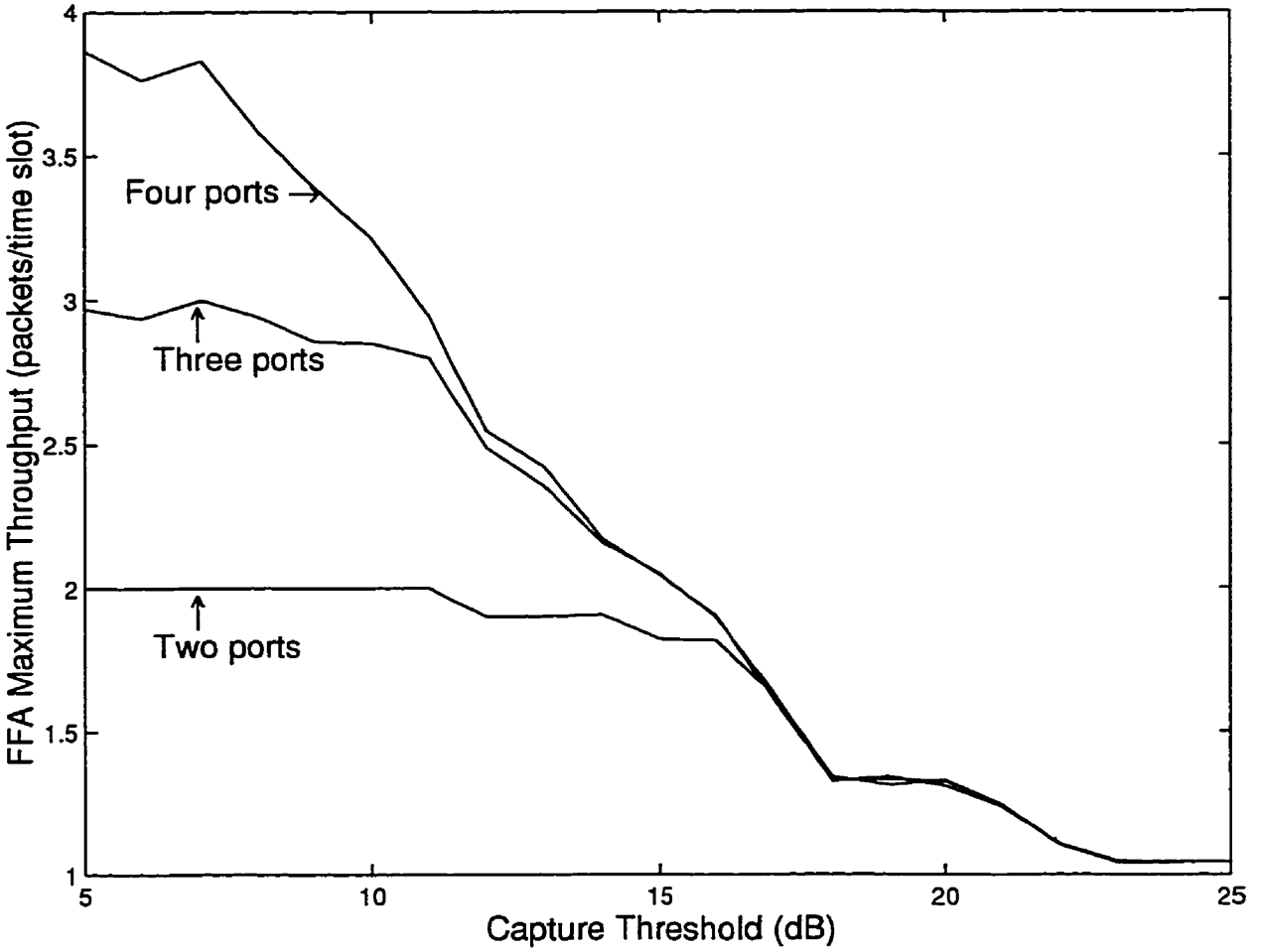

Figure 3.14: FFA down-link maximum throughput in location 2

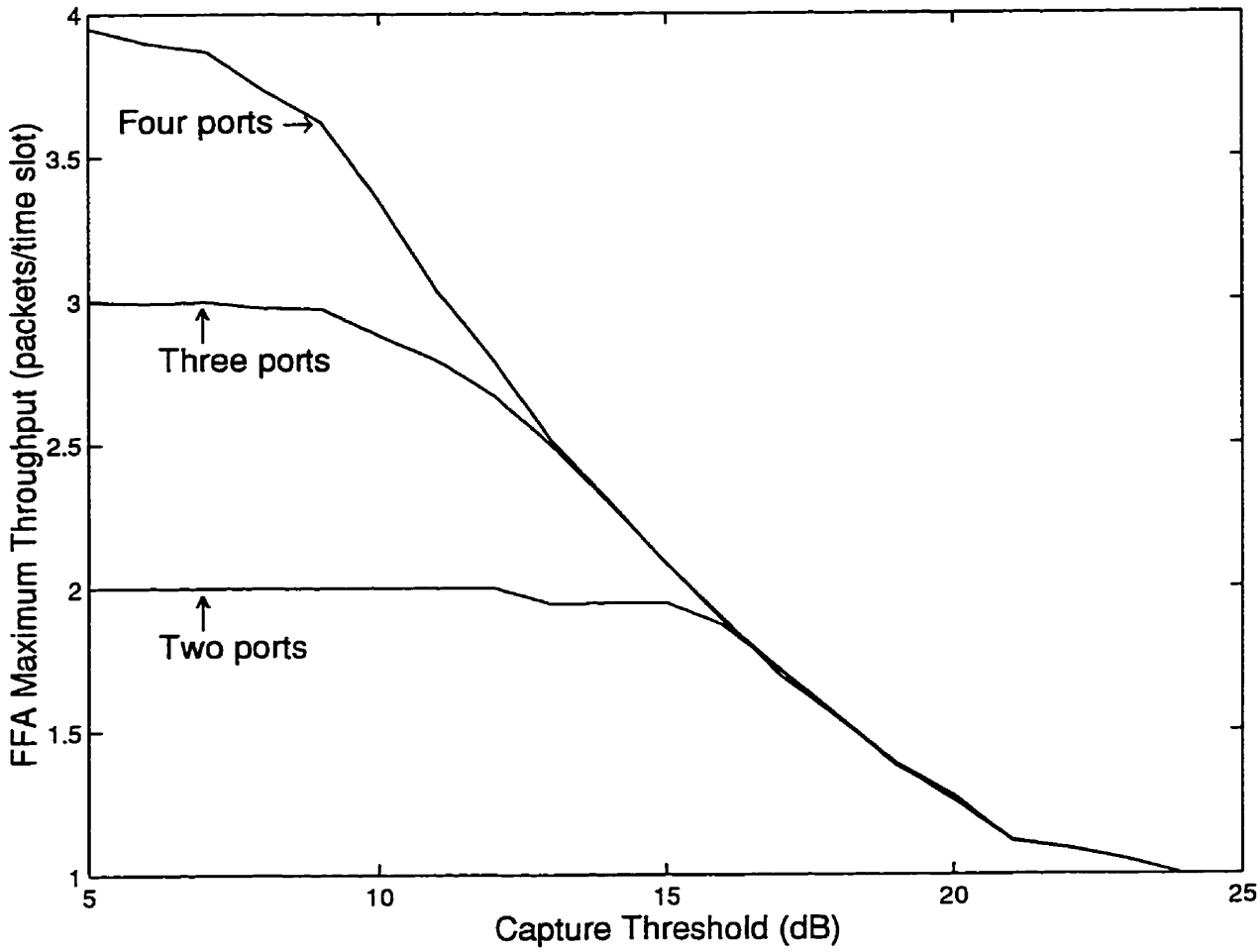

Figure 3.15: FFA down-link maximum throughput in location 3

Chapter 4

FFA Maximum Throughput as a Function of Sectorization Level

4.1 Introduction

So far, we have assumed a sectorization level of 10. We now start to investigate how the use of different sectorization levels affects the average compatibility among the portables and, consequently, how it affects the maximum throughput in the microcells. Intuitively, we can expect that the use of a larger sectorization level, which translates into using antennas with better directivity, can improve the average compatibility among the terminals, since antennas with better directivity can filter out more of the interfering multipaths.

The question was studied using a Monte Carlo simulation of an indoor multipath propagation statistical model. This was preferred over two other options: simulation by means of ray tracing [24] [25] and actual measurements using antennas of different directivities.

The main difficulty related to ray tracing is that the technique requires a detailed description of the indoor layout and a knowledge of reflection and transmission coefficients of walls, doors, windows, etc. We also had the option of measuring indoor locations using antennas of different directivities. However, we considered this option too complicated because each sectorization level would require its own directive antenna, and so the mea-

surements would have to be repeated for each sectorization level investigated. Moreover, these two options have the drawback of being ad hoc, unlike an indoor multipath propagation statistical model that can be applied to any location provided that some parameters in the model are adjusted appropriately.

In the following section, we describe the statistical model used for indoor propagation. The model is proposed by Spencer et al. [13] as an extension of the Saleh-Valenzuela model [15], and it accounts for amplitude, time and angle of ray arrival.

4.2 A Statistical Model for Amplitude, Time and Angle of Arrival in Indoor Multipath Propagation

The statistical model for indoor multipath propagation proposed by Saleh and Valenzuela does not take into consideration the angles of arrival of the multipaths, which are necessary in our investigation. However it has served as the starting point for a statistical model developed by Spencer et al. that incorporates the angle of arrival into multipath propagation. The resulting model is a combination of two statistically independent processes, one governing ray amplitudes and arrival times, and the other governing ray angles of arrival.

Modeling Ray Amplitude and Ray Arrival Time

This part of the model is actually the Saleh-Valenzuela model itself. It assumes that, in the time axis, rays arrive in clusters. The cluster arrival time (T_l, see Figure 4.1), which is defined as the arrival time of the first ray of the cluster, is modeled by a Poisson arrival process with rate Λ. A Poisson arrival process is also used, but with rate λ, to model ray arrival times (τ_{kl}, see Figure 4.1) within a cluster. The distribution of these arrival times is given by

$$p(T_l|T_{l-1}) = \Lambda e^{-\Lambda(T_l - T_{l-1})} \tag{4.1}$$

$$p(\tau_{kl}|\tau_{(k-1)l}) = \lambda e^{-\lambda(\tau_{kl} - \tau_{(k-1)l})}, \tag{4.2}$$

where l represents the l-th cluster and kl represents the k-th ray within the l-th cluster.

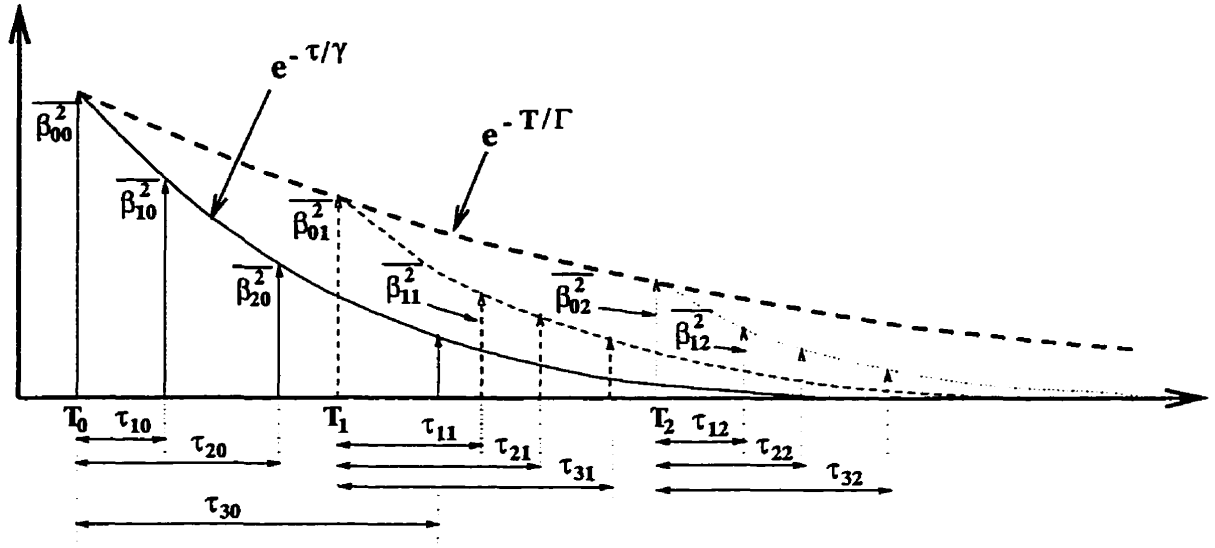

Figure 4.1: A representation of the clustering phenomenon in multipath propagation

Let us assume that the kl-th ray has amplitude β_{kl} and phase ϕ_{kl}. Therefore the channel impulse response is given by

$$h(t) = \sum_{l=0}^{\infty} \sum_{k=0}^{\infty} \beta_{kl} e^{-j\phi_{kl}} \delta(t - T_l - \tau_{kl}). \tag{4.3}$$

In this model, β_{kl} is a Rayleigh distributed random variable whose mean square value is illustrated in Figure 4.1, and is expressed mathematically by a double-exponential decay

$$\overline{\beta_{kl}^2} = \overline{\beta^2(0,0)} e^{-T_l/\Gamma} e^{-\tau_{kl}/\gamma}, \tag{4.4}$$

where $\overline{\beta^2(0,0)}$ is the average power of the first arrival, and Γ and γ are cluster and ray power-decay time constants, respectively. The following expression for $\overline{\beta^2(0,0)}$ is derived by Saleh and Valenzuela [15]:

$$\overline{\beta^2(0,0)} \approx \frac{G(1m) r^{-\alpha}}{\gamma \lambda}, \tag{4.5}$$

where r is the separation distance of the transmitter and receiver, $G(1m)$ is the channel gain at a distance of 1 meter ($r = 1$), and α is the channel loss parameter which depends on the characteristics of the indoor environment. A typical value of α for office buildings

is 3 [15], but values as high as 6 have been reported for office buildings with metalized partitions [27].

In [13] and [15], T_0, the arrival time of the first cluster, is defined in different ways. We will assume the definition given in [13], which is

$$T_0 = \frac{r}{c}, \tag{4.6}$$

where c is the speed of light.

Modeling the Ray Angle of Arrival

In their measurements, Spencer et al. could not observe any correlation between the angle and the time of ray arrival. Based on this fact, they propose a statistical model for ray angle of arrival that is independent of the ray arrival time. The following expression represents the proposed angular impulse response of the multipath channel:

$$h(\theta) = \sum_{l=0}^{\infty} \sum_{k=0}^{\infty} \beta_{kl} \delta(\theta - \Theta_l - \omega_{kl}), \tag{4.7}$$

where β_{kl} has the same meaning as in Equation 4.3; Θ_l is the mean angle of the l-th cluster, that is, the mean angle of the rays arriving within the l-th cluster; and ω_{kl} is the angle deviation from Θ_l making the kl-th ray arrive at an angle of $\Theta_l + \omega_{kl}$.

It is proposed in [13] that Θ_l be uniformly distributed throughout the interval $[0, 2\pi)$ and that the ray angle deviation, ω_{kl}, be modeled as a zero mean Laplacian distribution with standard deviation σ:

$$p(\omega) = \frac{1}{\sqrt{2}\sigma} e^{-|\sqrt{2}\omega/\sigma|}. \tag{4.8}$$

Estimated Parameters

The resulting statistical model, which accounts for amplitude, time, and angle of arrival, is defined by five parameters: Λ, λ, Γ, γ, and σ. Table 4.1 shows Spencer et al.'s estimations for these parameters, which were based on measurements taken in two different buildings

Parameter	Building 1	Building 2
Γ	33.6 ns	78.0 ns
γ	28.6 ns	82.2 ns
$1/\Lambda$	16.8 ns	17.3 ns
$1/\lambda$	5.1 ns	6.6 ns
σ	25.5°	21.5°

Table 4.1: Parameters estimated by Spencer et al.

and reported in [14]. The frequency used in these measurements was 7 GHz, which is relatively close to the 5.8 GHz frequency that we used in our measurements.

In order to understand why the parameter values are building-dependent, we need a physical interpretation of the model. Spencer et al. observed that the strongest cluster was almost always associated with a direct line of sight path, even when this line was blocked by walls. Weaker clusters were apparently caused by back wall reflections and doorway openings. Therefore the formation of clusters is related to building superstructures. The rays within a cluster are related to smaller objects, such as furniture, that are in the vicinity of the transmitter and the receiver.

4.3 Using the Statistical Model to Simulate Average Compatibility

This section shows how the statistical model described in the previous section can be used to simulate average compatibility among portables. We first define the dimensions of the indoor location. We will assume an area of 25×30 m^2, which is the area of our indoor location 1 (see Figure 2.10). In order to compose a simulation scenario, we place the base station at the center of this area, and we place M portables (we will be considering $M = 50$) at random positions uniformly distributed within the area. This is illustrated in Figure 4.2.

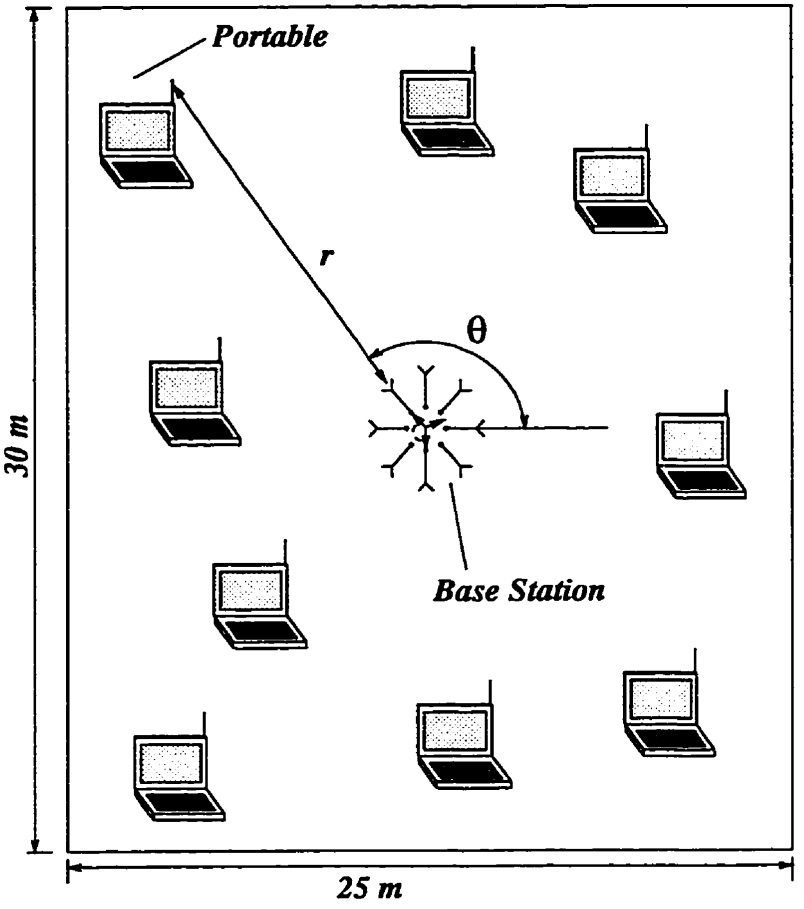

Figure 4.2: A generic indoor location

Next, the steps in the following list are repeated in order to generate a total of 4 clusters and 15 rays per cluster for each portable. These numbers were chosen based on the observation that using more than 4 clusters and more than 15 rays per clusters did not alter the simulation results significantly.

- Portable-Base distance r is used in (4.6) to compute the arrival time of the first cluster T_0.
- The probability distributions of (4.1) and (4.2) are used to draw the cluster arrival times (T_l) and the ray arrival times (τ_{kl}), respectively.

- Portable-Base distance r is used in (4.5) to compute the average power of the first arrival ($\overline{\beta_{00}^2}$).

- Cluster arrival time, ray arrival times and the average power of the first arrival are used in (4.4) to compute the mean square value of the ray amplitudes ($\overline{\beta_{kl}^2}$).

- A Rayleigh distribution with mean square values of $\overline{\beta_{kl}^2}$ is used to draw the kl-th ray amplitude (β_{kl}).

- A random phase ϕ_{kl} is drawn for each ray using a uniform distribution in the interval [0, 2π). Therefore the channel impulse response for the kl-th path is given by $\beta_{kl}e^{-j\phi_{kl}}\delta(t - T_l - \tau_{kl})$.

- The angle of the line of sight path Θ (see Figure 4.2) is used as angle of arrival for the first cluster Θ_0. This is based on the observation made by Spencer et al. that the strongest cluster was almost always associated with a direct line of sight path, even when this line was blocked by walls.

- A random angle of arrival Θ_l is drawn for each remaining cluster using a uniform distribution in the interval [0, 2π). Note that this does not incorporate possible angular correlations among clusters of neighboring portables. Figure 4.3 illustrates why cluster arrival angles of neighboring portables are likely to be correlated. However for now, we disregard these correlations.

- The probability distribution of (4.8) is used to draw the angle of arrival deviation ω_{kl} for each path. Therefore the ray angle of arrival of the kl-th ray is $\Theta_l + \omega_{kl}$.

Computing Average Power

Once we have obtained the angle of arrival and channel impulse response for each path, we can proceed to compute the average power received by the base station in each of its antenna sectors when a given portable transmits. We have to decide on the number of sectors to

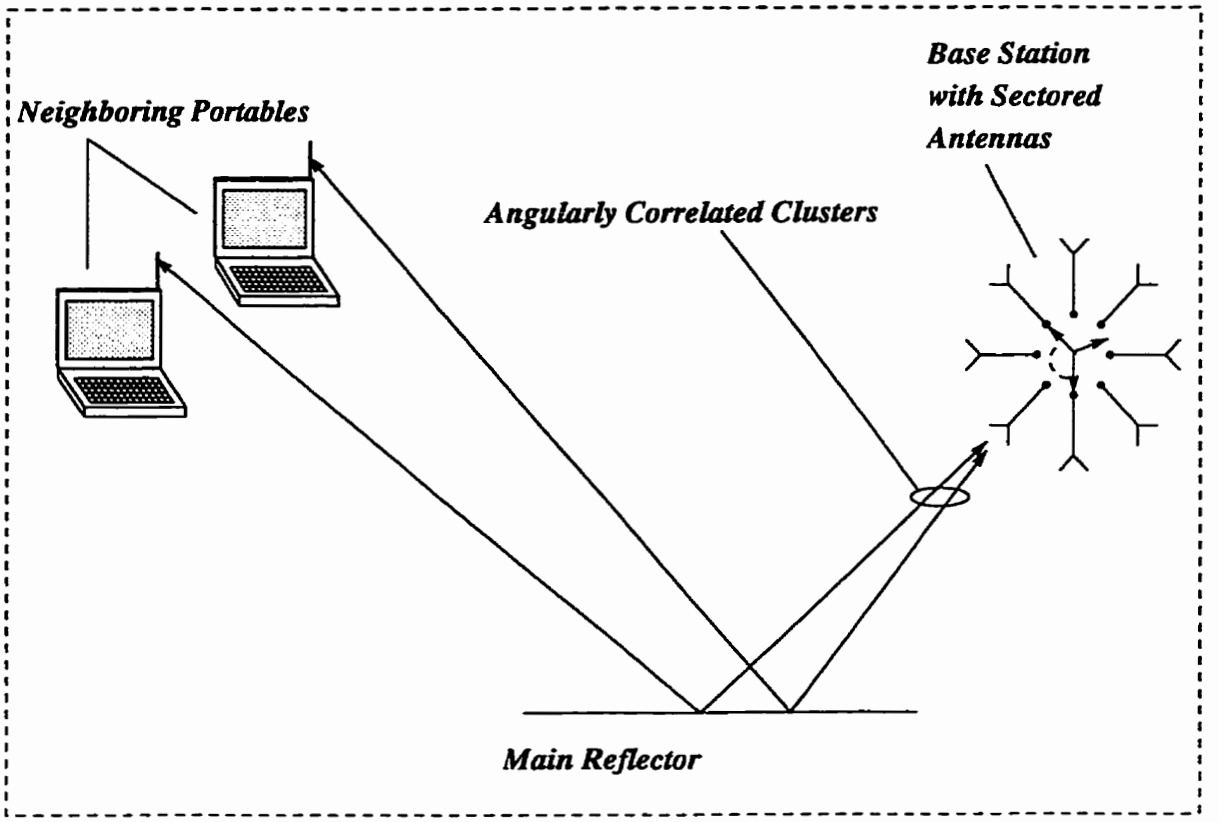

Figure 4.3: Illustration of angular correlation between clusters of neighboring portables.

simulate. Let us start with a sectorization level of 10 and assume that each sector employs a horn antenna like the one which was used for the measurements reported in Chapter 2. This antenna has approximately 36° of 3 dB beamwidth and its radiation pattern is shown in Figure 2.7, and the superimposed field strength patterns of the 10 sectors are shown in Figure 2.8.

In order to compute the average power received in each sector, we need the channel impulse response between the i-th sector and a given portable. This can be expressed by

$$h_i(t) = \sum_{l=0}^{\infty} \sum_{k=0}^{\infty} \beta_{kl} e^{-j\phi_{kl}} \delta(t - T_l - \tau_{kl}) g_i(\Theta_l + \omega_{kl}), \tag{4.9}$$

where $g_i(\theta)$ is the i-th antenna sector gain at angle θ.

Now we are ready to compute the average power received in each sector when a given portable transmits. We are interested in the average power received in a bandwidth of

20 MHz centered at 5.8 GHz. This can be expressed as

$$G_i = \frac{1}{20 \times 10^6} \int_{-10\times10^6}^{10\times10^6} |H_i(f - 5.8 \times 10^9)|^2 df, \tag{4.10}$$

where $H_i(f)$ is the channel frequency response between the portable and the i-th sector which is the Fourier transform of $h_i(t)$:

$$H_i(f) = \int_{-\infty}^{\infty} h_i(t) e^{-j2\pi ft} dt. \tag{4.11}$$

Substituting (4.9) into (4.11) we obtain

$$H_i(f) = \sum_{l=0}^{\infty} \sum_{k=0}^{\infty} g_i(\Theta_l + \omega_{kl}) \beta_{kl} e^{-j\phi_{kl}} e^{-j2\pi f(T_l + \tau_{kl})}. \tag{4.12}$$

Review of the Compatibility Condition

We now review the compatibility conditions defined in Chapter 2.

We use (4.10) to compute the average power received in the i-th antenna sector when portable p transmits. Let us rename it $G_{p,i}$; it can also be seen as the average power received by portable p when the base station transmits through its i-th antenna sector. This is true because up-link and down-link transmissions occur in the same frequency band; therefore there is up-link/down-link channel reciprocity. Consider antenna sector $B(p)$ which provides the best average power to portable p (defined in Chapter 2). Therefore the best average power for portable p is $G_{p,B(p)}$. In order to verify compatibility among portables, we use these values in the conditions defined in (2.3) and (2.4) for the down-link case and for the up-link case, respectively.

4.4 Simulations

The steps described in the previous section were followed to simulate average compatibilities among portables uniformly distributed in a 25×30 m^2 indoor location. The results were averaged over ten different scenarios, so that, for a given set of parameters, the simulations were run ten times, and a different draw of portables positions was used for each

run. The results were then presented as the average of these ten outputs. We chose to simulate only down-link average compatibilities since, as we saw in Chapter 2, up-link average compatibilities are close matches to down-link average compatibilities when power control is used.

The first simulation used the parameter values in Table 4.1 for building 1 which are: $\Gamma = 33.6$ ns, $\gamma = 28.6$ ns, $1/\Lambda = 16.8$ ns, $1/\lambda = 5.1$ ns, and $\sigma = 25.5°$. The channel loss parameter used was $\alpha = 3$. However, changing the value of α did not affect the simulation results, as expected for the down-link case. Figure 4.4 shows the simulation results compared with the average compatibilities measured in location 1. We can see that the measured and the simulated results did not match very well. However the matching can be improved by changing the simulation parameters as follows.

In Table 4.1, the main differences between the estimates of the two buildings are the values of Γ and γ. The lower values of Γ and γ in building 1 arise because there is greater attenuation with internal walls of cinder blocks than in building 2 whose internal walls are gypsum board [14]. Therefore, we can expect location 1 (see Fig. 2.10), whose internal walls are concrete blocks, to attenuate more than building 1. For example, we simulated average compatibilities with $\Gamma = 10$ ns and $\gamma = 10$ ns, and compared them with the average compatibilities of location 1. The results are shown in Figure 4.5. We can see that matching was improved at low values of the capture threshold, but the mismatch worsened at higher capture threshold values. This made us think that, while taking measurements in location 1, the horn antenna radiation pattern (see Fig. 2.7) may have been distorted due to the proximity of the spectrum analyser and computer monitor (see Fig. 2.6), which were mounted on a cart at a distance of less than one meter from the horn antenna. Moreover, metal structures on the ceiling (light fixtures) which were close to the antenna may have contributed to pattern distortion. The most likely form of distortion is enhancement of the back and side lobes, which may have been caused by rays that were reflected into the main lobe by the measuring system (cart, spectrum analyzer and personal computer) and/or by the light fixtures. In order to investigate this possibility, we ran a simulation using the

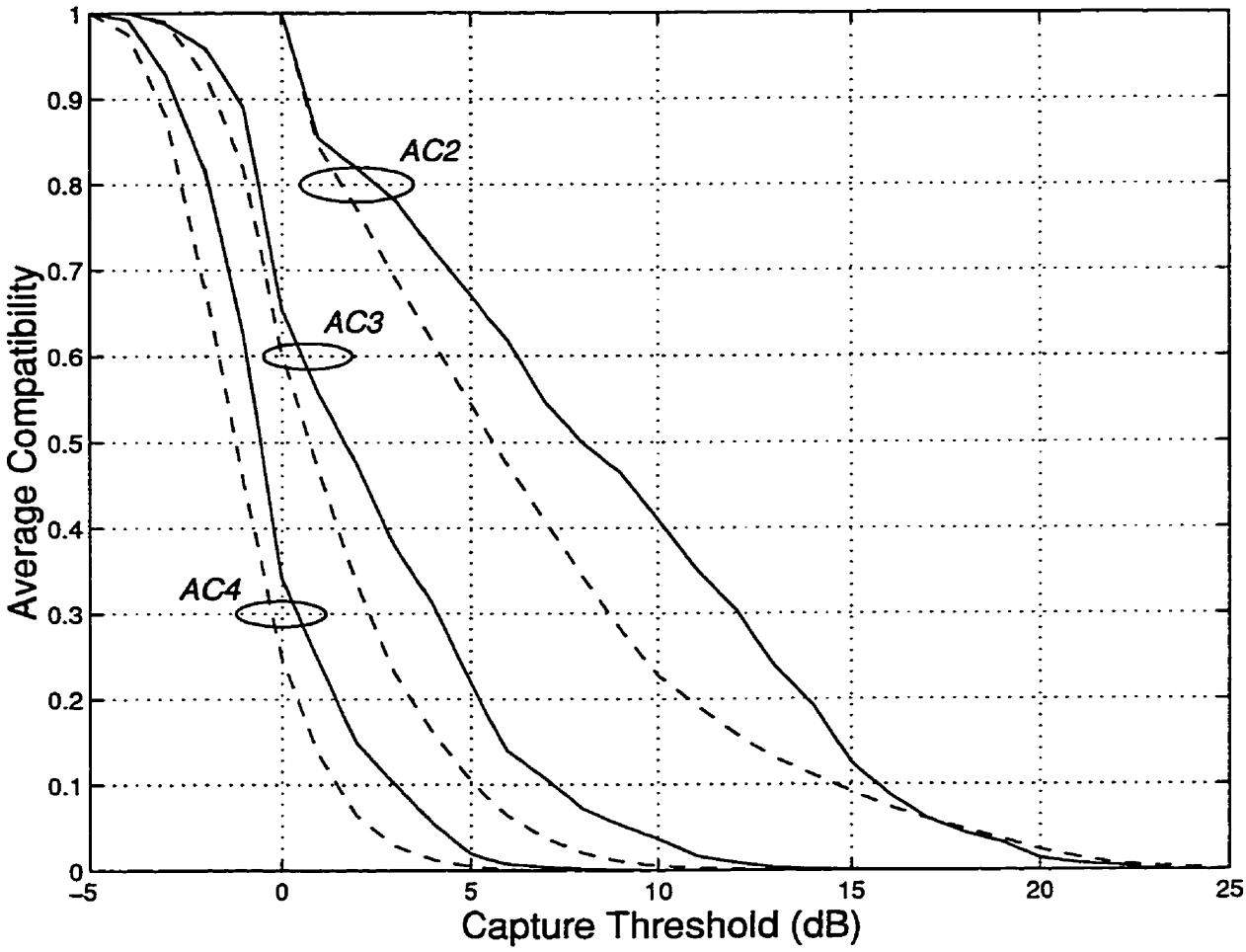

Figure 4.4: Average compatibilities simulated with parameters of building 1 (dashed lines) compared with average compatibilities measured in location 1 (solid lines)

antenna radiation pattern of the horn antenna distorted by back/side lobes in each sector. We added three -15 dB back/side lobes to the original antenna pattern. The resulting empirical antenna pattern is shown in Figure 4.6.

Figure 4.7 shows the average compatibilities simulated with this distorted antenna pattern compared with the average compatibilities measured in location 1. As the curves matched very well, we concluded that antenna back/side lobes are responsible for the loss in average compatibility at the high capture threshold values observed in Figure 4.5. Therefore, antennas with small side/back lobes in their radiation patterns should be used to pre-

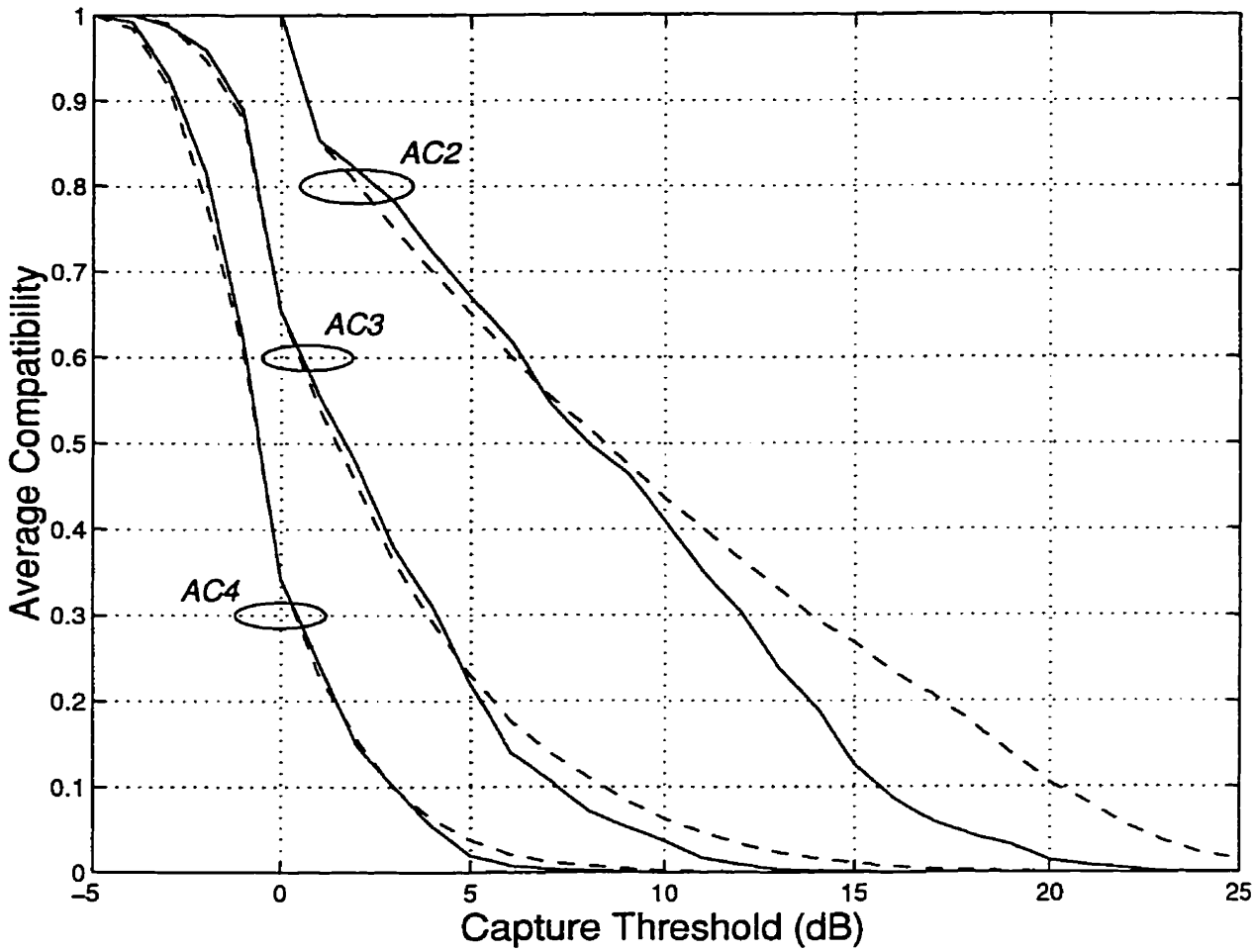

Figure 4.5: Average compatibilities simulated with $\Gamma = 10$ ns and $\gamma = 10$ ns (dashed lines) compared with average compatibilities measured in location 1 (solid lines)

vent this from happening. Also, metal structures, such as light fixtures should be kept as far as possible from the antennas to avoid distorting their radiation patterns. However this is important only if the system is to be operated at high values of the capture threshold.

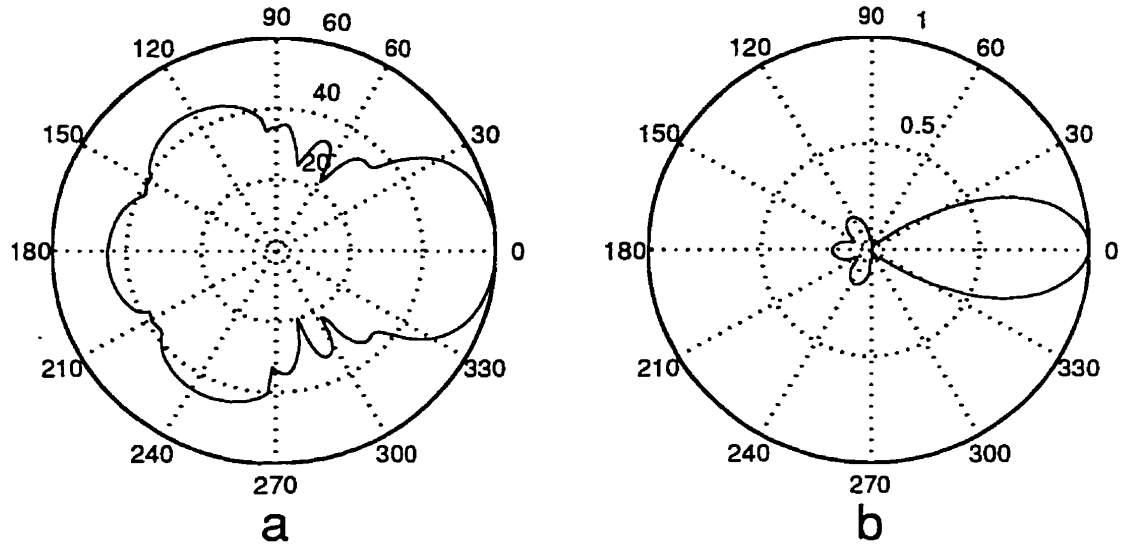

Figure 4.6: (a) Polar coordinate plots of distorted power radiation pattern on logarithmic scale; and (b) distorted field strength pattern on linear scale of the horn antenna used in the experiment. Note: the plotted values were normalized by making the maximum value equal to 60 dB in the logarithmic plot, and by making the maximum value equal to 1.0 in the linear plot.

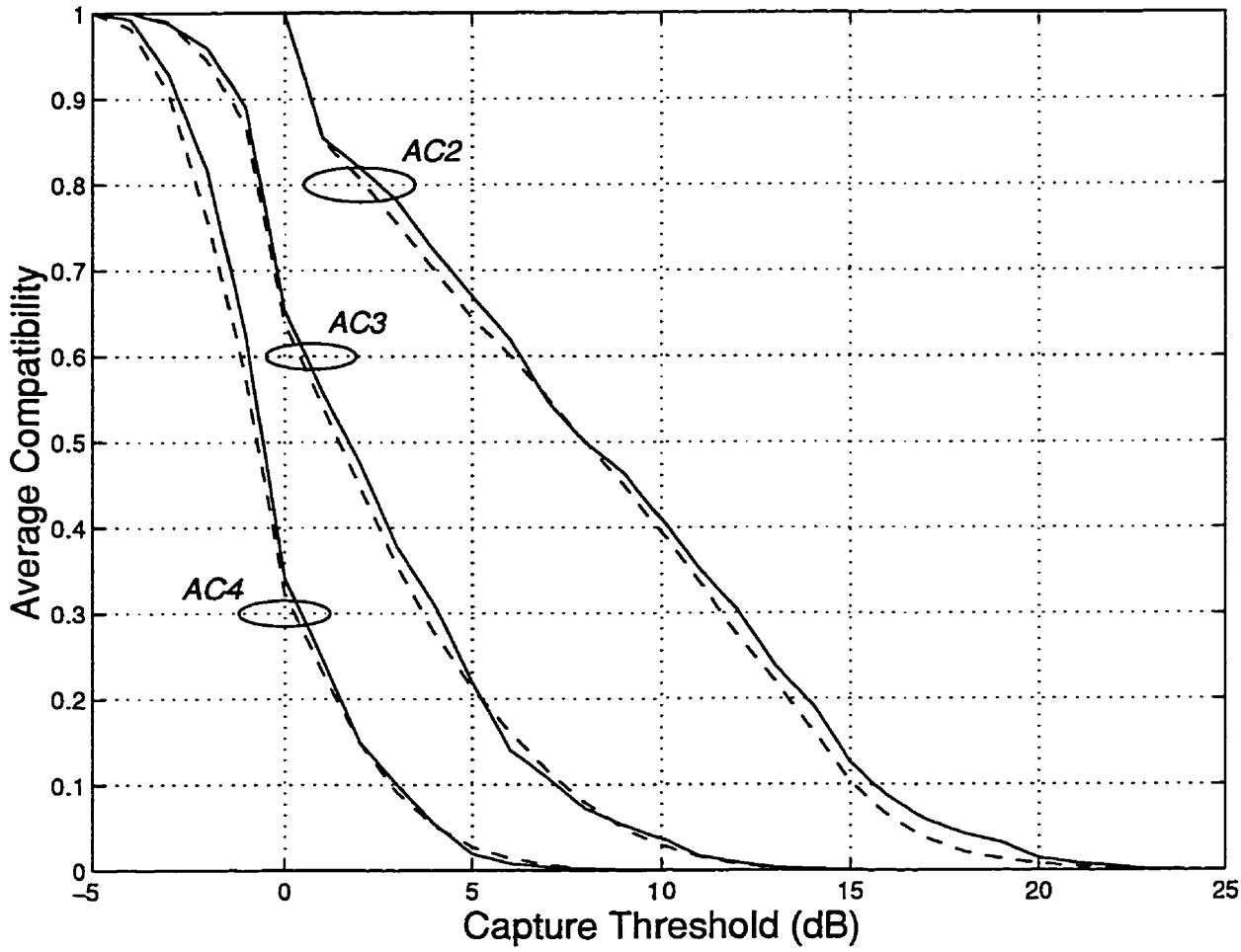

Figure 4.7: Average compatibilities simulated with distorted antenna pattern (dashed lines) compared with average compatibilities measured in location 1 (solid lines)

A Model for Generating Antenna Patterns

So far our simulations have been based on the antenna pattern of the horn antenna used for the indoor measurements reported in Chapter 2. For the following simulations, we will generate antenna patterns using a model where the antenna beamwidth is a variable. With this model, the i-th antenna sector normalized field strength radiation pattern can be generated as

$$g_i(\theta) = \begin{cases} \dfrac{\sin\{\frac{2.78[\theta-(i-1)\Phi]}{\Phi}\}}{\frac{2.78[\theta-(i-1)\Phi]}{\Phi}} & \text{for antenna main lobe} \\ a_0 & \text{otherwise,} \end{cases} \tag{4.13}$$

where a_0 is a uniform side lobe which we assume to be 30 dB below the main beam gain, and Φ is the 3 dB beamwidth of the antenna. The formula used in (4.13) to obtain the main lobe of the antenna resulted from an approximation to the formula for unidirectional radiation from uniform aperture distribution (see [29]-p.517).

For example, Figure 4.8 shows the pattern for antenna sector 1 ($i = 1$) with $\Phi = 36°$ superimposed on the pattern of the horn antenna which we have used in the measurements.

With this antenna pattern model we can simulate average compatibilities with a generic sectored antenna system with N_s sectors using N_s antennas with $\Phi = 360°/N_s$. For example, Figure 4.9 shows sectored antenna systems with 3, 5, 10 and 20 antennas.

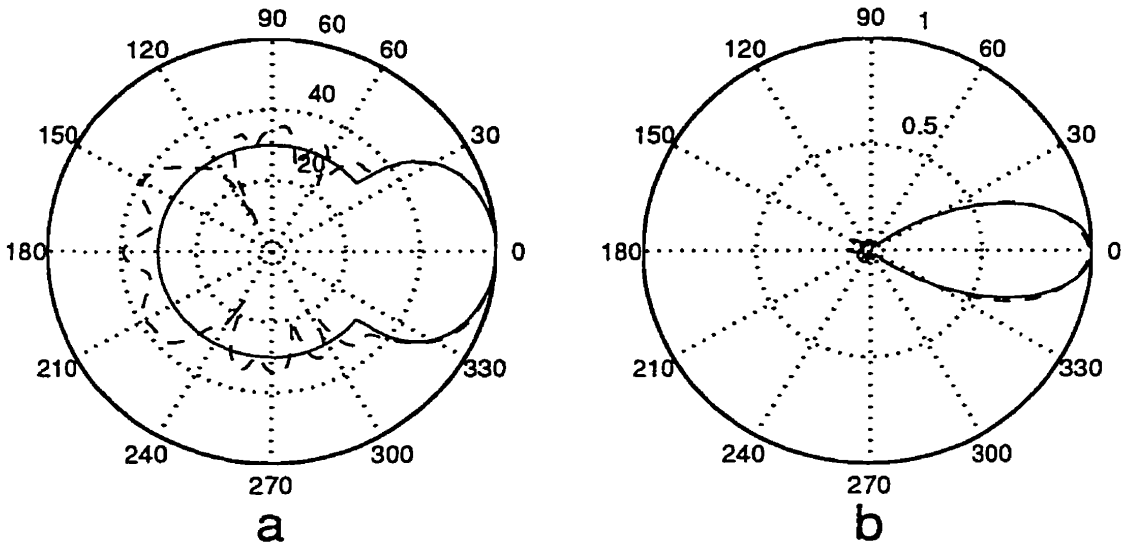

Figure 4.8: Radiation patterns on logarithmic scale (a) and on linear scale (b) of 36° beamwidth antenna (solid) and horn antenna (dashed)

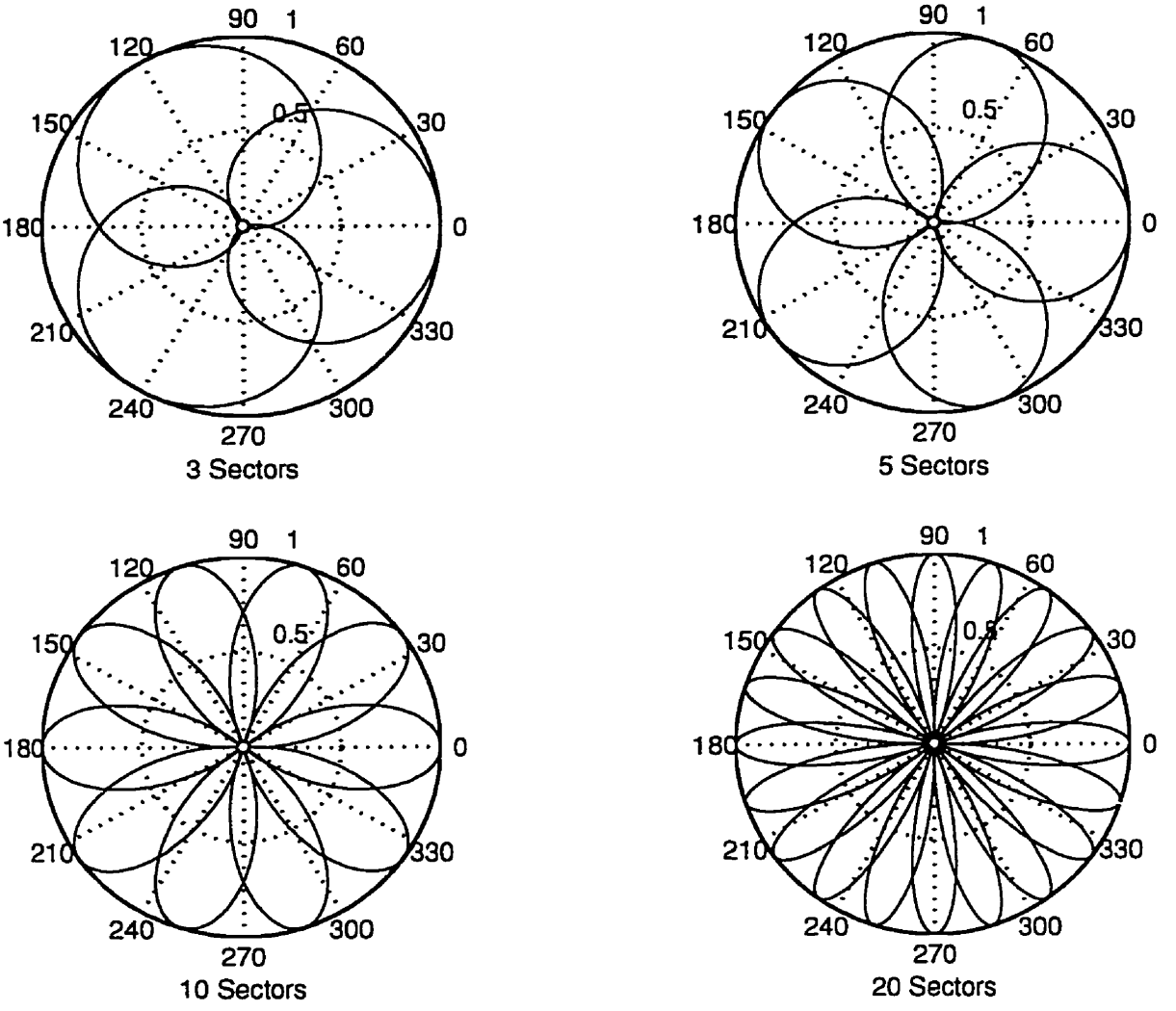

Figure 4.9: Sectored antenna systems with 3, 5, 10 and 20 antennas

Angular Correlations Between Clusters of Neighboring Portables

In the previous simulation results, we did not consider any angular correlation among clusters of portables that were close together in the indoor scenario. However if a portable produces a cluster with angle Θ, it is likely that a neighboring portable will produce a cluster with an angle close to Θ. This is illustrated in Figure 4.3. In order to investigate the effects on the average compatibilities of these correlations, we ran simulations where the simulation scenario was constructed by allocating portables one by one in the area that is illustrated by Figure 4.2, and the cluster angles of arrival for each portable are generated according to the following steps:

- Steps for the first portable:
  - The portable random position within the indoor scenario is generated by a uniform distribution.
  - The angle of the line of sight path Θ (see Figure 4.2) is used as angle of arrival for the first cluster Θ_0.
  - A random angle of arrival Θ_l is drawn for each remaining cluster using uniform distribution in the interval $[0, 2\pi)$.
- Steps for the remaining portables:
  - The portable random position within the indoor scenario is generated by a uniform distribution.
  - The angle of the line of sight path Θ is used as angle of arrival for the first cluster Θ_0.
  - The distance d from the closest portable already allocated in the scenario is obtained.

- The remaining cluster angles are generated according to the following steps:
  * For each remaining cluster generate an angle shift $\Delta\Theta_l$ using a zero mean Laplacian distribution

$$p(\theta) = \frac{1}{\sqrt{2}\sigma} e^{-|\sqrt{2}\theta/\sigma|}, \tag{4.14}$$

    here σ, the standard deviation, is a function of the distance d from the closest portable, that is,

$$\sigma = \rho d^{\nu}, \tag{4.15}$$

    where ρ and ν have their meaning explained below.
  * The angle of arrival of the l-th cluster is given by $\Theta_l = \Theta'_l + \Delta\Theta_l$, where Θ'_l is the angle of arrival of the l-th cluster of the closest portable.

With the constants ρ and ν we can temper the degree of correlation that we want to have among the clusters of neighboring portables as a function of the distance between the portables. For example, if we make $\rho = 5$ and $\nu = 2$, and the closest portable is at a distance of $d = 1$ meter, then the standard deviation σ of Equation (4.15) is 5°, meaning that there is a strong correlation between angles Θ_l and Θ'_l. If the closest portable is at a distance of $d = 5$ meters then the standard deviation is 125°, meaning that angles Θ_l and Θ'_l are only slightly correlated. If the closest portable is at a distance of $d = 10$ meters, then the standard deviation is 500°, meaning that angles Θ_l and Θ'_l are totally uncorrelated. Figure 4.10 shows, for $\rho = 5$ and $\nu = 2$, how the Laplacian distribution of (4.14) gradually approaches a uniform distribution (-180° to 180°) as the distance to the closest portable increases.

We simulated average compatibilities accounting for the correlation among clusters of neighboring portables using $\rho = 5$ and $\nu = 2$. Figure 4.11 shows the simulated average compatibilities when the correlations among clusters of neighboring portables are accounted for and when they are disregarded. Ten sectors were used in these simulations. As we can see, there is a slight decrease in the average compatibilities when the correlations are considered. The decrease was expected and can be explained by the line of reasoning illustrated

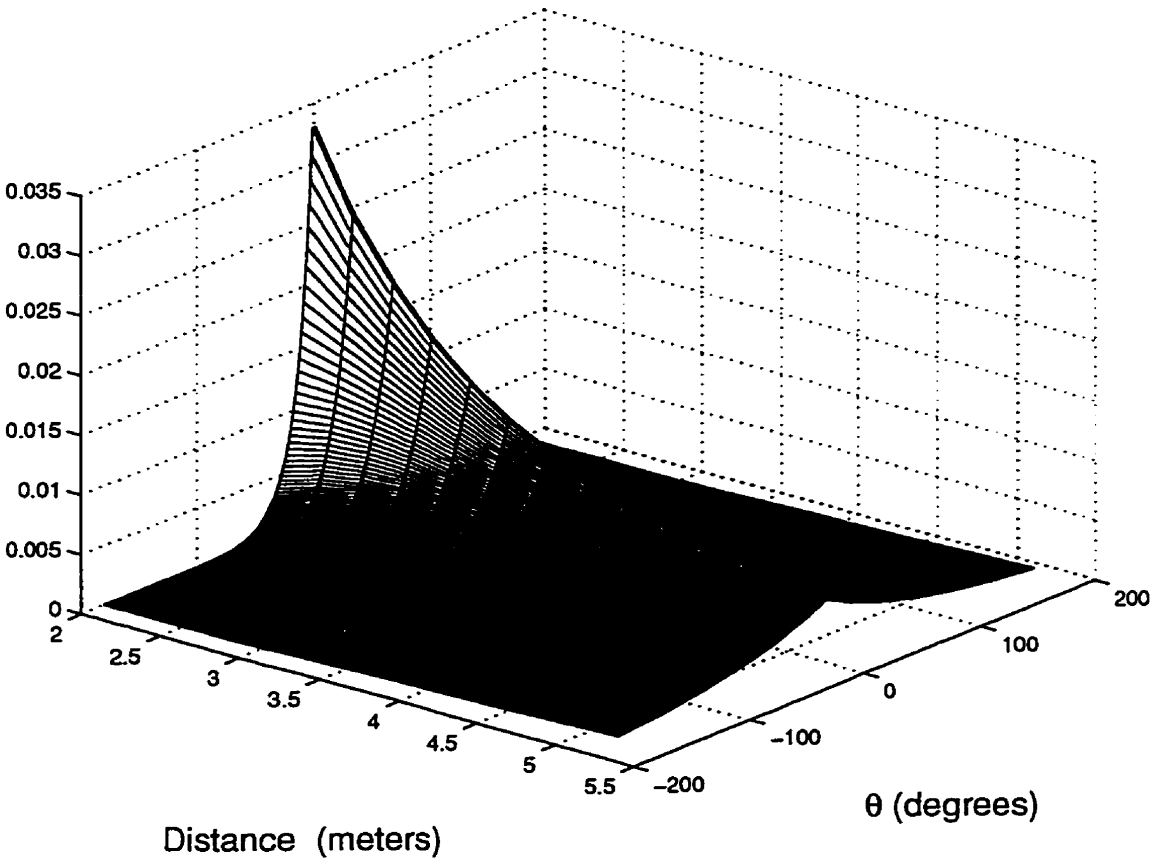

Figure 4.10: Laplacian distribution gradually approaching a uniform distribution as the distance to the closest portable increases

by Figure 4.12. Let us consider two portables, $\mathbf{P}_1$ and $\mathbf{P}_2$, that are not compatible, and let us introduce a third portable, $\mathbf{P}_3$, close to $\mathbf{P}_2$. If correlations among clusters of neighboring portables are considered in the simulations, then it is likely that portables $\mathbf{P}_3$ and $\mathbf{P}_1$ are not going to be compatible either. On the other hand, if the correlations are disregarded, then there is a better chance that portables $\mathbf{P}_3$ and $\mathbf{P}_1$ are going to be compatible.

Obviously, parameters ρ and ν will depend on the building superstructure. We should expect, for example, that a building with many small rooms will provide a smaller degree of correlation since even neighboring portables will probably be separated by walls. On contrary, if the indoor scenario is a single large room, there will be strong correlations between clusters of neighboring portables.

We also investigated the effect of correlations among neighboring portables for other levels of sectorization. We observed that with $\rho = 5$ and $\nu = 2$, there was only a slight decrease in the average compatibilities for the different sectorization levels. Therefore, in the following simulation results, we disregard the correlation between neighbouring portables.

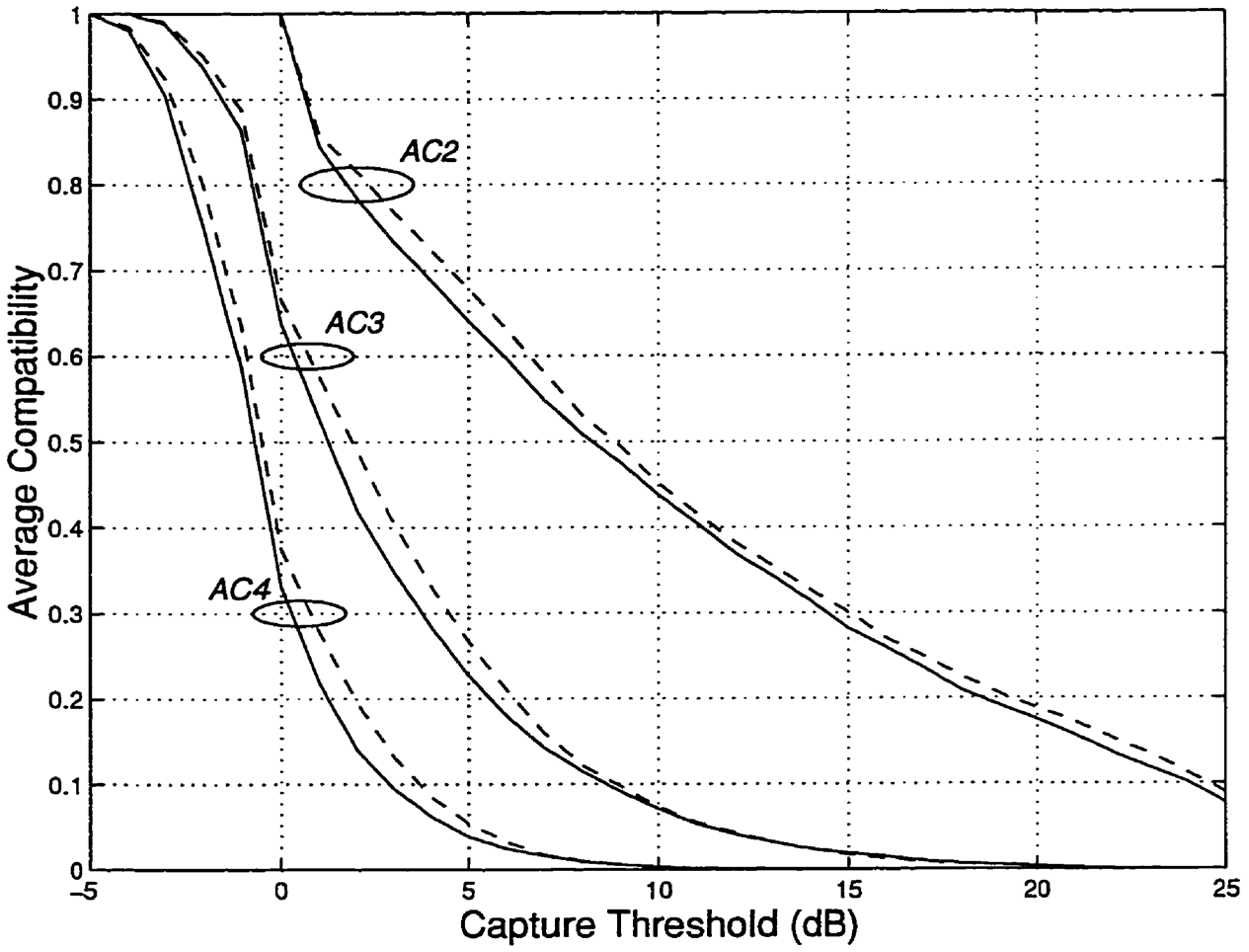

Figure 4.11: Average compatibilities when the correlations among clusters of neighboring portables are accounted for (solid) and when the correlations are not accounted for (dashed)

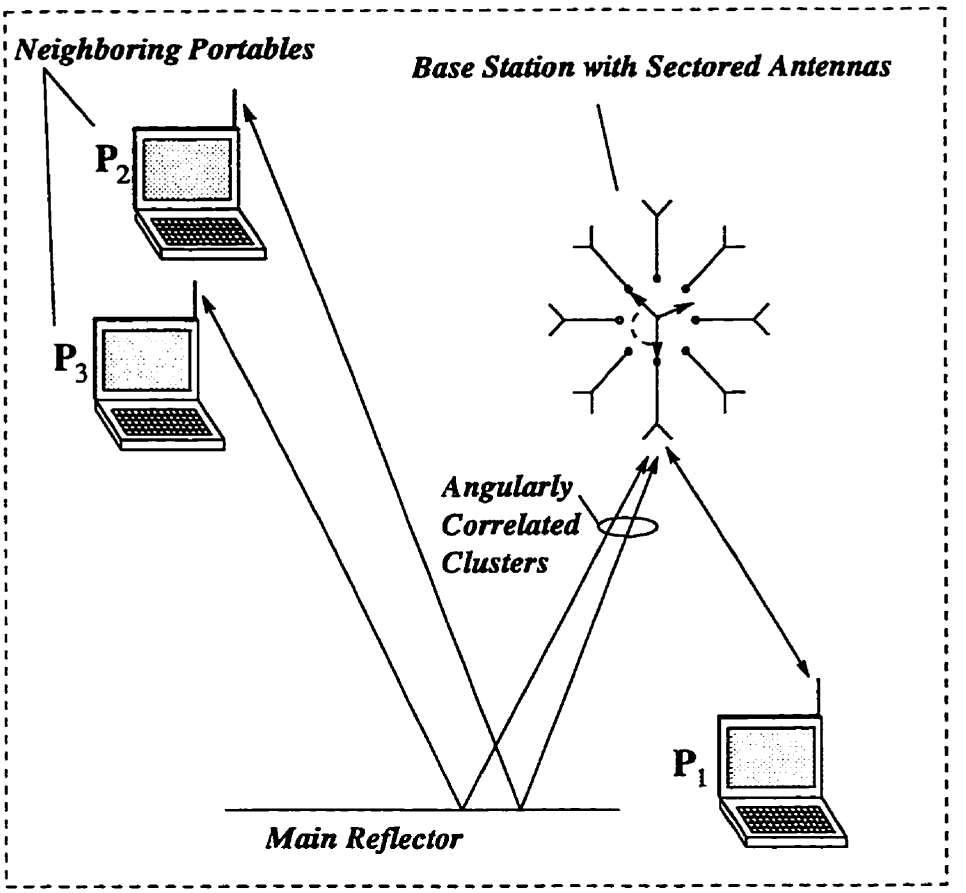

Figure 4.12: Illustration of angular correlation between clusters of neighboring portables creating incompatibility with a third portable

FFA Maximum Throughput as a Function of Sectorization Level

Figure 4.13 shows the FFA maximum throughput obtained with sectorization levels of 4, 10, 20 and 50 sectors, and with $\Gamma = 10.0$ ns, $\gamma = 10.0$ ns, $1/\Lambda = 16.8$ ns, $1/\lambda = 5.1$ ns and $\sigma = 25.5°$. The number of ports used to obtain the results were 3, 5, 7 and 11 when using 4, 10, 20 and 50 sectors, respectively.

These results show that there is considerable potential for increasing the maximum throughput by increasing the number of sectors in the microcell. The limit to this capacity gain seems to be related to the complexity of the sectored antenna system, since it is not obvious to us that, for example, a 50-sector antenna system built to operate at a frequency of 5.8 GHz can be made compact enough to be installed indoors.

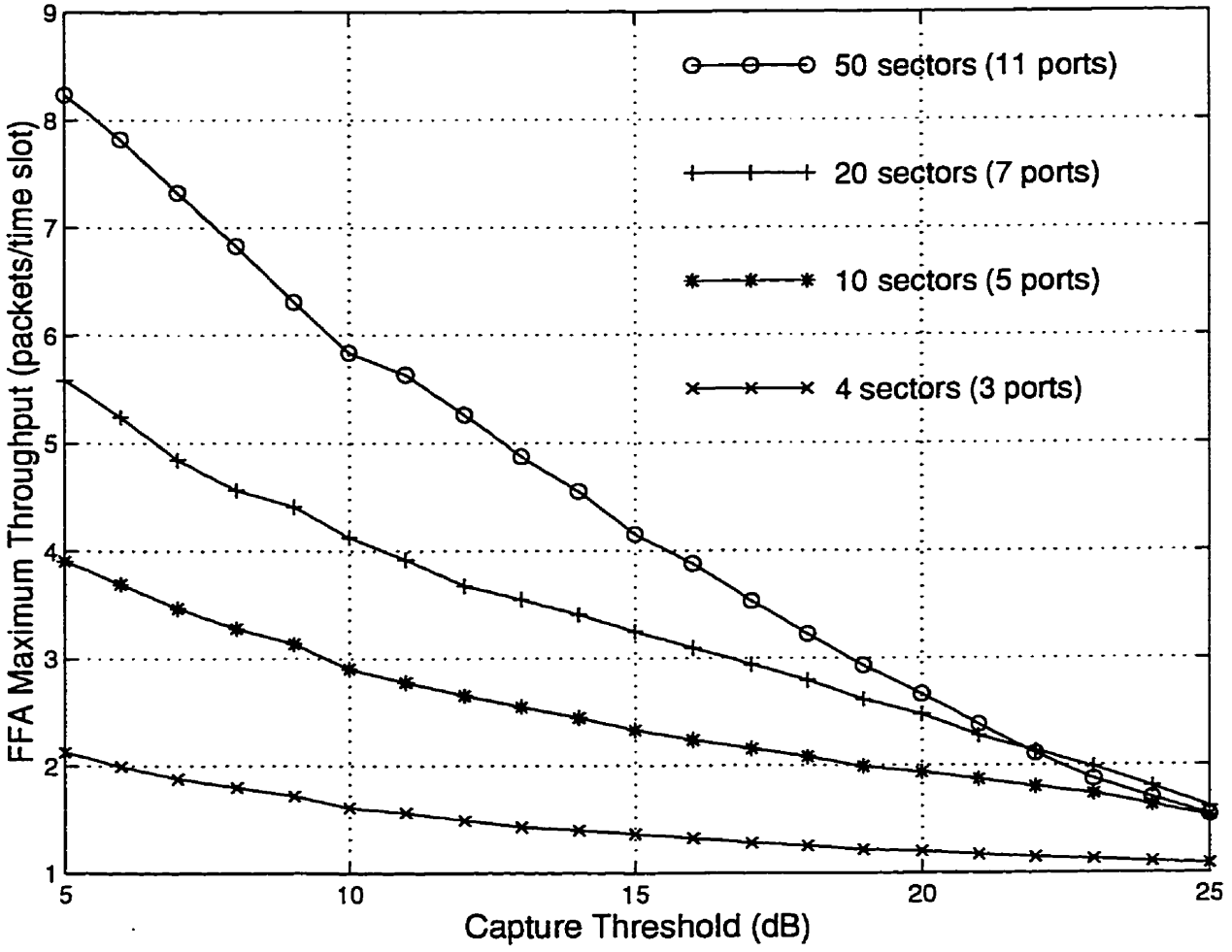

Figure 4.13: FFA maximum throughput with 4, 10, 20 and 50 sectors

Chapter 5

FFA Maximum Throughput with Multi-Carrier Modulation

5.1 Introduction

In the previous chapters, the FFA maximum throughput was investigated as a function of the capture threshold. However, the question may arise of which value of capture threshold a system can operate with. Of course the answer depends on the type of modulation and coding being used by the system.

The aim of this chapter is to investigate the performance of the proposed multiple access scheme assuming the use of multi-carrier modulation. This type of modulation [18] - [21] was chosen because it is naturally resistant to channel dispersion which occurs in indoor channels due to multipath propagation. This phenomenon affects signals when they operate at a symbol rate such that the symbol period is comparable to the channel time dispersion. In this case, Inter Symbol Interference (ISI) causes an intolerable degradation in the Bit Error Rate (BER) performance. To illustrate this phenomenon, let us assume that the signal of Figure 5.1, with a symbol rate of $\frac{1}{T}$, is transmitted through the two-path channel in Figure 5.2. The received signal is composed of the original signal, which is received through the main path, plus a delayed and attenuated copy, which is received through the

second path. This is illustrated in Figure 5.3. In order to recover (detect) the information carried by symbol i, the demodulator observes the received signal during the observation period i. However, as illustrated in Figure 5.3, part of the energy received on the delayed path during observation period i belongs to symbol $i-1$, which is characterized as ISI. Note also that, during observation period i, the remaining energy in the delayed path belongs to symbol i. This interference of symbol i with itself does not characterize ISI, but its effect can be destructive or constructive, depending on the relative phase of the two paths. In any case, the effect remains unchanged for many symbol periods since, in the case of indoor channels with a bit rate of 20 Mb/s, the coherence time of the channel is much larger than the symbol period. Therefore this type of distortion can be dealt with by means of diversity (for example, antenna diversity). On the other hand, ISI is a totally unpredictable type of interference which generates different distortion in every symbol period.

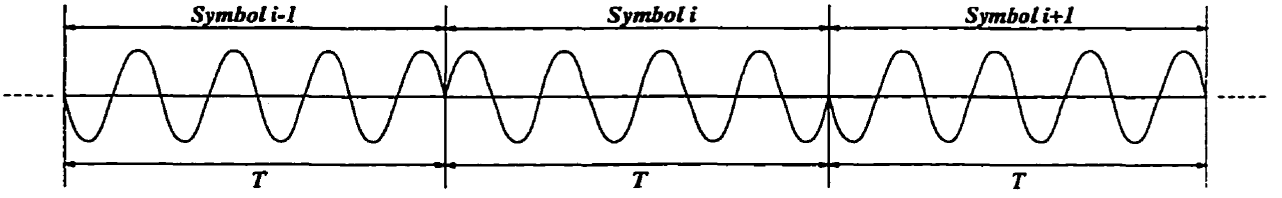

Figure 5.1: Signal with a symbol rate of $\frac{1}{T}$

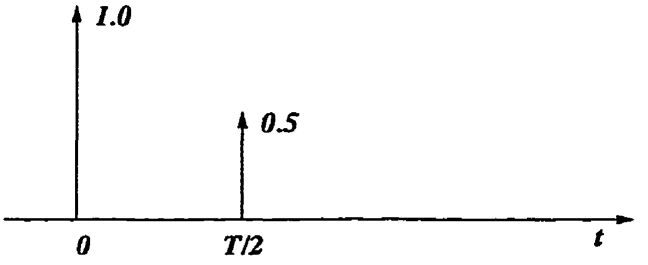

Figure 5.2: A two-path channel

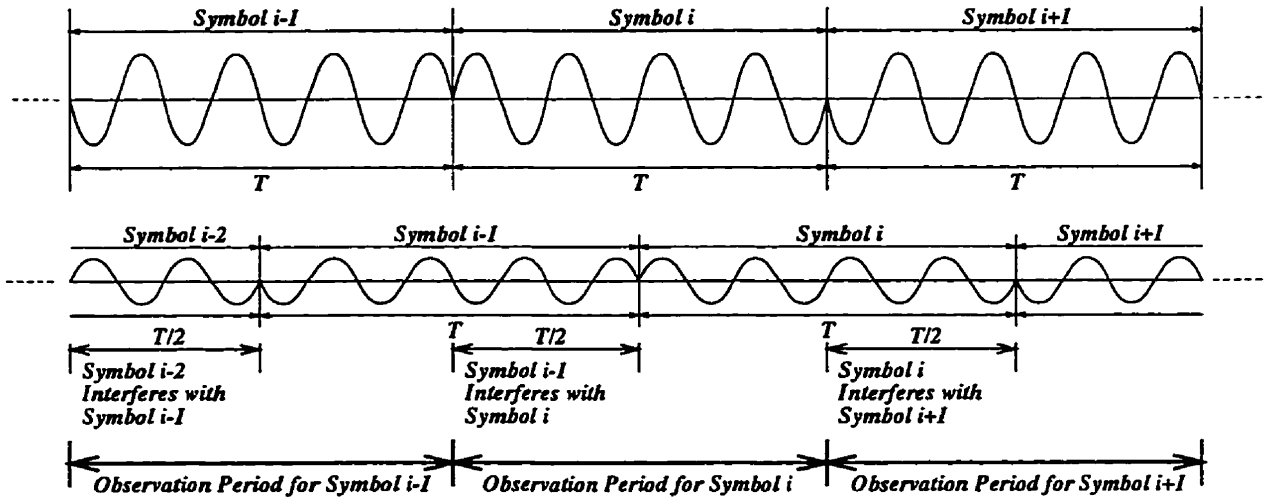

Figure 5.3: Illustration of Intersymbol Interference

The two-path channel in Figure 5.2 was used for illustrative purposes. A more realistic model for the indoor channel considers the arrival of many paths:

$$g(t) = \sum_{i=1}^{P} \beta_i \delta(t - \tau_i). \tag{5.1}$$

In order to be able to access quantitatively the effect of ISI, we need a convenient numerical measure of the time dispersion. The simplest measure is the *excess delay spread*, which is the overall span of path delays, i.e, time of last arrival minus time of first arrival $(\tau_P - \tau_1)$. However, this may not be a good indicator of how any given system would perform on the channel since different channels with the same excess delay spread can exhibit very different profiles of signal intensity over the delay span which will have different impacts on system performance. A better measure of channel dispersion is the root mean square *(rms) delay spread*, τ_{rms}, which is the second central moment of the channel impulse response:

$$\tau_{\text{rms}} = \sqrt{\overline{\tau^2} - (\overline{\tau})^2}, \tag{5.2}$$

where

$$\overline{\tau^n} = \frac{\sum_{i=1}^{P} \tau_i^n |\beta_i|^2}{\sum_{i=1}^{P} |\beta_i|^2}, \quad n = 1, 2.$$

In the literature, τ_{rms} is used to give a rough indication of the maximum data rate which can be reliably transmitted through the channel when using a single carrier modulation scheme, and when no special precaution, such as equalization, is taken. An estimate of the maximum data rate R_{max} is given by [33]

$$R_{\text{max}} = \frac{1}{4\tau_{\text{rms}}}. \tag{5.3}$$

We used the multi-path statistical model described in Chapter 4 to obtain the τ_{rms} for the two buildings whose parameters are given in Table 4.1. We considered sectorization levels of 5, 10 and 20. For each sectorization level, we calculated the τ_{rms} of 100 positions for each building. In Figures 5.4 and 5.5, the variations in τ_{rms} are shown for Building 1

and Building 2, respectively, by means of the Cumulative Distribution Functions (CDF). By substituting the values of τ_{rms} into Equation 5.3, we obtained the values of R_{max}, and plotted their CDFs in Figures 5.6 and 5.7, respectively.

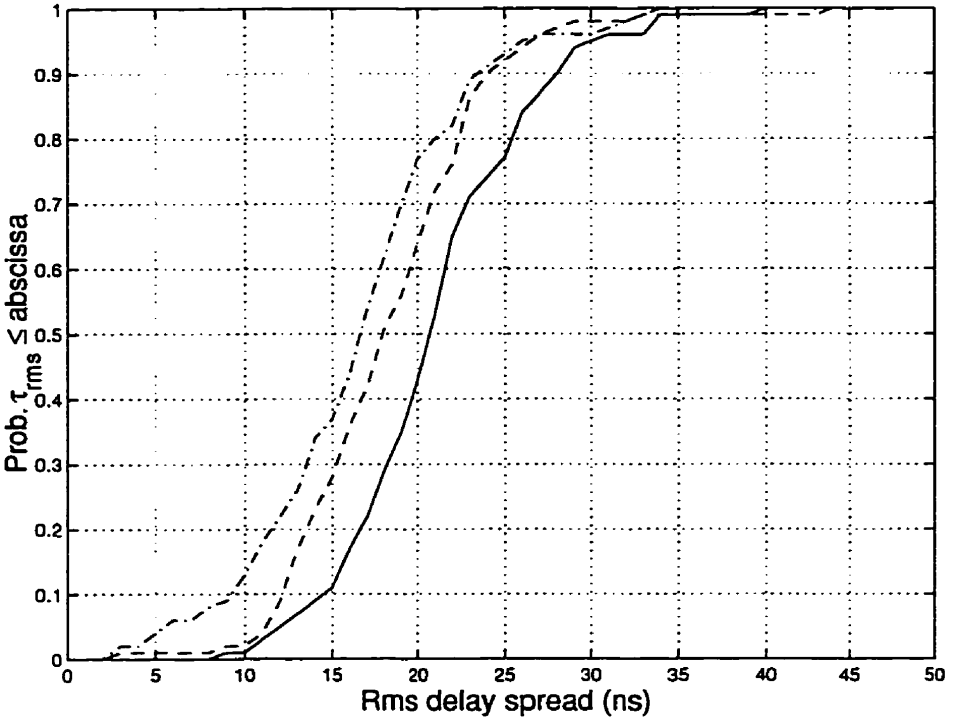

Figure 5.4: CDF of τ_{rms} in Building 1 with five sectors (solid), ten sectors (dashed), and 20 sectors (dash-dot)

Let us investigate how the 4-ary CPFSK modulation scheme of the ALTAIR system would perform in these channels at a bit rate of 20 Mbps, which is roughly the bit rate to be adopted in U-NII networks [9]. This bit rate corresponds to a symbol rate of 10 Msymbol/s for the 4-ary CPFSK modulation scheme. In this case, Figure 5.6 shows that, in Building 1, the probability of outage is about 0.2 if a sectorization level of 5 is used, and about 0.08 if a sectorization level of 20 is used. Similarly, Figure 5.7 shows that, in Building 2, the probability of outage is about 0.55 if a sectorization level of 5 is used, and about 0.3 if a sectorization level of 20 is used. Therefore we analyzed two sample indoor environments where the modulation scheme of the ALTAIR system would not provide acceptable

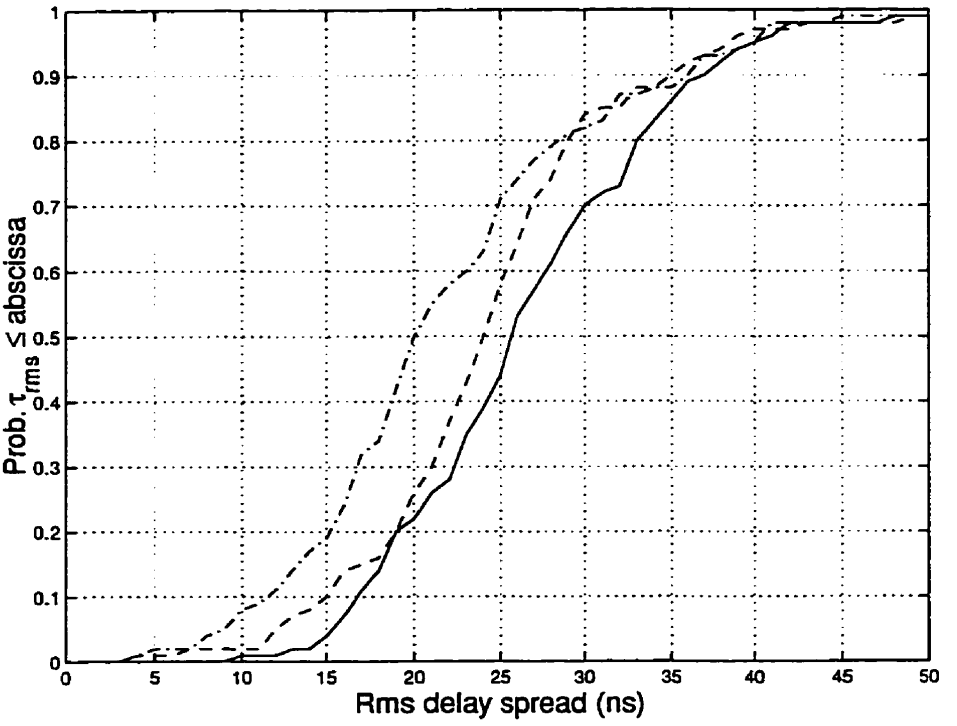

Figure 5.5: CDF of τ_{rms} in Building 2 with five sectors (solid), ten sectors (dashed), and 20 sectors (dash-dot)

performance. We recall that the ALTAIR system employs sectored antennas in both the base station (CM) and the portable (UM) (six sectors in each transceiver). This provides channels with smaller τ_{rms} values than those observed in Figures 5.4 and 5.5, which translates directly into reduced probability of outage due to ISI. The price paid in the ALTAIR system for the reduced delay spread is the complexity of the portable transceiver: six sectored antennas and a switch matrix to select one of them. However, we consider that the size of the antenna system is the main drawback to having a portable transceiver that also uses sectored antennas. In the case of the ALTAIR system which operates at 18 GHz, the antennas can be small (typically a 6×16 mm cross section [7]), making it possible to integrate several of them to the portable transceiver. However, when operating at 5 GHz, the antennas can not be made so compact. Therefore, we proposed using an omni-directional antenna in the portable transceiver.

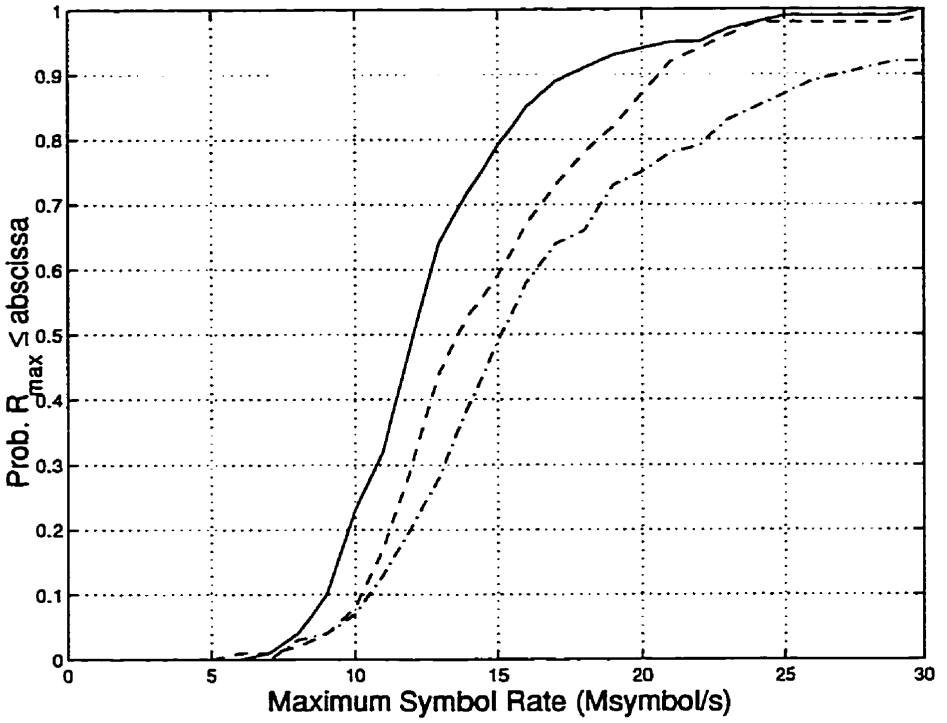

Figure 5.6: CDF of $R_{\max}$ in Building 1 with five sectors (solid), ten sectors (dashed), and 20 sectors (dash-dot)

Having shown that a single carrier modulation scheme will not perform well (at least when no special precautions are taken), we now need to obtain means to transmit reliably at the required high bit rates. One of the possible solutions is to use adaptive equalization [22]. However according to Mitzlaff [7], there are practical difficulties created by the sheer size, expense, and power consumption of the hardware needed to equalize a 10 Mb/s data signal. Because equalizing a 20 Mb/s data signal seems to be a challenging proposition, we adopted multi-carrier modulation as the solution to combat ISI. Figure 5.8 illustrates why multi-carrier modulation is resistant to ISI. This figure represents a two-carrier signal that is transmitted through the two-path channel of Figure 5.2. The two carriers are orthogonal, so they do not interfere with each other. Note that the symbol rate for each carrier is half the symbol rate for the single carrier in Figure 5.3, However, since the even symbols are transmitted in one carrier and the odd symbols are transmitted in the other, together these

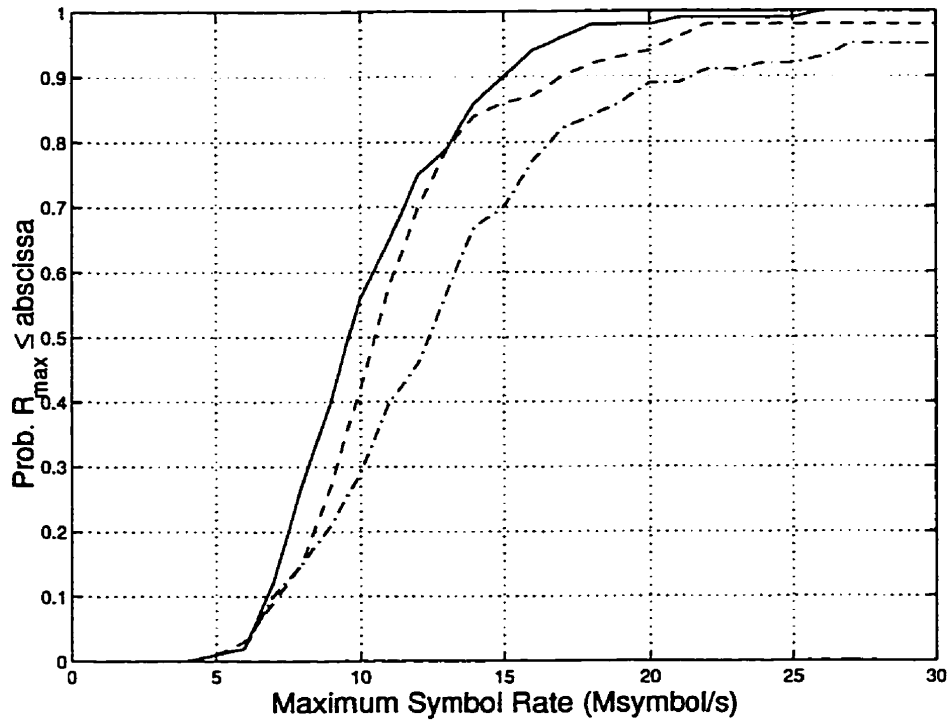

Figure 5.7: CDF of $R_{\max}$ in Building 2 with five sectors (solid), ten sectors (dashed), and 20 sectors (dash-dot)

two parallel signals transmit at the same symbol rate as that of the signal in Figure 5.3. By comparing Figures 5.3 and 5.8, we can see that the single carrier signal and the two-carrier signal are subject to the same excess delay spread of $\frac{T}{2}$, which is obvious because excess delay spread is a physical characteristic of the channel. However, in Figure 5.3 the excess delay spread corresponds to $\frac{1}{2}$ of the observation period while in Figure 5.8 it corresponds to only $\frac{1}{4}$ of the observation period. Therefore ISI is attenuated by half in the two-carrier signal. If we use four carrier, the ISI is attenuated by $\frac{1}{4}$ because the observation period is increased to $4T$, and as we increase the number of carriers, the observation period increases proportionally while the excess delay spread of the channel remains fixed. Therefore, the attenuation in ISI is given by $\frac{1}{N}$, where N is the number of carriers.

There is a technique that can be used to completely eliminate the ISI which consists of transmitting a cyclic prefix for each symbol. Figure 5.9 illustrates this technique. This

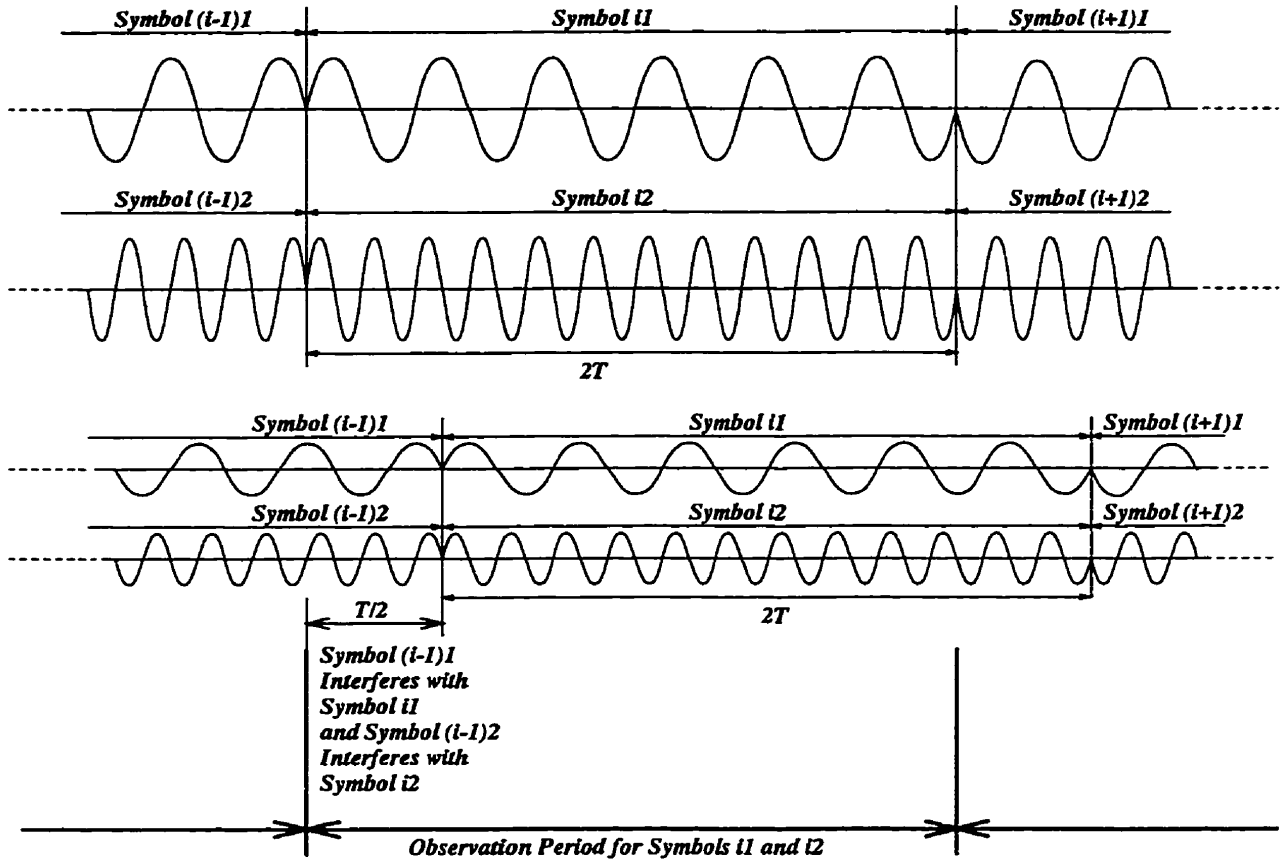

Figure 5.8: A two-carrier signal

figure considers that the signal was transmitted through the two-path channel of Figure 5.2. We can see that, during the observation period for symbol i, half of the energy received on the delayed path belongs to symbol i cyclic prefix, and the other half belongs to symbol i itself. Therefore, the ISI was completely eliminated. The drawback against this technique is the extra energy of the cyclic prefix that has to be transmitted for each symbol. We can see in the figure that guard periods are introduced between observation periods, so the energy of the cyclic prefix is wasted. However, when combined with multi-carrier modulation, this extra energy can be made as small as wished by increasing the number of carriers.

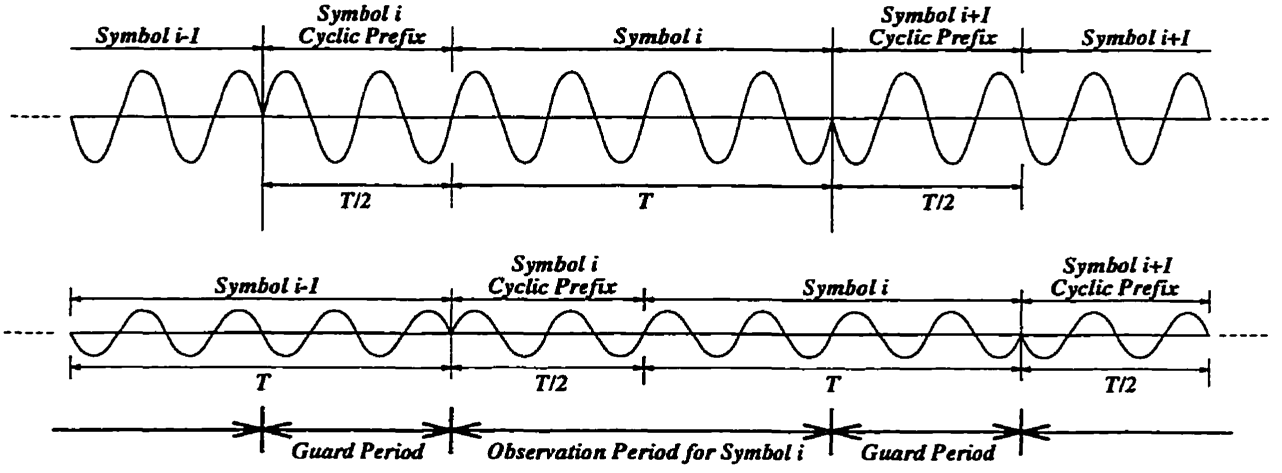

Figure 5.9: Illustration of the cyclic prefix technique

5.2 Orthogonal Frequency Division Multiplex

The specific type of multi-carrier modulation explored in this chapter is Orthogonal Frequency Division Multiplex (OFDM) which is popular because it can be generated and demodulated using Fast Fourier Transforms (FFTs). The baseband OFDM signal can be expressed as

$$S(t) = \sum_{i=-\infty}^{\infty} \sum_{n=0}^{N-1} A_{i,n} e^{j2\pi f_n t} \, w(t), \tag{5.4}$$

where

$$f_n = \frac{n}{T_O} \qquad n = 0, ..., N-1 \qquad w(t) = \begin{cases} 1, & 0 \le t \le T_S \\ 0, & \text{otherwise.} \end{cases}$$

Here, N is the number of carriers, T_O is the observation period, and T_S is the symbol duration ($T_S = T_O +$ *cyclic prefix*). Therefore the guard period is given by $\Delta = T_S - T_O$. The term $A_{i,n}$ represents the information symbol transmitted by the n-th carrier during the i-th symbol period.

Figure 5.10 (a) and (b) show the block diagrams of an OFDM transmitter and receiver, respectively. In the transmitter, the information sequence is applied to a serial to parallel converter (S/P), where N symbols are assembled. Each assembled vector $\{A_{i,n}|_{n=0,1,2,...,N-1}\}$ is padded with $(J-1)N$ zeros. Then the JN-point inverse discrete Fourier transform (IDFT) is performed on the resulting vector. It is easy to see that the output of the IDFT corresponds to JN samples of the baseband OFDM signal of Eq.(5.4) taken during the i-th symbol period at a sampling rate $f_{samp} = JN/T_O$. These samples are applied to a parallel to serial (P/S) converter, and the real and imaginary parts are applied to digital to analog converters (D/A). The output signals of the D/A converters are low-pass filtered to generate the complex signal $S(t)$ of Eq.(5.4). Then, real and imaginary parts of $S(t)$ are used to modulate the in-phase and quadrature components of the RF carrier, respectively.

In the receiver, the received signal $R(t)$ is down-converted, and JN samples are taken during the i-th observation period. These samples are applied to a Discrete Fourier Transform (DFT) to obtain the Fourier coefficients of the signals in the observation period

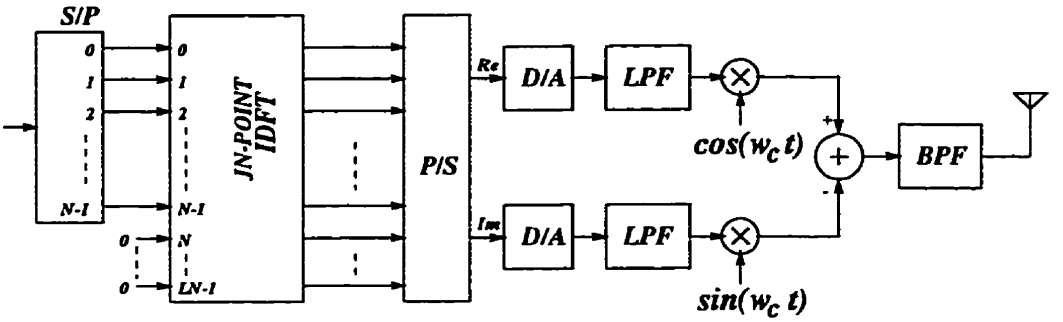

(a) Transmitter

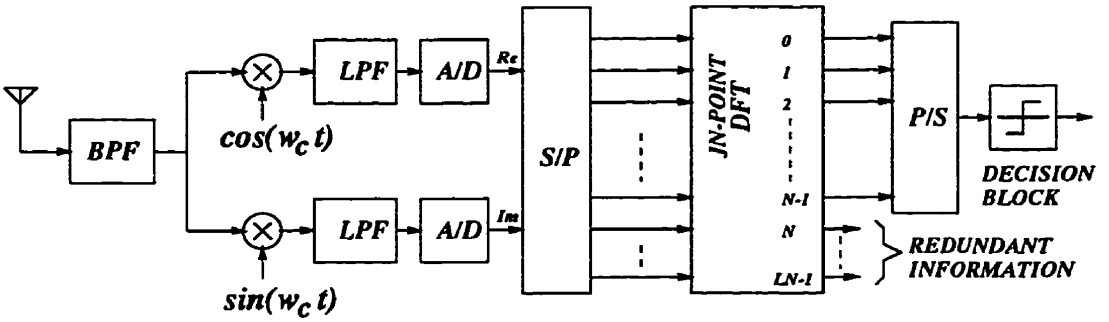

(b) Receiver

Figure 5.10: Block diagrams of an OFDM transmitter and receiver

$[iT_S, T_O + iT_S]$. The output $K_{i,n}$ of the n-th carrier at time iT_S is represented by

$$K_{i,n} = \frac{1}{T_O} \int_{iT_S}^{T_O+iT_S} R(t) e^{-j2\pi f_n (t-iT_S)} dt. \tag{5.5}$$

The demodulated vector $\{K_{i,n}\}$ is applied to a parallel to serial converter, and the decision block of the receiver decides which symbol was transmitted in the n-th carrier during the i-th symbol period.

5.3 OFDM Performance under Frequency Selective Fading

This section analyzes the BER performance of the OFDM in a frequency selective channel [1]. This type of channel can be modeled as a tapped delay line where each tap is an independent complex Gaussian random process. Assuming a static channel, the impulse response of the channel can be expressed as

$$g(t) = \sum_{l=1}^{P_1+P_2} \beta_l \delta(t - \tau_l), \tag{5.6}$$

where $\delta(t)$ represents the Dirac delta function; β_l is the complex envelope of the signal received on the l-th path which is assumed to be a complex Gaussian random process with zero mean and variance p_l; and τ_l is the propagation delay for the l-th path. It is assumed that for all paths, τ_l is not larger than the symbol duration T_S. Furthermore, τ_l are classified by the following inequalities:

$$\begin{aligned} 0 \leq \tau_l \leq \Delta \qquad & (l = 1, \ldots, P_1), \\ \Delta < \tau_l < T_S \quad & (l = P_1 + 1, \ldots, P_1 + P_2). \end{aligned} \tag{5.7}$$

When transmitting the OFDM signal through the channel expressed by Eq. (5.6), the received signal can be expressed as

$$R(t) = S(t) * g(t) + Z(t), \tag{5.8}$$

where $Z(t)$ represents added complex Gaussian noise. By substituting Eq. (5.6) into Eq. (5.8), and then into Eq. (5.5) we obtain

[1] The theory developed here is similar to the theory developed in [21].

$$K_{i,n} = A_{i,n}\Big\{ \sum_{l=1}^{P_1} \beta_l e^{-j2\pi f_n \tau_l} + \sum_{l=P_1+1}^{P_1+P_2} \frac{T_O - \tau_l + \Delta}{T_O} \beta_l e^{-j2\pi f_n \tau_l} \Big\}$$

$$- \sum_{l=P_1+1}^{P_1+P_2} \sum_{\substack{k=0 \\ k \neq n}}^{N-1} \frac{\tau_l - \Delta}{T_O} \beta_l e^{-j2\pi f_k \tau_l} \; e^{-j\pi(n-k)(\tau_l-\Delta)/T_O} \; \mathrm{sinc}[\pi(n-k)(\tau_l-\Delta)/T_O] A_{i,k}$$

$$+ \sum_{l=P_1+1}^{P_1+P_2} \sum_{k=0}^{N-1} \frac{\tau_l - \Delta}{T_O} \beta_l e^{-j2\pi f_k (\tau_l - T_O)} \; e^{-j\pi(n-k)(\tau_l-\Delta)/T_O} \; \mathrm{sinc}[\pi(n-k)(\tau_l-\Delta)/T_O] A_{i-1,k}$$

$$+ z_{i,n}, \tag{5.9}$$

where

$$\mathrm{sinc(x)} = \frac{\sin(\mathrm{x})}{\mathrm{x}}. \tag{5.10}$$

The first term in this Eq.(5.9) represents the desired signal component distorted by the multi-path channel, the second and third terms represent Inter Channel Interference (ICI) and ISI, respectively. We can see that the second and the third terms are completely eliminated when the guard period Δ is larger than or equal to the largest path delay $\tau_{P_1+P_2}$. In this case Eq.(5.9) can be rewritten as

$$\begin{aligned} K_{i,n} &= A_{i,n}\Big\{ \sum_{l=1}^{P_1+P_2} \beta_l e^{-j2\pi f_n \tau_l} \Big\} + z_{i,n} \\ &= A_{i,n} C_n + z_{i,n}, \end{aligned} \tag{5.11}$$

where C_n is the channel response in the n-th carrier when the ISI is completely eliminated by the cyclic prefix:

$$C_n = \sum_{l=1}^{P_1+P_2} \beta_l e^{-j2\pi f_n \tau_l}. \tag{5.12}$$

The last term, $z_{i,n}$, is a complex Gaussian noise component with zero mean and variance σ_z^2.

The average Signal to Noise plus Interference Ratio (SNIR) for the n-th carrier is given by

$$\overline{\rho}_n = \frac{b_n}{\sigma_{I,n}^2 + \sigma_z^2}, \tag{5.13}$$

where b_n is the average power of the desired signal of n-th carrier related to the first term of Eq.(5.9). Let us assume that each symbol $A_{i,n}$ of the information sequence is chosen out of $\{e^{j2\pi m/M}|_{m=0,1,\ldots,M-1}\}$. Then b_n can be expressed as

$$b_n = \sum_{l=1}^{P_1} p_l + \sum_{l=P_1+1}^{P_1+P_2} \left(\frac{T_O - \tau_l + \Delta}{T_O}\right)^2 p_l, \tag{5.14}$$

and $\sigma_{I,n}^2$ is the power of the interference related to the second and third terms of Eq.(5.9):

$$\sigma_{I,n}^2 = \left[\sum_{l=P_1+1}^{P_1+P_2} \left(\frac{\tau_l - \Delta}{T_O}\right)^2 p_l\right]\left[\sum_{k=0}^{N-1} \mathrm{sinc}^2[\pi(n-k)(\tau_l - \Delta)/T_O] - 1/2\right]. \tag{5.15}$$

The first term of Eq.(5.9) is the sum of $(P_1 + P_2)$ zero mean complex Gaussian random variables, therefore the envelope of this term is a Rayleigh random variable. Moreover, the second and third terms of Eq.(5.9) are complex Gaussian random variables since they are sums of complex Gaussian random variables. Therefore, in order to calculate the Bit Error Rate (BER) in the n-th carrier, we can make use of the expression developed in [22]-p.786 for M-ary PSK under Rayleigh fading. In the case of QDPSK (Quadrature Differential Phase Shift Keying) with differential detection, the BER of the n-th carrier is given by

$$P_{b,n} = \frac{1}{2}\left[1 - \frac{\mu_n}{\sqrt{2 - \mu_n^2}}\right], \tag{5.16}$$

where

$$\mu_n = \frac{\overline{\rho}_n}{1 + \overline{\rho}_n}. \tag{5.17}$$

In QDPSK, the symbols are differentially encoded before transmission:

$$D_{i,n} = D_{i-1,n} A_{i,n}, \tag{5.18}$$

which allows using differential detection in the receiver, so there is no need for phase estimation. This is useful in the reception of short data packets, where there is not enough

time for phase acquisition, and in channels where tracking the phase is difficult due to fast fading.

To confirm the validity of these equations, BER performance based on this theory was compared with the results of computer simulations. The channel model used was a 16-ray Rayleigh fading channel where the strength of each ray fluctuates independently with the Rayleigh distribution. Figure 5.11 illustrates the Power Delay Profile (PDP) of the proposed channel model. This PDP is based on indoor measurement results which are reported in [16]. Assuming that the number of carriers is $N = 32$, Figure 5.12 shows the average bit error rate performance over the 32 carriers, which can be computed by

$$P_b = \frac{1}{N} \sum_{n=0}^{N-1} P_{b,n}. \tag{5.19}$$

Each carrier was modulated by QDPSK at a symbol rate of (20/32) Msymbol/s, so the total symbol rate was 20 Msymbol/s. The pulse energy to noise density ratio, Eb/No, was set to 30 dB. Simulations were run for five values of the cyclic prefix, or guard period ($\Delta =$ 0, 50, 100, 150 and 200 ns). With a guard period of 200 ns, which is larger than the excess delay spread of the channel (see Figure 5.11), the second and third terms of Eq.(5.9) are eliminated, and the extra power of the cyclic prefix is 0.51 dB. Therefore, when using 32 carriers, the ISI can be completely eliminated with only 0.51 dB of extra transmitted power. It can be seen that the theoretical results agreed well with the simulation results.

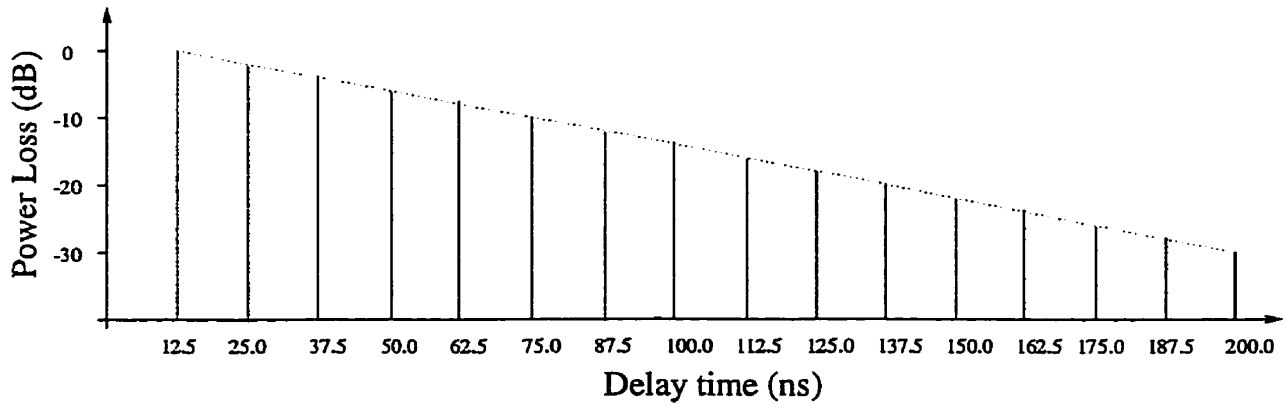

Figure 5.11: Power delay profile of a 16-path indoor channel

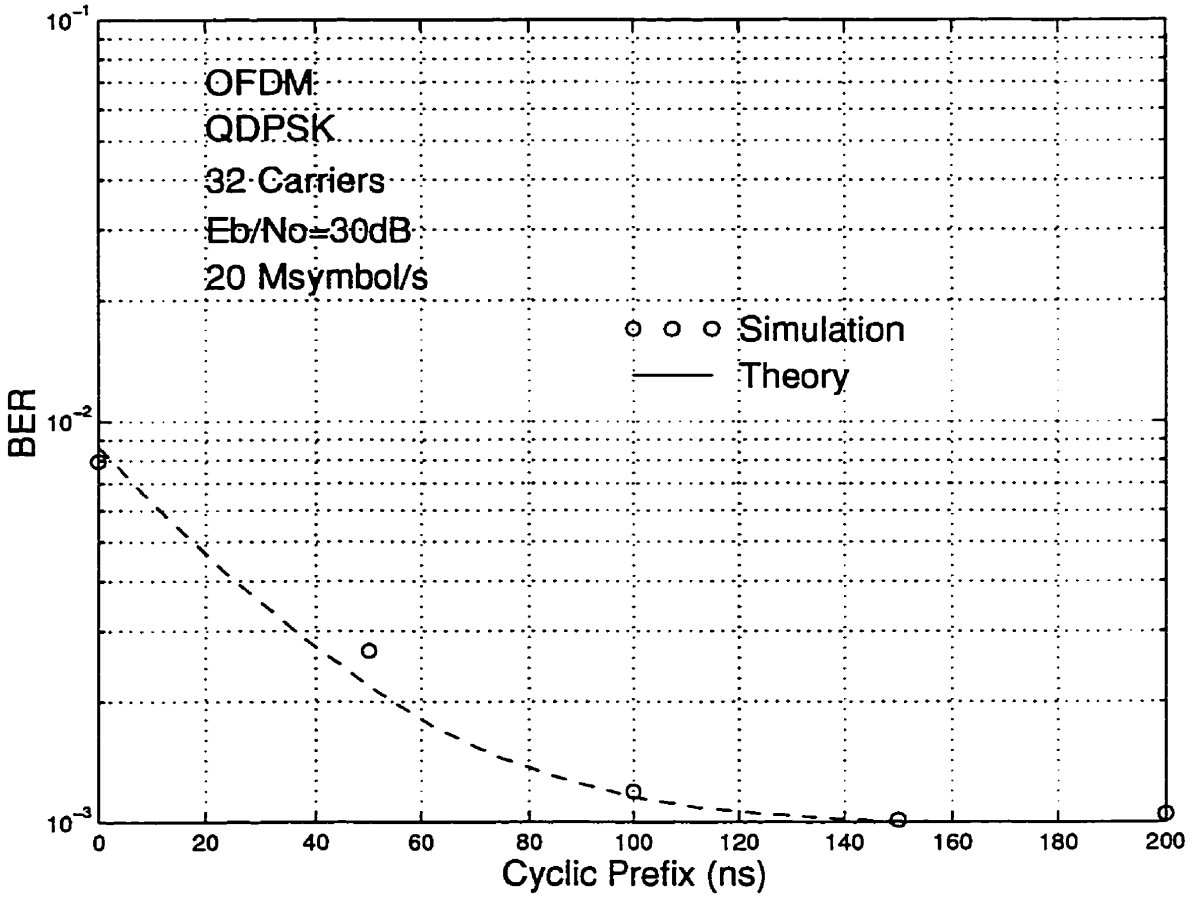

Figure 5.12: Theoretical and simulation results of QDPSK OFDM in a frequency selective channel

5.4 Alternative OFDM

We have seen in Figure 5.10 that a JN-point IDFT is used in the modulation of an N-carrier OFDM signal, and a JN-point DFT is used in the demodulation. With the JN-point IDFT, samples of the transmit signal are generated at a sampling rate of $f_{samp} = JN/T_O$. Bingham [19] stated that if $f_{samp} = 2N_{tot}/T_O$, then N_{tot} carriers are available for modulation, which makes $J = 2$. In this section we analyse an alternative OFDM signal proposed by Macedo and Sousa [1] where $J = 1$. The main merit of this alternative OFDM signal is that it can be generated using an N-point IDFT, and demodulated using an N-point DFT, while the conventional OFDM requires at least a $2N$-point IDFT in the generation and a $2N$-point DFT in the demodulation. Therefore, with this alternative OFDM, there is the potential to cut the amount of processing by $\frac{1}{2}(\frac{1}{1+1/\log_2 N})$.

Figure 5.13 compares the four-carrier conventional OFDM signal with the four-carrier alternative OFDM signal. In Figure 5.13-a, an 8-point IDFT is used to generate eight samples per observation period T_O of a four-carrier OFDM signal. As seen in this figure, padding with zeros is required in order to obtain the appropriate sampling rate which has to be at least $\frac{2N}{T_O}$. Figure 5.13-b illustrates how the alternative OFDM signal can be generated in the case of four carriers. During the i-th symbol period, the vector $\{S_{i,k}\}$ is generated by taking the N-point IDFT of the information vector $\{A_{i,n}\}$ (without padding with zeros). The elements of the vector $\{S_{i,k}\}$ are then serially transmitted by Nyquist pulses with a signaling rate of $1/T$, where $T = T_O/N$. Here, a cyclic prefix can also be added to combat ISI. The resulting signal has a symbol period of $T_S = T_O + pT$, where pT is the cyclic prefix, and p is an integer. Figure 5.14 illustrates one symbol period of the alternative OFDM signal with and without the addition of a cyclic prefix of size $p = 2$.

The baseband transmitted signal can be expressed as

$$S(t) = \sum_{i=-\infty}^{\infty} \sum_{k=-p}^{N-1} S_{i,k} h(t - kT - iT_S), \tag{5.20}$$

where

$$S_{i,k} = \sum_{n=0}^{N-1} A_{i,n} e^{j\frac{2\pi nk}{N}}, \quad (S_{i,-k} = S_{i,N-k-1})|_{k=1,2,\ldots,p}, \tag{5.21}$$

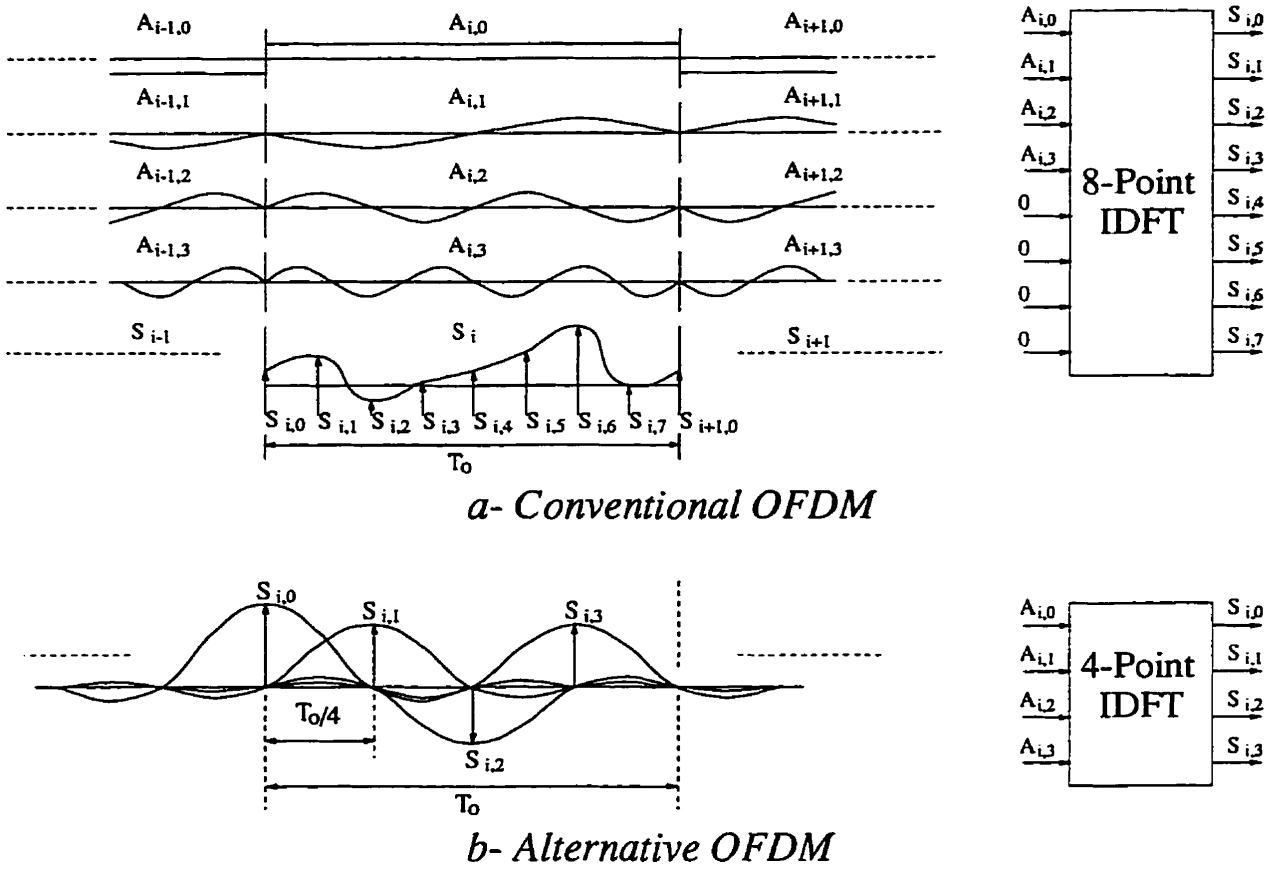

Figure 5.13: (a) Conventional and (b) alternative OFDM signals

and $h(t)$ is the Nyquist pulse waveform. More precisely, $h(t)$ is assumed to be the raised cosine pulse, which can be expressed as

$$h(t) = \left[\frac{\sin(\pi t/T)}{\pi t/T}\right]\left[\frac{\cos(\alpha\pi t/T)}{1-(2\alpha t/T)^2}\right], \tag{5.22}$$

where α is the rolloff factor. The real and imaginary parts of $S(t)$ are then used to modulate the in-phase and quadrature components of the RF carrier, respectively.

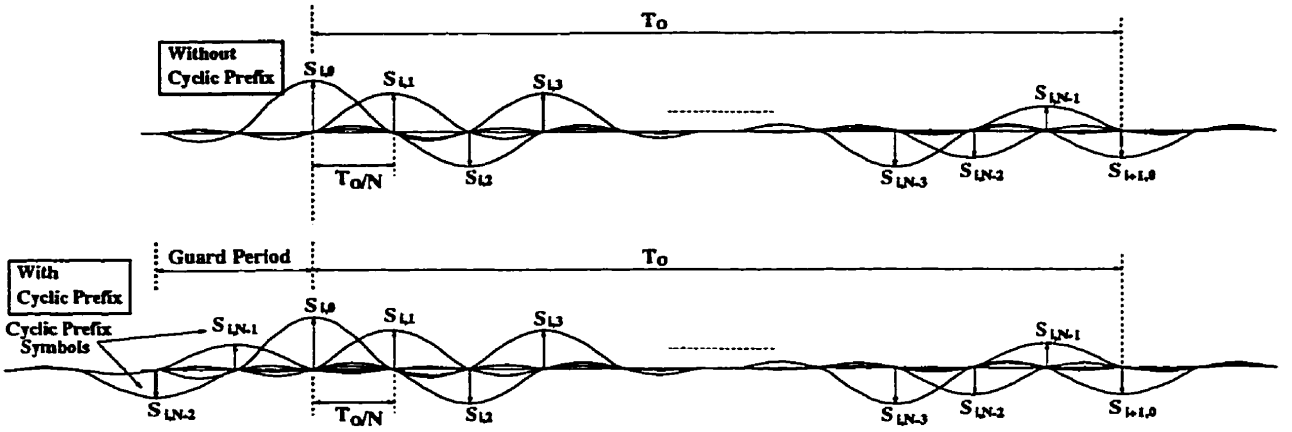

Figure 5.14: The alternative OFDM signal without and with a cyclic prefix

5.5 Alternative OFDM under Frequency Selective Fading

This section analyzes the BER performance of the alternative OFDM in a frequency selective channel. This type of channel can be modeled as a tapped delay line of Eq.(5.6), which we rewrite as

$$g(t) = \sum_{l=1}^{P} \beta_l \delta(t - \tau_l), \tag{5.23}$$

where $\delta(t)$ represents the Dirac delta function; β_l is the complex envelope of the signal received on the l-th path which is assumed to be a complex Gaussian random process with zero mean and variance p_l; and τ_l is the propagation delay for the l-th path. It is assumed that for all paths, τ_l is not larger than the symbol duration T_S.

When transmitting the alternative OFDM signal through the channel expressed by Eq. (5.23), the received signal can be expressed as

$$R(t) = S(t) * g(t) + Z(t), \tag{5.24}$$

where $Z(t)$ represents added complex Gaussian noise. By substituting Eq. (5.20) and Eq. (5.23) into Eq. (5.24) we obtain

$$R(t) = \sum_{i=-\infty}^{\infty} \sum_{k=0}^{N-1} \sum_{l=1}^{P} \beta_l S_{i,k} h(t - kT - iT_S - \tau_l) + Z(t). \tag{5.25}$$

In order to demodulate the i-th symbol, N samples of $R(t)$ are taken at times $t = uT + iT_S$. The generated samples are

$$R_{i,u} = R(t)|_{t=uT+iT_S}. \tag{5.26}$$

For simplification purposes, let us express $R_{i,u}$ as a function of G_m, where G_m is defined as

$$G_m \stackrel{\text{def}}{=} \sum_{l=1}^{P} \beta_l h(mT - \tau_l). \tag{5.27}$$

The values of $R_{i,u}$ can be approximated considering that G_m has significant values only for $-L \leq m \leq L$. For example, for $L = 2$, $R_{i,u}$ can be expressed as[2]

$$\begin{bmatrix}
R_{i,0} \simeq & S_{i-1,N-2}G_2 & +S_{i,N-1}G_1 & +S_{i,0}G_0 & +S_{i,1}G_{-1} & +S_{i,2}G_{-2} & +Z_{i,0} \\
R_{i,1} \simeq & S_{i,N-1}G_2 & +S_{i,0}G_1 & +S_{i,1}G_0 & +S_{i,2}G_{-1} & +S_{i,3}G_{-2} & +Z_{i,1} \\
R_{i,2} \simeq & S_{i,0}G_2 & +S_{i,1}G_1 & +S_{i,2}G_0 & +S_{i,3}G_{-1} & +S_{i,4}G_{-2} & +Z_{i,2} \\
 & & & \vdots & & & \\
R_{i,N-3} \simeq & S_{i,N-5}G_2 & +S_{i,N-4}G_1 & +S_{i,N-3}G_0 & +S_{i,N-2}G_{-1} & +S_{i,N-1}G_{-2} & +Z_{i,N-3} \\
R_{i,N-2} \simeq & S_{i,N-4}G_2 & +S_{i,N-3}G_1 & +S_{i,N-2}G_0 & +S_{i,N-1}G_{-1} & +S_{i+1,0}G_{-2} & +Z_{i,N-2} \\
R_{i,N-1} \simeq & S_{i,N-3}G_2 & +S_{i,N-2}G_1 & +S_{i,N-1}G_0 & +S_{i+1,0}G_{-1} & +S_{i+1,1}G_{-2} & +Z_{i,N-1}
\end{bmatrix}, \tag{5.28}$$

[2]Here we are assuming a cyclic prefix of $p = 1$.

which can be rearranged as

$$\begin{bmatrix}
R_{i,0} \simeq & S_{i-1,N-2}G_2 & & & & & & \\
& -S_{i,N-2}G_2 & & & & & & \\
& +S_{i,N-2}G_2 & +S_{i,N-1}G_1 & +S_{i,0}G_0 & +S_{i,1}G_{-1} & +S_{i,2}G_{-2} & +Z_{i,0} & \\
R_{i,1} \simeq & S_{i,N-1}G_2 & +S_{i,0}G_1 & +S_{i,1}G_0 & +S_{i,2}G_{-1} & +S_{i,3}G_{-2} & +Z_{i,1} & \\
R_{i,2} \simeq & S_{i,0}G_2 & +S_{i,1}G_1 & +S_{i,2}G_0 & +S_{i,3}G_{-1} & +S_{i,4}G_{-2} & +Z_{i,2} & \\
& & & \vdots & & & & \\
R_{i,N-3} \simeq & S_{i,N-5}G_2 & +S_{i,N-4}G_1 & +S_{i,N-3}G_0 & +S_{i,N-2}G_{-1} & +S_{i,N-1}G_{-2} & +Z_{i,N-3} & \\
R_{i,N-2} \simeq & S_{i,N-4}G_2 & +S_{i,N-3}G_1 & +S_{i,N-2}G_0 & +S_{i,N-1}G_{-1} & +S_{i,0}G_{-2} & +Z_{i,N-2} & \\
& & & & & +S_{i+1,0}G_{-2} & & \\
& & & & & -S_{i,0}G_{-2} & & \\
R_{i,N-1} \simeq & S_{i,N-3}G_2 & +S_{i,N-2}G_1 & +S_{i,N-1}G_0 & +S_{i,0}G_{-1} & +S_{i,1}G_{-2} & +Z_{i,N-1} & \\
& & & & +S_{i+1,0}G_{-1} & +S_{i+1,1}G_{-2} & & \\
& & & & -S_{i,0}G_{-1} & -S_{i,1}G_{-2} & &
\end{bmatrix}. \tag{5.29}$$

By observing (5.29), $R_{i,u}$ can be expressed in terms of four components:

$$R_{i,u} = \Gamma_{i,u} + \Lambda_{i,u} + \Omega_{i,u} + Z_{i,u}, \tag{5.30}$$

where

$$\Gamma_{i,u} = \sum_{m=-L}^{L} S_{[i,(N+m+u) \bmod N]} G_m \quad 0 \le u \le N-1, \tag{5.31}$$

$$\Lambda_{i,u} = \sum_{m=u+p+1}^{L} (S_{i-1,N-m+u} - S_{i,N-m+u}) G_m \quad 0 \le u < L, \tag{5.32}$$

$$\Omega_{i,u} = \sum_{m=N-u}^{L} (S_{i+1,m+u-N} - S_{i,m+u-N}) G_{-m} \quad N-L \le u \le N-1, \tag{5.33}$$

and $Z_{i,u}$ represents the samples of the added Gaussian noise.

The next step in the demodulation of the i-th symbol, which carries the i-th information vector $\{A_{i,n}\}$, is to take the DFT of the vector $\{R_{i,u}\}$ to obtain

$$K_{i,n} = \gamma_{i,n} + \lambda_{i,n} + \omega_{i,n} + z_{i,n}, \tag{5.34}$$

where $\gamma_{i,n}$, $\lambda_{i,n}$, $\omega_{i,n}$ and $z_{i,n}$ are the DFT of the terms $\Gamma_{i,n}$, $\Lambda_{i,n}$, $\Omega_{i,n}$ and $Z_{i,n}$, given respectively by

$$\gamma_{i,n} = \frac{1}{N} \sum_{u=0}^{N-1} \Gamma_{i,u} e^{-j2\pi nu/N}, \tag{5.35}$$

$$\lambda_{i,n} = \frac{1}{N} \sum_{u=0}^{N-1} \Lambda_{i,u} e^{-j2\pi nu/N}, \tag{5.36}$$

$$\omega_{i,n} = \frac{1}{N} \sum_{u=0}^{N-1} \Omega_{i,u} e^{-j2\pi nu/N}, \tag{5.37}$$

and

$$z_{i,n} = \frac{1}{N} \sum_{u=0}^{N-1} Z_{i,u} e^{-j2\pi nu/N}. \tag{5.38}$$

By substituting Eq.(5.31) into Eq.(5.35), we obtain

$$\gamma_{i,n} = A_{i,n} \sum_{m=-L}^{L} G_m e^{-j2\pi mn/N} = A_{i,n} C_n. \tag{5.39}$$

Therefore $\gamma_{i,n}$ represents the information symbol transmitted by the n-th carrier multiplied by a distortion factor C_n which can be expressed as

$$\begin{aligned} C_n &= \sum_{m=-L}^{L} G_m e^{-j2\pi mn/N} \\ &= \sum_{l=1}^{P} \beta_l \sum_{m=-L}^{L} h(mT-\tau_l) e^{-j2\pi mn/N}. \end{aligned} \tag{5.40}$$

We can see that C_n is the sum of P zero mean complex Gaussian random variables, therefore its envelope is a Rayleigh random variable.

Let us assume that each element of the vector $\{A_{i,n}\}$ is chosen out of $\{e^{j2\pi m/M} | m = 0, 1, ..., M-1\}$. Therefore the average power of the n-th carrier can be expressed as

$$\begin{aligned} b_n^{alt} &= E[|C_n|^2] \\ &= \sum_{l=1}^{P} p_l \sum_{m=-L}^{L} \sum_{k=-L}^{L} h(mT-\tau_l) h(kT-\tau_l) \cos[2\pi(m-k)n/N]. \end{aligned} \tag{5.41}$$

The second and third terms of Eq. (5.34), $\lambda_{i,n}$ and $\omega_{i,n}$, represent Inter Symbol Interference (ISI). The term $\lambda_{i,n}$ represents interference coming from past symbols, and $\omega_{i,n}$ represents interference coming from future symbols. The third term, $z_{i,n}$, represents added Gaussian noise.

The interference power in the n-th carrier, related to the term $\lambda_{i,n}$, can be expressed as

$$\sigma_{\lambda,n}^2 = E[|\lambda_{i,n}|^2]. \tag{5.42}$$

By substituting Eq.(5.36) into Eq.(5.42) we obtain

$$\sigma_{\lambda,n}^2 = \frac{1}{N^2} \Big\{ \sum_{u=0}^{N-1} \sum_{k=0}^{N-1} E[\Lambda_{i,u} \Lambda_{i,k}^*] e^{-j2\pi n(u-k)/N} \Big\}. \tag{5.43}$$

Next, we substitute Eq.(5.32) into Eq.(5.43) to obtain

$$\begin{aligned} \sigma_{\lambda,n}^2 = \frac{1}{N^2} \sum_{u=0}^{L-1} \sum_{k=0}^{L-1} E\Big[& \sum_{m=u+p+1}^{L} \sum_{q=k+p+1}^{L} (S_{i-1,N-m+u} - S_{i,N-m+u}) G_m \\ & \times (S_{i-1,N-q+k}^* - S_{i,N-q+k}^*) G_q^* \Big] e^{-j2\pi n(u-k)/N}. \end{aligned} \tag{5.44}$$

Equation (5.44) can be further developed by noticing that

$$E[S_{i,j} S_{k,l}^*] = \begin{cases} N, & i = k \text{ and } j = l, \\ 0, & \text{otherwise}, \end{cases} \tag{5.45}$$

and that

$$E[G_m G_q^*] = \sum_{l=1}^{P} p_l h(mT - \tau_l) h(qT - \tau_l). \tag{5.46}$$

Therefore, Eq.(5.44) can be developed into

$$\sigma^2_{\lambda,n} = \frac{1}{N} \sum_{l=1}^{P} p_l \sum_{u=0}^{L-1} \sum_{k=0}^{L-1} \sum_{m=u+p+1}^{L} \sum_{q=k+p+1}^{L} I(u,k,m,q) h(mT - \tau_l) h(qT - \tau_l) \cos[2\pi(u-k)n/N], \tag{5.47}$$

where

$$I(u,k,m,q) = \begin{cases} 1, & u - m = k - q, \\ 0, & \text{otherwise}, \end{cases} \tag{5.48}$$

and p is the size of the cyclic prefix. Similarly, the interference power in the n-th carrier, related to the term $\omega_{i,n}$, can be developed, and expressed as

$$\begin{aligned} \sigma^2_{\omega,n} \;=\; & \frac{1}{N} \sum_{l=1}^{P} p_l \sum_{u=N-L}^{N-1} \sum_{k=N-L}^{N-1} \sum_{m=N-u}^{L} \sum_{q=N-k}^{L} I(u,k,m,q) \\ & \times h(-mT - \tau_l) h(-qT - \tau_l) \cos[2\pi(u-k)n/N], \end{aligned} \tag{5.49}$$

where

$$I(u,k,m,q) = \begin{cases} 1, & u + m = k + q, \\ 0, & \text{otherwise}. \end{cases} \tag{5.50}$$

Observe that the term $\sigma^2_{\lambda,n}$ can be attenuated or even eliminated by increasing cyclic prefix p. We could also have added a cyclic extension in order to attenuate the term $\sigma^2_{\omega,n}$. In practice, only the cyclic prefix is worth adding because in general $\sigma^2_{\omega,n} << \sigma^2_{\lambda,n}$.

The average SNIR in the n-th carrier is given by

$$\overline{\rho}_n = \frac{b_n^{alt}}{\sigma^2_{\lambda,n} + \sigma^2_{\omega,n} + \sigma^2_z}, \tag{5.51}$$

where σ^2_z is the variance of the Gaussian random noise $z(t)$. The BER of the QDPSK signal (see [22]-p.786) in the n-th carrier can be computed by

$$P^{alt}_{b,n} = \frac{1}{2}\left[1 - \frac{\mu_n}{\sqrt{2 - \mu_n^2}}\right], \tag{5.52}$$

where

$$\mu_n = \frac{\overline{\rho}_n}{1 + \overline{\rho}_n}. \tag{5.53}$$

The term $\overline{\rho}_n$ is the average received SNIR in the n-th carrier, which can be computed by Eq.(5.51).

To confirm the validity of these equations, BER performance based on this theory was compared with the results of computer simulations. The channel model used was the 16-ray Rayleigh fading channel of Figure 5.11. Assuming that the number of carriers is $N = 32$, Figure 5.15 shows the average bit error rate performance over the 32 carriers, which can be computed by

$$P_b = \frac{1}{N} \sum_{n=0}^{N-1} P_{b,n}^{alt}. \tag{5.54}$$

Each carrier was modulated by QDPSK at a symbol rate of (20/32) Msymbol/s, so the total symbol rate was 20 Msymbol/s. The pulse energy to noise density ratio, Eb/No, was set to 30 dB. Simulations were run for five values of the cyclic prefix ($p = 0$, 1, 2, 3 and 4). This means that a guard period of $\frac{p}{p+N} \times T_S$ was wasted per symbol period. For $p = 4$, the wasted guard period corresponds to a power loss of only 0.51 dB. It can be seen that the theoretical results agreed well with the simulation results.

5.6 Conventional versus Alternative OFDM

The bandwidth efficiency of the alternative OFDM depends on the rolloff factor α. A small α is desired because bandwidth efficiency is inversely proportional to α. For example, $\alpha = 0.1$ corresponds to an excess bandwidth of 10%. In this case a symbol rate of 20 Msymbol/s occupies a bandwidth of 22 MHz. This bandwidth efficiency is close to what can be achieved with the conventional OFDM. Figure 5.16 plots the theoretical bit error rate performance P_b for QDPSK of conventional and alternative OFDM in the 16-path Rayleigh channel model of Figure 5.11. Three values of the rolloff factor were considered, $\alpha = 0.1$, 0.5 and 1.0. A cyclic prefix of $\frac{4}{36}T_S$ (or a 0.51 dB loss) was considered for both OFDM schemes. It can be seen that using a small rolloff factor causes degradation in the performance at high values of Eb/No. This is due mainly to the term $\omega_{i,n}$ of Eq. (5.34), which represents the ISI coming from future symbols, a kind of ISI that does not occur in

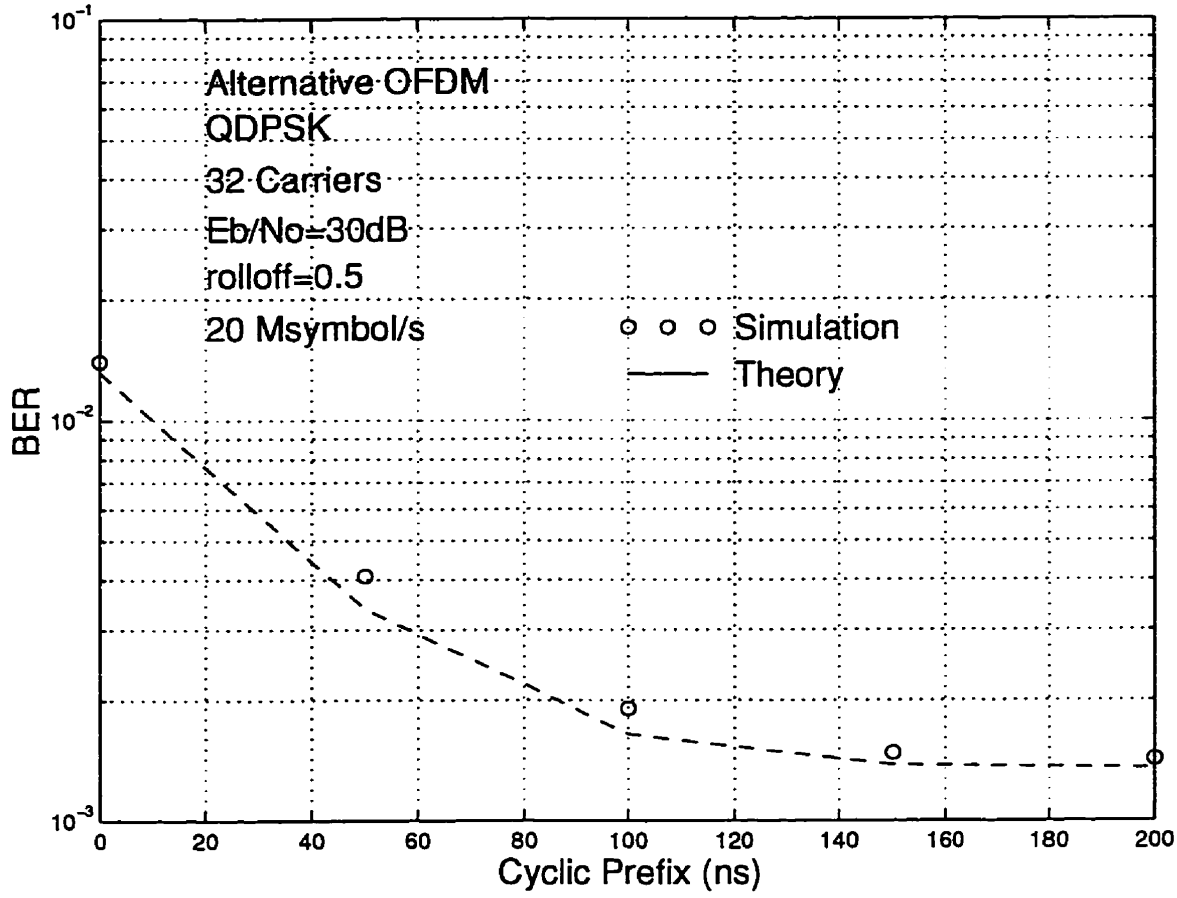

Figure 5.15: Theoretical and simulation results of QDPSK alternative OFDM in a frequency selective channel

the conventional OFDM. However, for Eb/No below 20 dB, the range of practical interest, the performance of the alternative OFDM is close to the performance of the conventional OFDM, even for a rolloff factor as small as 0.1. Therefore the alternative OFDM can match the bandwidth efficiency of the conventional OFDM without sacrificing performance.

5.7 Coding Requirement

In dispersive channels, when the total bandwidth is subject to frequency selective fading, the components of $\{A_{i,n}\}$ transported by carriers that are close to a spectral null are badly

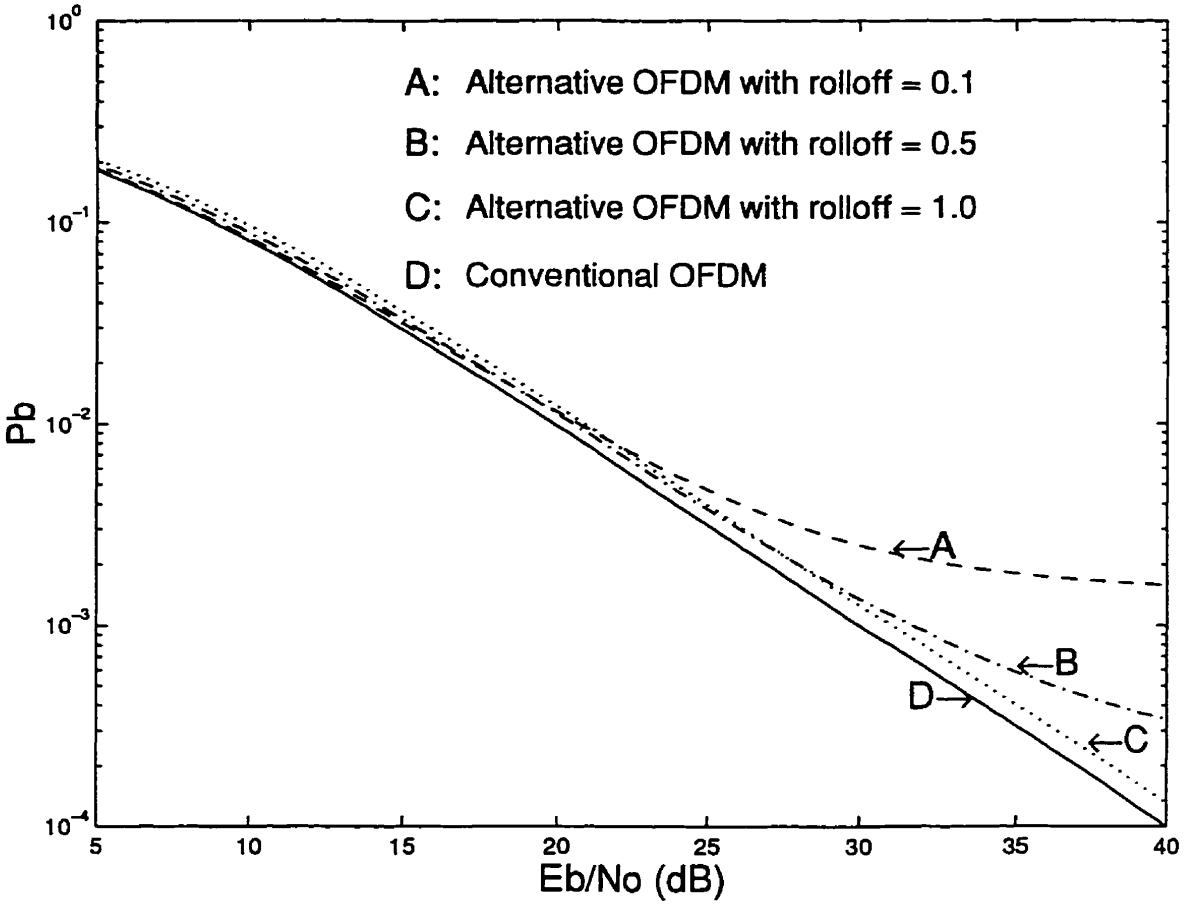

Figure 5.16: BER performance of conventional and alternative OFDM (QDPSK, 32 carriers)

attenuated, while other components may have their power enhanced. This could cause errors to be concentrated in these badly attenuated carriers. This problem can be treated by using codes capable of spreading each information bit among the carriers as much as possible. In this case, recovery of the modulated data may still be possible provided that enough carriers are not badly attenuated. A coding scheme capable of fulfilling this purpose is Trellis Coded Modulation (TCM). Moreover, TCM does not require bandwidth expansion in order to achieve the information redundancy required for coding. Instead TCM expands the constellation.

We used a simple TCM code combined with multi-carrier modulation and interleaving to simulate the FFA in the three locations described in Chapter 2. The simulation is represented by the block diagram of Figure 5.17, which can be used to represent both the conventional OFDM and the alternative OFDM simulations. However, in the alternative OFDM case, the IDFT and DFT blocks are N-point FFTs, therefore there is no need for padding with zeros. Moreover, the Low Pass Filters (LPF) used in the transmitter of the alternative OFDM signal are raised cosine filters.

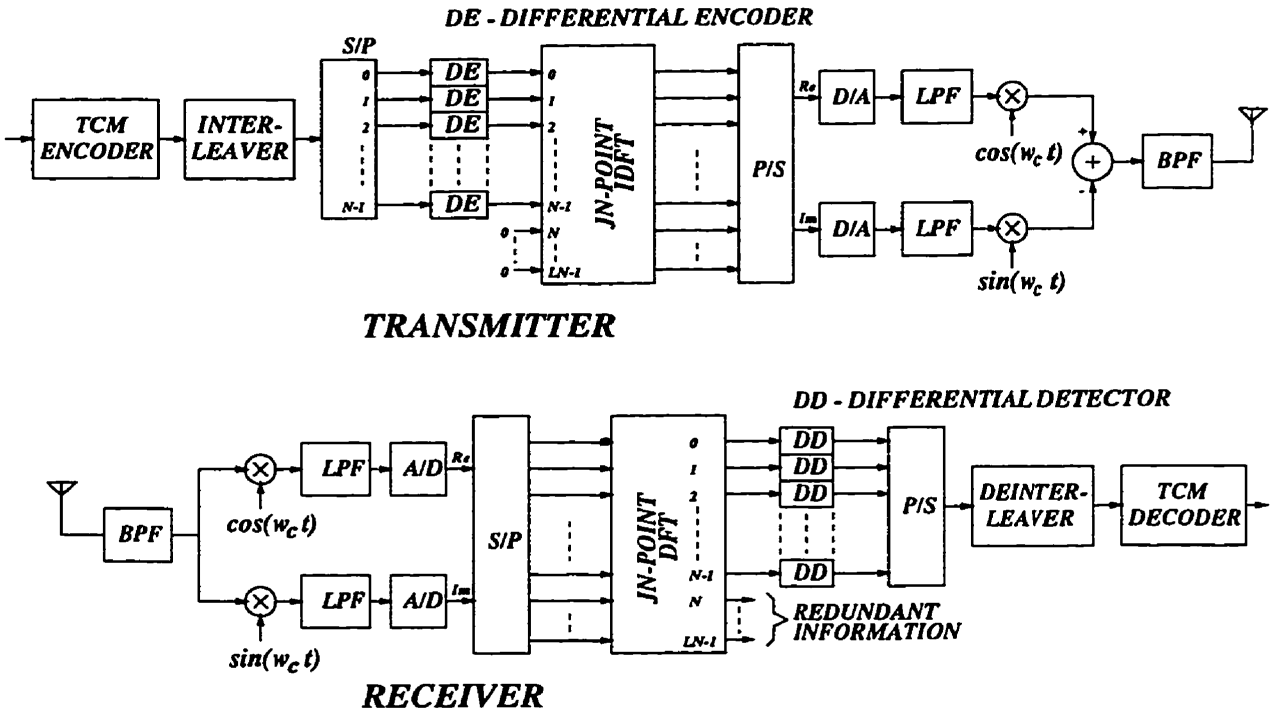

Figure 5.17: Simulation block diagram

The chosen TCM code expands the constellation from the two-point constellation of Figure 5.18-a to the four-point constellation of Figure 5.18-b. Therefore, an uncoded BPSK (Binary Phase Shift Keying) is encoded into a QPSK signal.

In the design of the trellis code for fading channels, the main objective is to achieve as large a *shortest error event path* [22]-p.831 as possible, since this parameter is equivalent to the amount of diversity in the received signal. In order to increase the shortest error

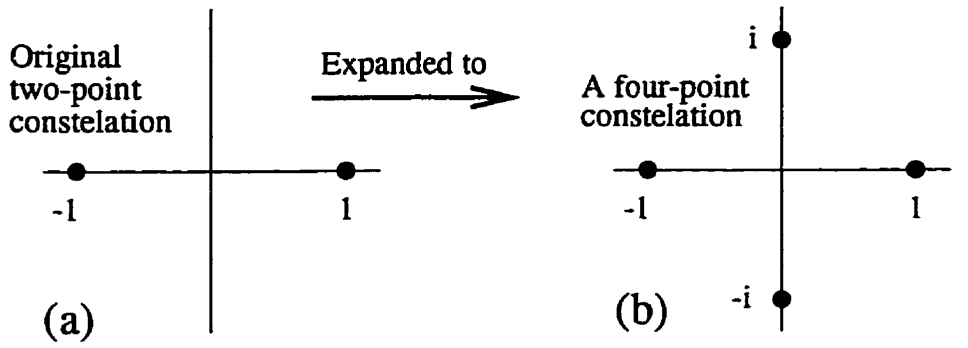

Figure 5.18: Two-point constellation expanded to a four-point constellation

event path, we have to increase the number of states in the trellis that is used to encode the BPSK signal into the QPSK signal. We used the four-state trellis depicted in Figure 5.19 in the simulations. This figure also shows how the two-phase information signal is mapped into the four-phase signal. Figure 5.20 shows the shortest error event path provided by this trellis code. As we can see, the shortest error path spans over a period of three encoded symbols, and since three consecutive symbols are transmitted by different carriers, the TCM code yields diversity over three carriers.

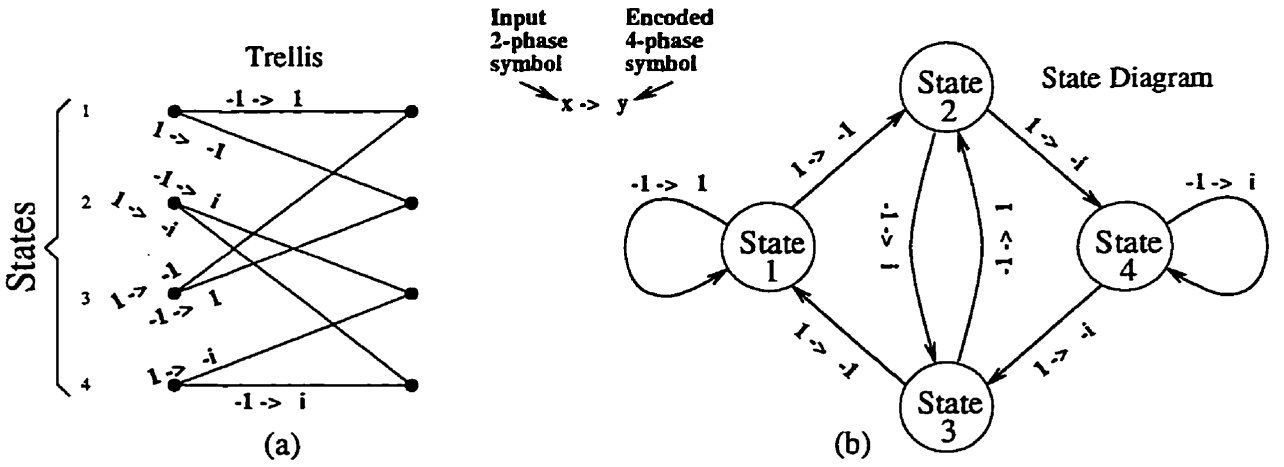

Figure 5.19: Encoding used in the simulations; (a) trellis representation, and (b) state diagram representation

This trellis coding scheme can be made more effective by maintaining frequency separation, which can be accomplished by interleaving or sufficiently separating successive output

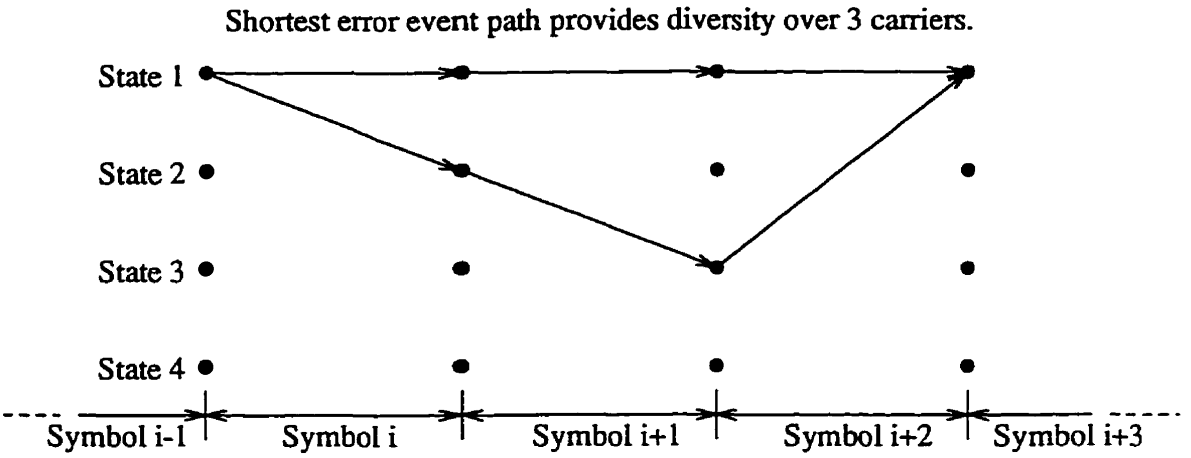

Figure 5.20: Shortest error path provided by the TCM code

symbols from the encoder. To better understand this, we should note that if a given carrier is deeply attenuated for being close to a spectral null, then it is likely that the adjacent carriers will also be attenuated at some extent. Therefore, if interleaving is not used, three consecutive symbols that are transmitted by the three adjacent and attenuated carriers will suffer the fading effect. It is easy to see that the TCM coding, which can provide diversity over three carriers, will not be very effective if the three carriers happen to be attenuated. By interleaving the symbols, we avoid that consecutive symbols are transmitted by adjacent carriers, which makes the TCM coding scheme more effective. In the simulations, the block interleaver in Figure 5.21 was used.

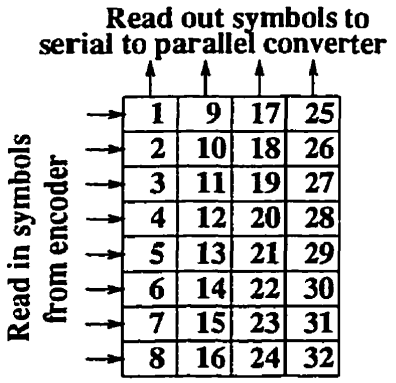

Figure 5.21: The block interleaver used in the simulations

5.8 Representing the Measured Channels in the Simulations

As seen in Eq.(5.6), a static frequency selective channel can be modeled as a tapped delay line, each tap, β_l, being the complex envelope of the signal received on the l-th path. Unfortunately the non-coherent channel measuring experiment described in Chapter 2 could only be used to obtain the amplitude frequency response across a 20 MHz channel. This information is not enough to determine the complex tap values of Eq. (5.6). However, the simulations can be run without knowing the actual tap values because, provided that the ISI is completely eliminated by a cyclic prefix, the exact tapped delay line of a given measured channel can be replaced by any tapped delay line whose amplitude frequency response satisfactorily approximates the actual amplitude frequency response. These alternative tapped delay lines were obtained under the assumption that any measured channels can be represented by the 16-path Rayleigh channel model in Figure 5.11. Then, for each measured channel, a total of 10^4 tapped delay outcomes were drawn, and the outcome which best approximated the measured amplitude frequency response was picked. As an example, Figure 5.22 plots the experimentally measured amplitude frequency response of channel "P1S3" (position 1-sector 3, see definition in Chapter 2) of location 1. It also plots the amplitude frequency response of the tapped delay line chosen to represent this channel in the simulations. It has been observed that, for this channel and for all the other measured channels, the amplitude frequency response of the chosen tapped delay line approached the respective experimentally measured amplitude frequency response reasonably well.

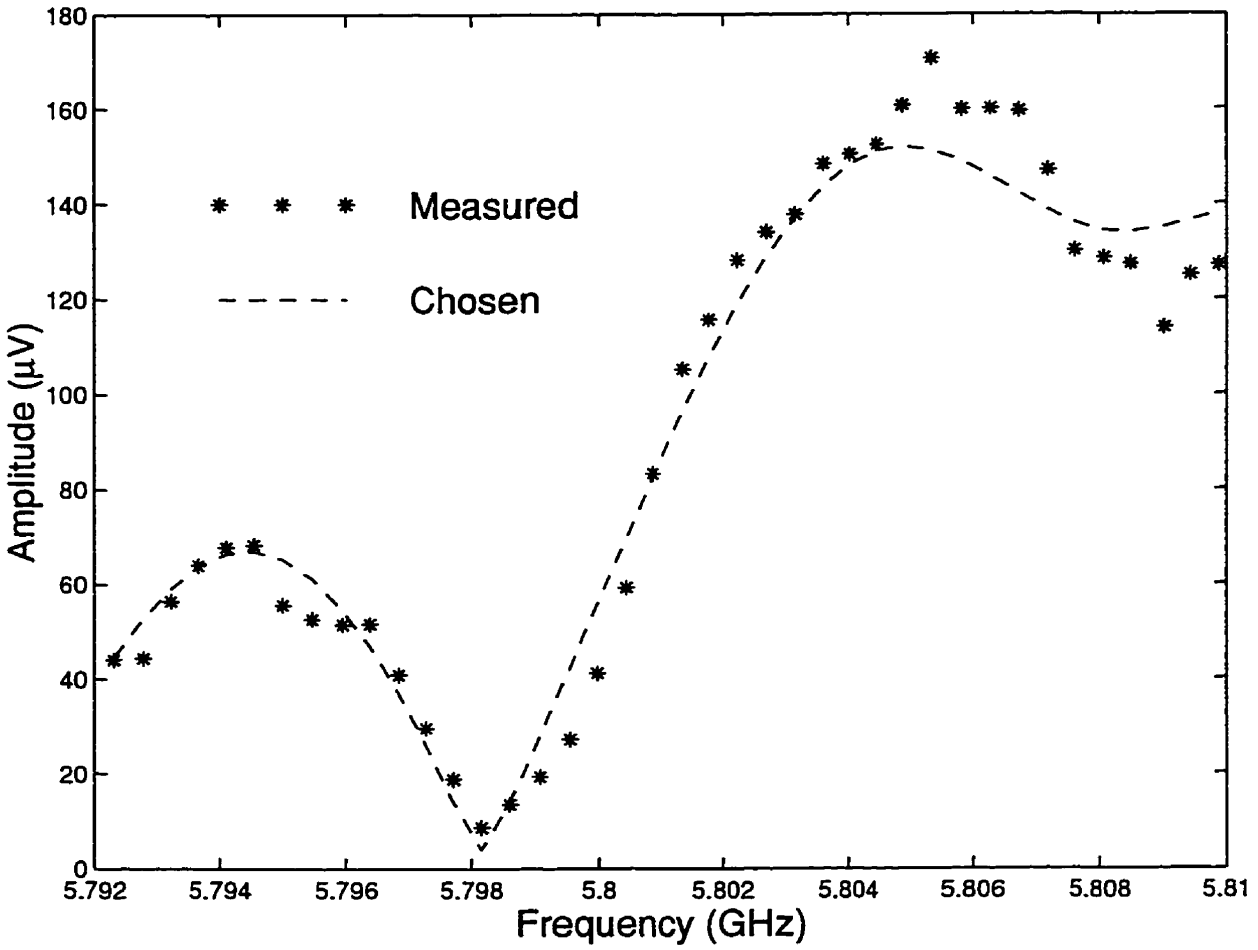

Figure 5.22: Measured and chosen amplitude frequency responses of channel "P1S3" in location 1

5.9 Simulation Description

The FFA maximum throughput algorithm described in Chapter 3 assumes that a single value of the capture threshold is used by all portables in the microcell. The simulation process described here uses a modified version of this algorithm where each portable works with its particular capture threshold value. This makes more sense because portables transmit through channels with different characteristics, which causes different portables to be able to stand different amounts of interference. Therefore, in order to maximize throughput, each portable should operate with its minimum supportable capture threshold value.

The simulation process starts with all the portables operating at a low capture threshold value and communicating with the base station sector that provides highest average power. The simulation runs until each portable has transmitted at least 100 packets. At this time, the number of packets that arrived in the base station corrupted by error are counted for each portable, and any portable that transmitted more than five corrupted packets has its capture threshold increased by 1 dB, and this ends the first iteration. In the second iteration, the simulation restarts with the portables operating at their new capture threshold. Again, the simulation runs until each portable has transmitted at least another 100 packets. At this time, the number of packets that arrived corrupted by error are counted again for each portable, and any portable that transmitted more than five corrupted packets has its capture threshold increased by 1 dB. This process is repeated for a number of iterations until each portable transmits less than five corrupted packets. If a given portable could not transmit less than five corrupted packets per set of 100 packets after having increased its capture threshold to 20 dB, the base station switches the communication with this portable to the antenna sector that provides the second highest average power. This is done because sometimes the best sector for communicating with a given portable is not the one that provides highest average power; it also matters how the power is distributed among the carriers. The simulation ends when all the portables transmit less than 5 corrupted packets per set of 100 transmitted packets. The throughput achieved in the last iteration is taken

as the output of the simulation.

Note that five corrupted packets per set of 100 transmitted packets represents a reasonable packet error rate if the system operates with an Automatic Repeat reQuest (ARQ) protocol. We observed that only a few portables were subjected to a packet error rate of $\frac{5}{100}$, and most of the portables transmitted no corrupted packets during the last iteration of the simulation. Therefore, the average packet error rate was much smaller than $\frac{5}{100}$.

In order to understand better the computations that were performed during the simulations, let us suppose that in a given time slot, two portables, $\mathbf{P}_1$ and $\mathbf{P}_2$, are allowed to transmit. Figure 5.23 illustrates this scenario.

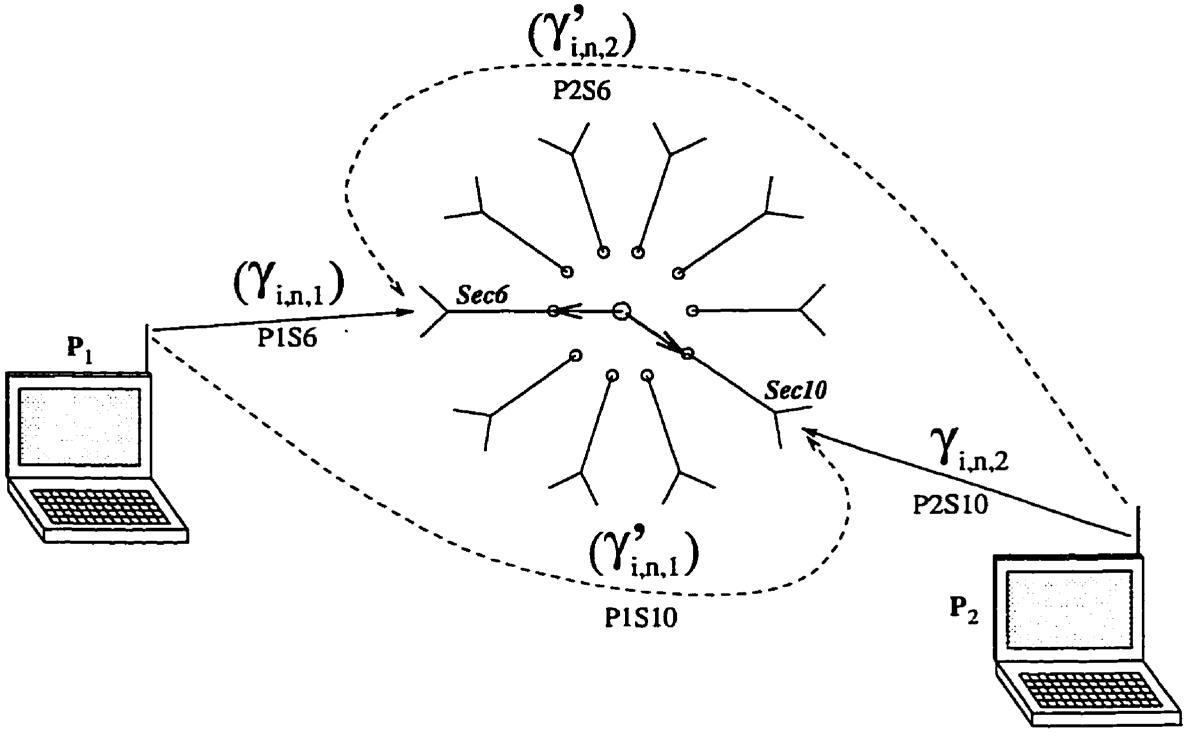

Figure 5.23: An illustration of simultaneous transmissions

During the i-th symbol period, the base station receives symbols $\gamma_{i,n,1}$ and $\gamma'_{i,n,2}$ through channels "P1S6" and "P2S6", respectively. Symbol $\gamma_{i,n,1}$ carries the desired information transmitted by portable $\mathbf{P}_1$ in the n-th carrier during the i-th symbol period. Symbol $\gamma'_{i,n,2}$ represents the interference from $\mathbf{P}_2$ received by the base station in the same carrier, during

the same symbol period. Therefore the symbol received during the i-th symbol period in the n-th carrier from portable $\mathbf{P}_1$ can be expressed as

$$R_{i,n,1} = \gamma_{i,n,1} + \gamma'_{i,n,2} + z_{i,n}, \tag{5.55}$$

where $z_{i,n}$ is the Gaussian noise term. In the simulations, this term was such that the Eb/No averaged over the N carriers was made equal to 20 dB. The term $\gamma_{i,n,1}$ can be calculated as

$$\gamma_{i,n,1} = D_{i,n,1} C_n, \tag{5.56}$$

where C_n represents the channel response for the n-th carrier. It is expressed by Eq. (5.12) in the case of conventional OFDM, and by Eq. (5.40) in the case of alternative OFDM. The term $D_{i,n,1}$ represents the differentially encoded information transmitted by portable $\mathbf{P}_1$ during the i-th symbol period in the n-th carrier:

$$D_{i,n,1} = D_{i-1,n,1} A_{i,n,1}, \tag{5.57}$$

where $A_{i,n,1}$ represents the information symbol, encoded by the TCM scheme and interleaved, that must be recovered during the i-th symbol period in the n-th carrier.

In the simulations, demodulation assumed differential phase estimation. In this case the demodulated symbol can be expressed as

$$\begin{aligned} K_{i,n,1} &= R_{i,n,1} R^*_{i-1,n,1} \\ &= (\gamma_{i,n,1} + \gamma'_{i,n,2} + z_{i,n})(\gamma_{i-1,n,1} + \gamma'_{i-1,n,2} + z_{i-1,n})^* \\ &= (\gamma_{i,n,1}\gamma^*_{i-1,n,1}) + (\text{interference/noise terms}) \\ &= (D_{i,n,1} C_n)(D_{i-1,n,1} C_n)^* + (\text{interference/noise terms}) \\ &= A_{i,n,1}|C_n|^2 + (\text{interference/noise terms}), \end{aligned} \tag{5.58}$$

where $|C_n|$ represents the gain of the n-th carrier in channel "P1S6" (see Figure 5.23). The $K_{i,n,1}$ sequence is then deinterleaved and decode by the TCM decoder. In the case of alternative OFDM, the ISI term $\lambda_{i,n}$ was disregarded based on the assumption that an adequate cyclic prefix can be used. The other ISI term, $\omega_{i,n}$, was also disregarded since in the simulations $\omega_{i,n} << z_{i,n}$. In the case of the conventional OFDM, the second and third

terms of Eq.(5.9) were disregarded based on the assumption that an adequate cyclic prefix can be used.

The other features of the simulations are the following:

- The number of carriers used was $N = 32$.
- A rolloff factor of 0.1 was assumed in the case of alternative OFDM.
- A packet size of only 64 bits was used in order accelerate the simulations, so the number of symbols (bits) per packet transmitted on each carrier were two; one was used to provide phase reference for the differential detector, and the other was encoded by the trellis code.
- The Viterbi algorithm was used in the decoder.
- Only up-link traffic was simulated.
- Power control was used. The power control mechanism assumes that all the portables adjust their transmitting power so that the base station receives, through the best sector for communication with a given portable, the same average power level from any portable transmissions.
- Simulations were run with the modified FFA maximum throughput algorithm operating with different numbers of ports, from two ports up to a number of ports where the maximum throughput saturated.

5.10 Simulation Results

The simulation results for locations 1, 2 and 3 are shown in Figures 5.24, 5.25 and 5.26, respectively. In location 1, the maximum throughput saturated with three ports, meaning that it is pointless to use more than three ports in this location with multi-carrier modulation, the TCM coding scheme, and a sectorization level of 10. The maximum throughput in

location 1 was 2.8 packets per time slot when using the alternative OFDM, and 2.5 packets per time slot when using the conventional OFDM. In location 2, the maximum throughput saturated with five ports at 3.9 packets per time slot when using the alternative OFDM, and at 4.2 packets per time slot when using the conventional OFDM. In location 3, the maximum throughput saturated with five ports at 4.3 packets per time slot when using the alternative OFDM, and at 4.2 packets per time slot when using the conventional OFDM.

The main conclusion is that the alternative OFDM scheme provides performance similar to the performance achieved with the conventional scheme.

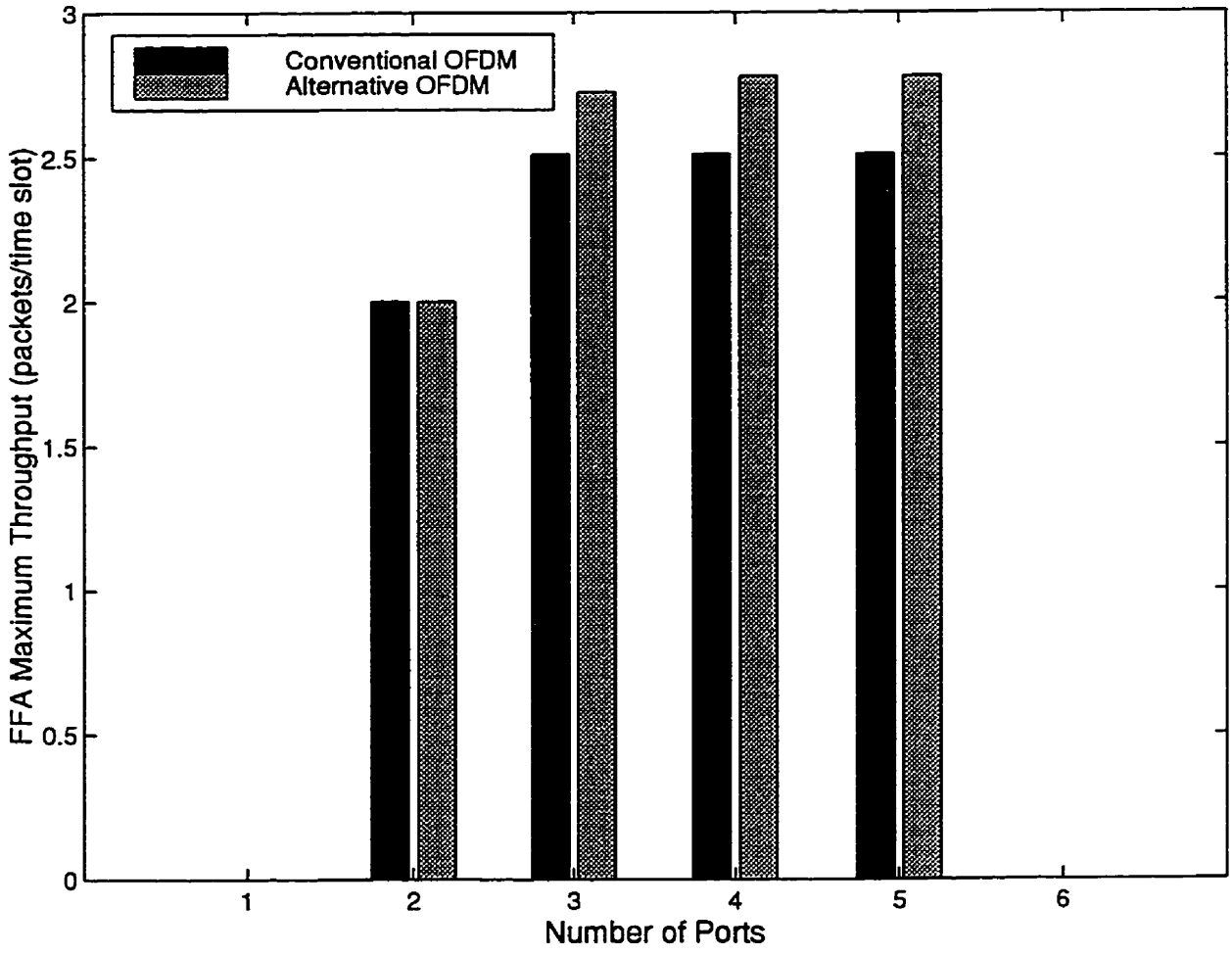

Figure 5.24: Simulated FFA maximum throughput in location 1 with conventional and alternative OFDM

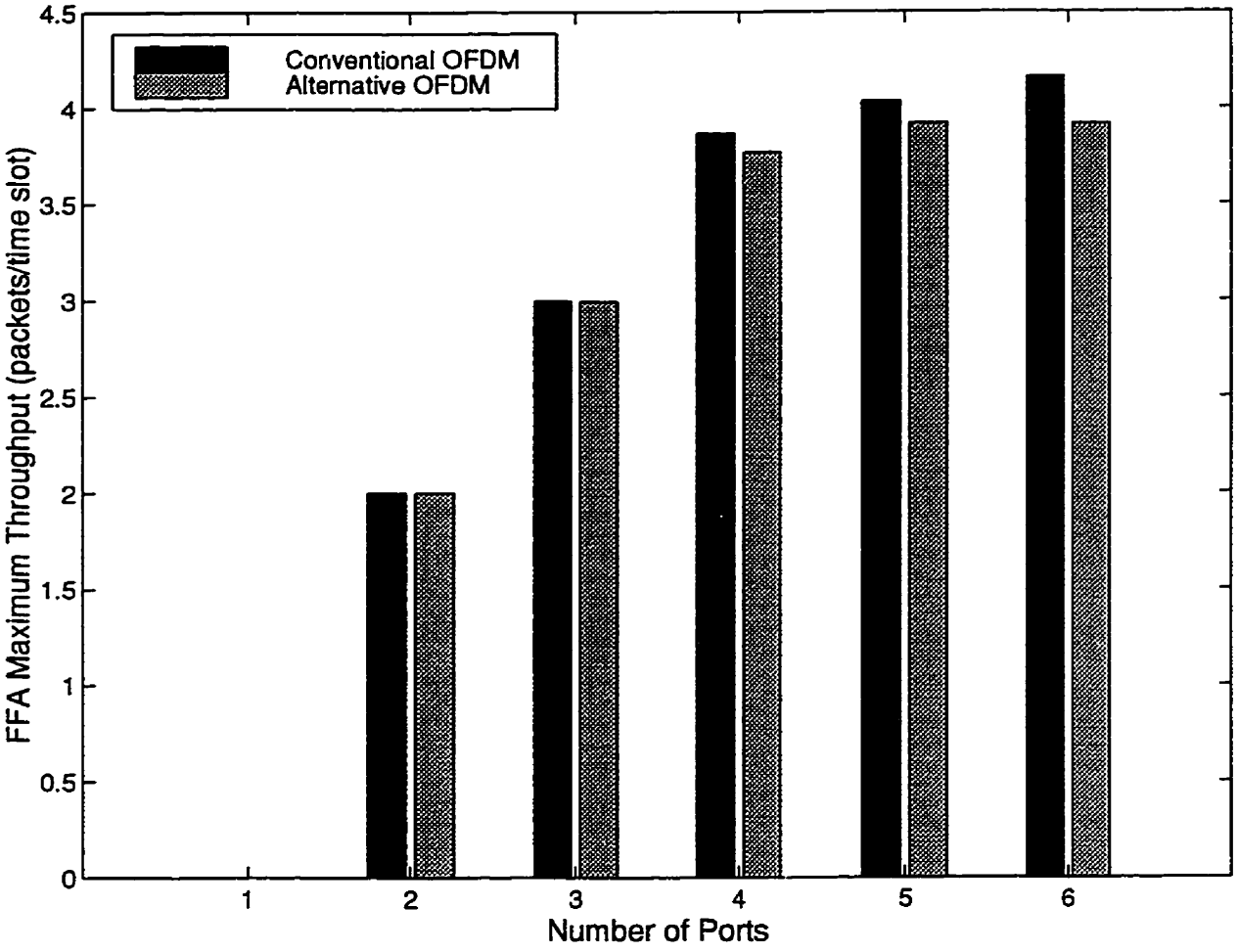

Figure 5.25: Simulated FFA maximum throughput in location 2 with conventional and alternative OFDM

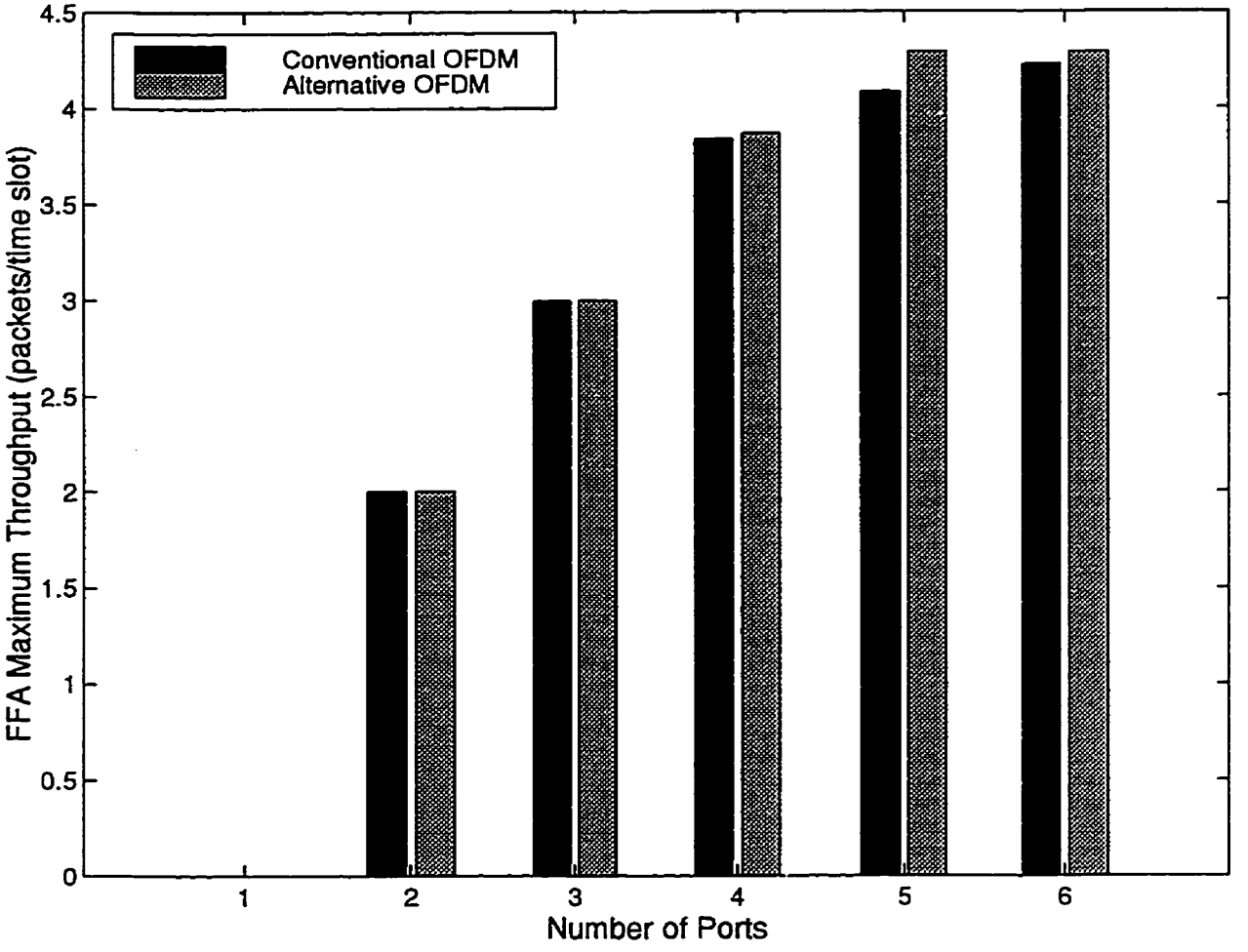

Figure 5.26: Simulated FFA maximum throughput in location 3 with conventional and alternative OFDM

Chapter 6

Conclusions and Suggestions for Future Research

6.1 Conclusions

This thesis proposed and investigated a new indoor communication system in which a base station uses sectored antennas, and portable terminals use omni-directional antennas. The system is able to handle simultaneous packet transmissions in a microcell. It was shown that the system can provide significant capacity gain when compared with indoor sectored antenna systems that can transmit only one packet at a time.

Chapter 2 introduced the compatibility concept and described a experiment devised to verify compatibility among portables. Measurements were taken in three indoor location: a closed indoor environment represented by a section of a building floor; a semi-open environment represented by a large room divided into cubicle offices; and an open environment represented by a classroom. Measurement results were presented in terms of average compatibility among portables in these locations.

Chapter 3 proposed a multiple access scheme that is able to take advantage of the compatibilities among portables in order to transmit more than one data packet per time slot. The FFA algorithm was proposed to schedule simultaneous packet transmissions in

the microcell. The algorithm maximum throughput was investigated for the three indoor locations.

Chapter 4 used a statistical model of indoor multipath propagation to investigate the use of different sectorization levels in the proposed system. The simulation parameters of this model were adjusted to fit the experimental results. The simulations showed that there is considerable potential for increasing the maximum throughput by increasing the number of sectors in the microcell.

Chapter 5 proposed a new multi-carrier modulation scheme. The scheme was analysed for the case of frequency selective fading channels and showed to be able to achieve performance comparable to the performance of the conventional multi-carrier modulation scheme that requires more processing power. The FFA maximum throughput was then evaluated with the system operating with the proposed modulation technique and with the conventional multi-carrier scheme. The maximum throughput achieved with ten antenna sectors was around 2.8 packets per time slot in the closed indoor location, and around 4.2 packets per time slot in the other two locations.

6.2 Suggestions for Future Research

We suggest the following areas for further research on the topic:

- Investigate the use of antenna arrays to replace the sectored antennas.
- Study maximum throughput and portable blocking issues when the microcell operates with specific traffic compositions, for example, Ethernet traffic.
- Investigate how channel dynamics affect the amount of overhead required for allowing the base station to track the compatibility relations in the microcell, and investigate loss in maximum throughput if the tracking is not perfect.
- Study the effect of intercell interference.

- Apply the proposed multiplexing scheme to outdoor fixed wireless system. For example, Local Multi Point Distribution Systems (LMDS) and Wireless Local Loop Systems (WLL).

Appendix A

NP-Completeness of the N-Port Frame Scheduling Problem

In this appendix we prove that the N-PORT FRAME SCHEDULING problem ($N \geq 3$) is in the **NP**-complete class of problems. "The theory of **NP**-completeness provides many straightforward techniques for proving that a given problem is "just as hard" as a large number of other problems that are widely recognized as being difficult and that have been confounding the experts for years" [10].

According to [10], there are four steps in proving that problem Π is in the **NP**-complete class of problems:

1. showing that problem Π is in the **NP** (not the same as **NP**-complete) class of problems (the **NP** class is described below),
2. selecting a known **NP**-complete problem Π',
3. constructing a transformation f from Π' to Π, and
4. proving that the transformation f can be performed in polynomial time.

The **NP** class is a more generic class of problems that contains the **NP**-complete class: **NP**$\supseteq$**NP**-complete.

Informally, an **NP** problem can be solved by a nondeterministic algorithm comprising two stages: a guessing stage that guesses a solution; and a deterministic stage that checks the validity of the guessed solution in polynomial time. Let us consider, for example, the classical TRAVELING SALESMAN problem defined in [10] the following way:

INSTANCE: A finite set $C = \{c_1, c_2, ..., c_m\}$ of "cities," a "distance" $d(c_i, c_j) \in Z^+$ for each pair of cities $c_i, c_j \in C$, and a bound $B \in Z^+$ (where Z^+ denotes the positive integers).

QUESTION: Is there a "tour" of all the cities in C having total length no more than B, that is, an ordering $< c_{\pi(1)}, c_{\pi(2)}, ..., c_{\pi(m)} >$ of C such that

$$[\sum_{i=1}^{m-1} d(c_{\pi(i)}, c_{\pi(i+1)})] + d(c_{\pi(m)}, c_{\pi(1)}) \leq B \ ? \qquad \blacksquare$$

This problem is in **NP** since we can propose using the nondeterministic algorithm of Figure A.1 to solve it, and in which we can identify the two required stages.

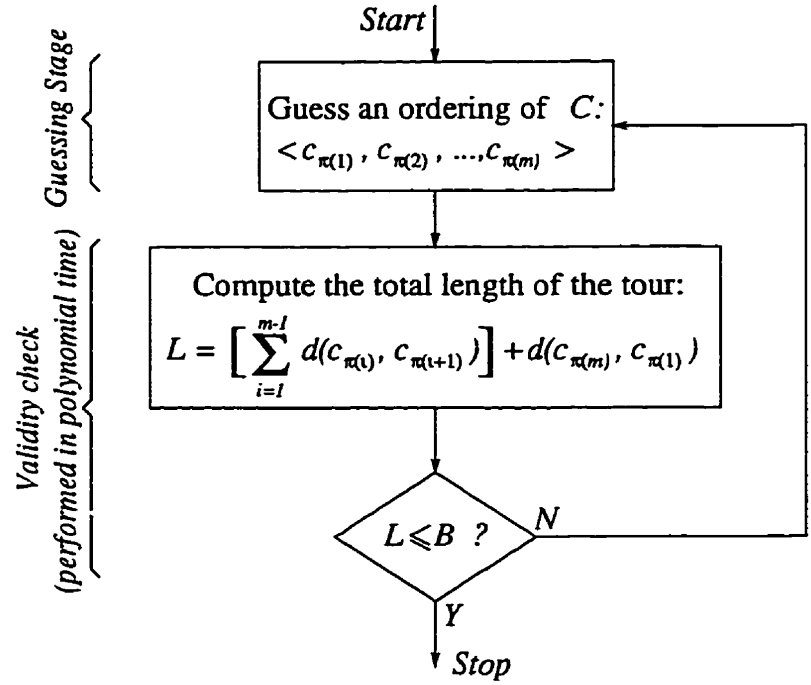

Figure A.1: A nondeterministic algorithm for solving the TRAVELING SALESMAN problem

Decision Problems Versus Optimization Problems

The 3-PORT FRAME SCHEDULING problem is an example of an optimization problem; it consists of finding the maximum number of triples of compatible packets that can be transmitted in the time slots of a given time frame. However, the theory of **NP**-completeness is designed to be applied to decision problems only. The TRAVELING SALESMAN problem is an example of a decision problem.

In general, an optimization problem can be associated to a decision problem. For example, the 3-PORT FRAME SCHEDULING decision problem is:

INSTANCE: A finite set $P = \{p_1, p_2, ..., p_m\}$ of data packets (this set can also be seen as the set of portables to whom the packets belong); the compatibility relations of three packet combinations given by a 3-dimensional array C_3 of ones ("1s") and zeros ("0s"):

$$C_3(i,j,k) = \begin{cases} 1, & \text{if packets } i,\ j \text{ and } k \text{ satisfy compatibility condition.} \\ 0, & \text{otherwise.} \end{cases}$$

QUESTION: Can at least L triples of compatible packets be allocated in a time frame? (see Figure A.2) ■

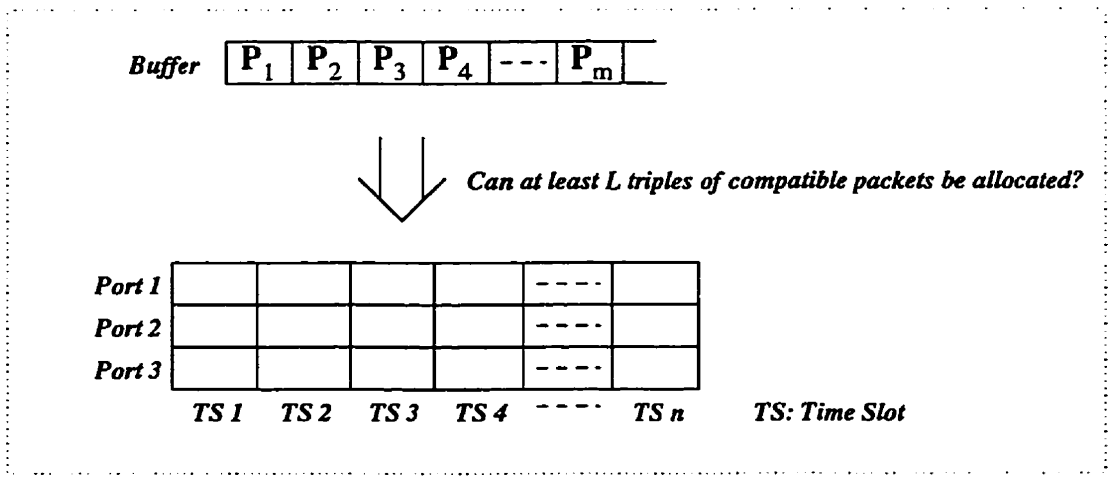

Figure A.2: The 3-port frame scheduling decision problem

The key point to observe is that this decision problem can be no harder than the corresponding optimization problem. Clearly, if we could find the maximum number of

triples of compatible packets by solving the optimization problem, then we could also solve the decision problem just by comparing L with the solution given by the optimization problem.

The 3-DIMENSIONAL MATCHING Problem

In order to prove that the 3-PORT FRAME SCHEDULING (**3PFS**) decision problem is **NP**-complete, we will transform the 3-DIMENSIONAL MATCHING (**3DM**) problem, which is a known **NP**-complete problem, to the **3PFS**. The **3DM** problem is the 3-dimensional version of the classical "marriage problem": given "n" unmarried men and "n" unmarried women, along with a list of all male-female pairs who would be willing to marry one another, is it possible to arrange at least "m" marriages so that polygamy is avoided and "m" men and "m" women receive an acceptable spouse? Let us imagine now a species that is composed of three sexes, X, Y and W. In this case, the 3-dimensional matching problem consists in finding 3-*way marriages* that would be acceptable to all three participants. For the relief of traditionalists, whereas **3DM** is **NP**-complete, the ordinary marriage problem can be solved in polynomial time [30]. For this reason, we will not be able to extend our **NP**-completeness proof of the frame scheduling problem to the 2-port case.

NP-Completeness Proof

Theorem: **3PFS** is **NP**-complete.

Proof:

1. It is easy to see that **3PFS** $\in$ **NP**, since a nondeterministic algorithm needs only guess L triples of packets and use C_3 to check in polynomial time if the packets in each triple are compatible.

2. We select the **3DM** problem, which is a known **NP**-complete problem.

3. We transform **3DM** to **3PFS**. This can be easily done just by assuming that the elements of X, Y and W are data packets of a set P, and by creating a compatibility array C_3 using the compatibility relations among the elements of X, Y and W, and considering the fact that elements inside one set, X, Y or W, are not compatible among themselves.

4. Clearly, the transformation done in step 3 can be performed in polynomial time. ■

N-PORT FRAME SCHEDULING Problem

Intuitively, the N-PORT FRAME SCHEDULING (N>3) is "harder" than the the 3-PORT FRAME SCHEDULING, so it must be also a **NP**-complete problem. A rigorous proof that the N-PORT FRAME SCHEDULING (**NPFS**) problem is indeed in the class of **NP**-complete problems can be obtained by transforming the **3PFS**, which now is a know **NP**-complete problem, to the generic N-PORT FRAME SCHEDULING (N>3) problem. For that, we just have to add to the set of packets a number of imaginary packets that are compatible to any triple of compatible packets. This guarantees that, if we can find L triples of compatible packets, we can also find L subsets of N compatible packets. In other words, the **3PFS** problem can be seen as a relaxed version of the **NPFS** problem (relaxed by the addition of the imaginary packets). Therefore, if we had a method to solve the **NPFS** (N>3) in polynomial time, we would also be able to solve the **3PFS** problem in polynomial time just by adding the imaginary packets. However, we know that the **3PFS** problem is a **NP**-complete problem, so the relaxed version of the **NPFS** problem is also a **NP**-complete problem. This proves that the **NPFS** problem is a **NP**-complete problem, i.e, if an "easier" relaxed version of this problem is in the class of **NP**-complete problems, then the true **NPFS** problem is at least as "hard".

Bibliography

[1] A. S. Macedo and E. S. Sousa,"Coded OFDM for Broadband Indoor Wireless Systems," *ICC'97*, Vol. 2, pp. 934-938, Montreal, June 1997.

[2] A. S. Macedo and E. S. Sousa,"Broadband Indoor Wireless Systems with In-Cell Frequency Reuse Based on Sectored Antennas," *SBT'97*, pp. 349-352, Recife-Brazil, August 1997.

[3] A. S. Macedo and E. S. Sousa, "In-Cell Frequency Reuse for Broadband Indoor Wireless Systems Using Sectored Antennas," To appear in *Wireless Personal Communications*, Special Issue on Wireless Broadband Communications.

[4] A. S. Macedo and E. S. Sousa,"Antenna Sector-Time Division Multiple Access for Broadband Indoor Wireless Systems," To appear in *IEEE JSAC*.

[5] D. Buchholz, P. Odlyzko, M. Taylor and R. White, "Wireless In-Building Network Architecture and Protocols," *IEEE Network Magazine*, Vol. 5, No. 6, pp. 31-38, Nov. 1991.

[6] A. S. Mahmoud, D. D. Falconer and S. A. Mahmoud, "A Multiple Access Scheme For Wireless Access to a Broadband ATM LAN Based on Polling and Sectored Antennas," *PIMRC'95*, Vol. 3, pp. 1047-1051, Toronto Canada, Sept. 1995.

[7] J. E. Mitzlaff, "Radio Propagation and Anti-Multipath Techniques in the WIN Environment," *IEEE Network Magazine*, Vol. 5, No. 6, pp. 21-26, Nov. 1991.

[8] K. M. Duch, "Baseband Signal Processing," *IEEE Network Magazine*, Vol. 5, No. 6, pp. 39-43, Nov. 1991.

[9] FCC 96-193 Document, Released on May 7, 1996.

[10] M. R. Garey and D. S. Johnson, *Computers and Intractability - A Guide to the Theory of NP-Completeness,* San Francisco: W. H. Freeman, 1979.

[11] M. de Prycker, *Asynchronous Transfer Mode: Solution for Broadband ISDN,* New York: Ellis Horwood, 1991.

[12] N. Movahhedinia, G. Stamatelos and H. M. Hafez, "Polling-Based Multiple Access for Indoor Broadband Wireless Systems," *PIMRC'95*, Vol. 3, pp. 1052-1056, Toronto Canada, Sept. 1995.

[13] Q. Spencer, M. Rice, B. Jeffs and M. Jensen, "A Statistical Model for Angle of Arrival in Indoor Multipath Propagation," *VTC'97*, Vol. 3, pp. 1415-1419, Phoenix, Arizona, USA, May 1997.

[14] Q. Spencer, M. Rice, B. Jeffs and M. Jensen, "Indoor Wideband Time/Angle of Arrival Multipath Propagation Results," *VTC'97*, Vol. 3, pp. 1410-1414, Phoenix, Arizona, USA, May 1997.

[15] A. A. M. Saleh and R. A. Valenzuela, "A Statistical Model for Indoor Multipath Propagation," *IEEE Journal on Selected Areas in Communications*, Vol. SAC-5, No. 2, pp. 128-137, February 1987.

[16] G. J. M. Janssen, "Wideband Indoor Channel Measurements and BER Analysis of Frequency Selective Multipath Channels at 2.4, 4.75, and 11.5 GHz," *IEEE Trans. Commun.*, Vol. 44, No. 10, pp. 1272-1287, October, 1996.

[17] D. Bertsekas and R. Gallager, *Data Networks, 2nd ed.*, Englewood Cliffs, N.J.: Prentice-Hall, 1992.

[18] S. B. Weinstein and P. M. Ebert "Data Transmission by Frequency-Division Multiplexing Using Discrete Fourier Transform," *IEEE Trans. Communic. Tech.*, Vol. COM-19, No. 5, pp. 628-634, Oct 1971.

[19] J. A. C. Binghan, "Multicarrier Modulation for Data Transmission: An Idea Whose Time Has Come," *IEEE Comm. Mag.*, Vol. 28, No. 5, pp. 5-14, May 1990.

[20] E. A. Lee and D. G. Messerschmitt, *Digital Communications, 2nd ed.,* Kluwer, 1993.

[21] M. Okada, S. Hara and N. Morinaga, "Bit Error Rate Performances of Orthogonal Multicarrier Modulation Radio Transmission Systems," *IEICE Trans, Commun.*, Vol. E76-B, No. 2, Feb. 1993.

[22] J. G. Proakis, *Digital Communications, 3rd ed.,* New York: McGraw-Hill, 1995.

[23] A. J. Viterbi, *CDMA: Principles of Spread Spectrum Communications,* Addison-Wesley, 1995.

[24] G. Yang, K. Pahlavan and T. Holt, "Sector Antenna and DFE Modems for High Speed Indoor Radio Communications," *IEEE Transactions on Vehicular Technology*, Vol. 43, No. 4, pp. 925-933, Nov. 1994.

[25] J. McKown and R. Lee Hamilton, Jr,, "Ray Tracing as a Design Tool for Radio Networks," *IEEE Network Magazine*, Vol. 5, No. 6, pp. 27-30, Nov. 1991.

[26] S. E. Alexander, "Radio Propagation within Buildings at 900 MHz," *Electron Lett.*, Vol. 18, No. 21, pp. 913-914, Oct. 1982.

[27] S. E. Alexander, "Characterizing Buildings for Propagation at 900 MHz," *Electron Lett.*, Vol. 19, No. 20, pp. 860, Sept. 1983.

[28] K. M. Cheung, H. Leib, and S. Pasupathy, "Multipath Induced Intersymbol Interference Bandwidth Expanding Signaling," in *Proceedings of 16th Biennial Symposium on Communications*, pp. 273-276, May. 1992.

[29] J. D. Kraus, *Antennas, 2nd ed.*, New York: Mc Graw-Hill, 1988.

[30] J. E. Hopcroft and R. M. Karp, "An $n^{5/2}$ algorithm for maximum matchings in bipartite graphs", *SIAM J. Comput.* 2, 225-231.

[31] K. Pahlavan and A. H. Levesque, *Wireless Information Networks*, New York: Wiley, 1995.

[32] S. Lin and D. J. Costello , *Error Control Coding,* Englewood Cliffs, N.J.: Prentice-Hall, 1983.

[33] B. Glance and L. J. Greenstein, "Frequency-Selective Fading Effects in Digital Mobile Radio with Diversity Combining," *IEEE Trans. Commun.*, Vol. COM-31, No. 9, pp. 1085-1094, Sept. 1983.

[34] S. Haykin , *Communication Systems, 3rd ed.,* New York: Wiley, 1994.

IMAGE EVALUATION TEST TARGET (QA-3)

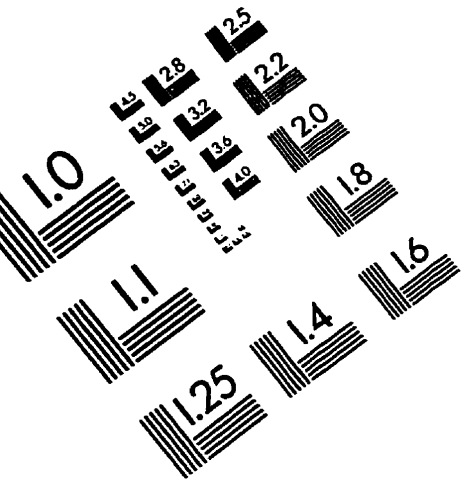

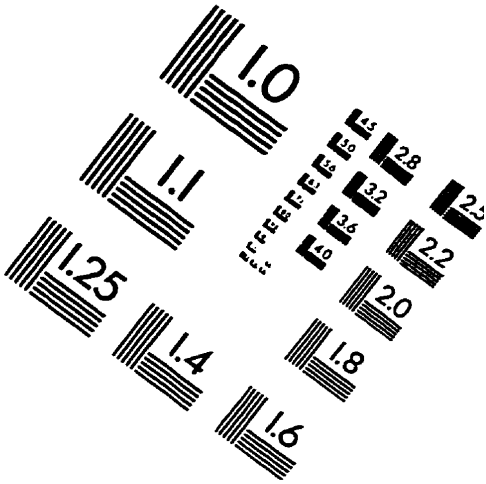

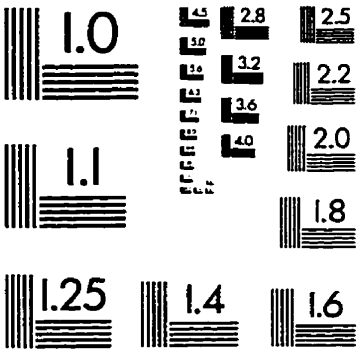

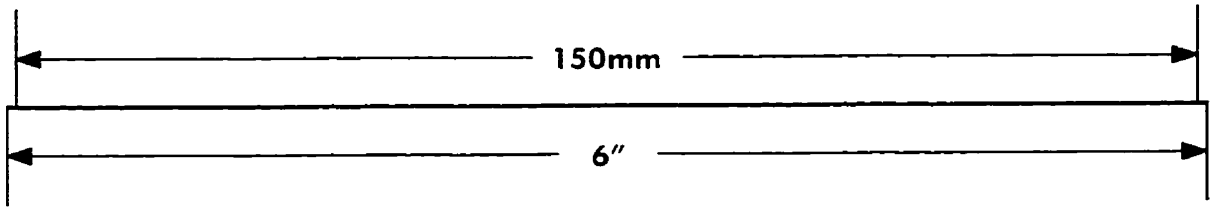

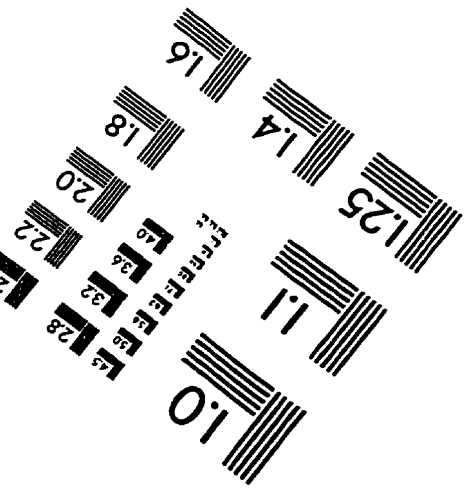

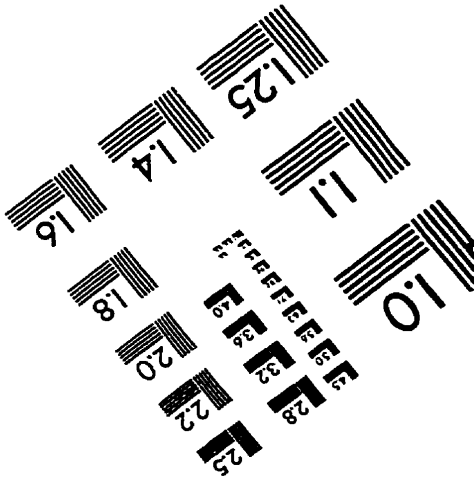

APPLIED IMAGE, Inc
1653 East Main Street
Rochester, NY 14609 USA
Phone: 716/482-0300
Fax: 716/288-5989